# In-situ monitoring and intermittent controller for adaptive trajectory generation during laser directed energy deposition via powder feeding

by

Farzaneh Kaji

A thesis
presented to the University of Waterloo
in fulfillment of the
thesis requirement for the degree of
Doctor of Philosophy
in
Mechanical and Mechatronics Engineering

Waterloo, Ontario, Canada, 2023

## Examining Committee Membership

The following served on the Examining Committee for this thesis. The decision of the Examining Committee is by majority vote.

| | |
|---|---|
| External Examiner NAME: | Christ Prakash Paul |
| | Title: Professor |
| Supervisor(s) NAME: | Ehsan Toyserkani |
| | Title: Professor |
| Internal Member NAME: | Adrian Gerlich |
| | Title: Associate Professor |
| Internal Member NAME: | Amir Khajepour |
| | Title: Professor |
| Internal-external Member NAME: | Shoja'eddin Chenouri |
| | Title: Professor |

## Author's Declaration

This thesis consists of material all of which I authored or co-authored: see the Statement of Contributions included in the thesis. This is a true copy of the thesis, including any required final revisions, as accepted by my examiners.

I understand that my thesis may be made electronically available to the public.

## Statement of Contributions

I would like to acknowledge the names of my co-authors who contributed to the research described in this dissertation, these include:

Prof. Ehsan Toyserkani: Supervision the research, developing original ideas for the current thesis, editing papers, provided lab facilities, review and editing papers.

Dr. Jinoop Arackal Narayanan: Support in material characterization, brainstorming, review and editing papers.

Alikasim Budhwani: Brainstorming on developing a deep learning defect detection network for point clouds.

Mark Zimny: Managing and supporting the research project, providing valuable discussion, research funding.

Patrick Hallen: Brainstorming on software development for bend-pipe application.

German Frikel: Discussion and brainstorming on slicing techniques for printing complex geometries.

Howard Nguyen:  Brainstorming on developing a ray tracing algorithm.

Ali Zardoshtian: Support in material characterization.

Kyle Tam: Design of experiment for determination of critical overhang angles in LDED-PF.

## Abstract

Laser Directed Energy Deposition (LDED) is one of the advanced manufacturing technologies for building near-net-shaped engineering components in a layer-by-layer fashion using high-power lasers as an energy source. LDED using powder feeding (LDED-PF) is widely used due to its higher dimensional accuracy and ability to build fine features. The quality and performance of LDED-PF-built components are dependent on several factors such as process parameters, process conditions, feedstock properties, system configuration, tool-path generation, etc. Among the above, trajectory control is one of the emerging and active areas of research. Generally, trajectories are developed offline for printing the parts. However, some of the major challenges involved in conventional trajectory development for LDED-PF are the propensity for collision between the deposition head/ nozzle and the part being built and challenges in building components with variable overhang.

The major goal of this work is the development of adaptive trajectory control of the LDED-PF process using online and offline techniques to build high-quality components. The work involves the offline trajectory development to build complex-shaped components with variable overhang angles by considering collision between the nozzle head and the part; adaptive layer thickness for higher dimensional accuracy. In addition, the work is extended to the development of online and intermittent trajectory control using a combination of in-situ surface quality monitoring and machine learning technique.

Offline trajectory planning is performed for two complex-shaped geometries such as a hemispherical dome and a bent pipe. Offline adaptive trajectory planning for hemispherical dome involves the development of an algorithm including the deposition parameters with variable overhang and collision checking, while the trajectory planning for building bent pipe structures

includes the deployment of adaptive slicing in addition to the collision check and overhang angle deposition. To manufacture the dome, the tilt angle is used to avoid the collision between the nozzle and previously built material with a condition that the tilt angle cannot exceed the maximum allowable overhang angle. The algorithm verifies the tilt angle suitable to build the dome and the angle is transferred from the tilt angle to the tilt angle of the rotary table. In order to build the bent pipe geometry, the variation in scanning speed is used to realize the adaptive slicing, which aids in having point-to-point variable layer height thereby permitting non-parallel deposition. In addition, changing the tool orientation during the deposition permits the manufacturing of support-free bent pipe parts as observed for dome structures. LDED-PF of the hemispherical dome and bent pipe was performed using the developed algorithms and the built geometries have good dimensional stability and density.

In the case of online trajectory planning, a novel in-situ monitoring software platform was developed for the online surface anomaly detection of LDED-PF parts using machine learning techniques. The above starts with the development of a novel method to calibrate the laser line scanner with respect to the robotic end-effector with sub 0.5 mm accuracy. Subsequently, 2D surface profiles obtained from the LDED-PF built part surface using the laser scanner are stitched together to create an accurate 3D point cloud representation. Further, the point cloud data is processed, and defect detection is carried out using unsupervised learning and supervised (deep) learning techniques. Further, the developed defect detection software platform was used to create an online adaptive toolpath trajectory control platform to correct the dimensional inaccuracies in-situ. It uses a laser line scanner to scan the part after the deposition of the definite number of layers followed by the detection of concave, convex, and flat surfaces using deep learning. Further, the developed adaptive trajectory planning algorithm is deployed by using three different strategies to

control material deposition on concave, convex, and flat surfaces. The material deposition is controlled by using adaptive scanning speed, and a combination of laser on-off and scanning speed. Subsequently, the built geometries are subjected to geometric, microstructure, and mechanical characterizations. The study offers an integrated and complete methodology for developing high-quality components using LDED-PF with a minimal dimensional deviation from the original CAD model.

## Acknowledgment

First and foremost, I would like to express my sincere appreciation to my supervisor, Professor Ehsan Toyserkani who provided a great opportunity for me to join his top-notch team and work in Multi-scale Additive Manufacturing (MSAM) lab. I appreciate greatly his support in providing magnificent facilities and a research environment in the MSAM lab. Similarly, I would like to thank the project sponsor, Mr. Mark Zimny, CEO of Promation Engineering for his great support of my research project and his leadership on this project.

I would like to thank Dr. Jinoop Arackal Narayanan for his support in material characterization and guidance on my research project. Jinoop helped me a lot in every aspect of my research work during the past years and shared his valuable knowledge and experience to help me during my PhD.

I was fortunate to work with Mr. Patrick Hallen and Mr. German Flicker from ModuleWorks GmbH who helped me a lot during these years and shared valuable knowledge and experience during my PhD project.

I want to thank all my colleagues at Promation Engineering for their support, especially Mr. Chris Barber, Mr. Derek Jarzak, Mr. Jathavan Sivanesan, and Mr. Ketul Shah.

Besides, I appreciate MSAM members who supported me in every aspect of my studies, Mr. Ali Zardoshtian and Mr. Henry Ma.

Besides, I thank my friends, Mitra Manouchehri, Saeedeh Mirjalili, and Ernest Namdar who assisted and supported me in every aspect of my life and studies.

Finally, I would like to profoundly appreciate the support of my family. My belated parents, Fatemeh and Jalal, My brother, Ahmad, and My sisters, Faezeh and Fahimeh. I would not be in this position without their support, encouragement, and love.

*Dedicated to*

*my beloved family*

# Table of Contents

# List of Figures

# List of Tables

# 1 Introduction

## 1.1 Motivation

Metal Additive Manufacturing (MAM), a disruptive technology, is revolutionizing industrial manufacturing through a unique combination of shape and material design freedom [1–3] uses a layer-by-layer manufacturing methodology to build metallic components directly from 3D model data. MAM is used to build complex-shaped metallic components with overhangs, undercuts, etc. that enable the fabrication of lightweight structures for various engineering applications. MAM primarily uses wire and powder as feedstock source [4-5].Among them, powder-based MAM is the most commonly used technique mainly due to the higher precision. Laser Directed Energy Deposition- Powder Fed (LDED-PF) is a MAM process that uses a moving laser heat source to create a melt pool on the surface of the substrate/ previously built layer onto which powder is added to deposit material as per the desired geometry. The material deposition is carried out in a layer-by-layer fashion to build 3D components. LDED-PF is also known by several names such as laser metal deposition, direct metal deposition, laser solid forming, laser engineered net shaping, etc[6]. LDED-PF permits the fabrication of components with desired density and high performance with tailored properties by manipulating the process parameters and conditions [7].

The quality and performance of LDED-PF-built components are dependent on several factors such as: process parameters, process conditions, feedstock properties, system configuration, tool-path generation, etc. In LDED-PF, the major process parameters that control the process quality are laser power, scanning speed, powder feed rate, shielding gas feed rate, powder particle size distribution, working distance, etc [8]. In addition to the above, the slight change in the process conditions such as variations in ambient temperature, humidity, etc. can influence the process

quality. The quality of feedstock governs the density of the part, mechanical properties, and minimum feature size of the LDED-PF built part [9]. The system configuration is significant in deciding the amount of design freedom that can be achieved with LDED-PF.

Among the above, trajectory control is one of the emerging and active areas of research. Generally, trajectories are developed offline for printing the parts. However, some of the major challenges involved in conventional trajectory development for LDED-PF are the propensity for collision between the deposition head/ nozzle and built part and challenges in building components with variable overhang. In order to manufacture complex parts with a high overhang angle using LDED-PF, the nozzle need to rotate to keep tangent to previous layers. This avoids the requirement of building support structures for geometries having high overhang angles. However, the above introduces the possibility of a collision between the deposition head, the substrate, or previously deposited layers. In addition, the trajectory may need to be adaptive to suit the geometry of the components with overhangs as it is challenging to build complex components with uniform slicing. Another challenge in trajectory development is the lack of dimensional accuracy due to heat accumulation and melt-pool overflow [10]. The rapid heating and cooling cycles during LDED-PF can lead to the induction of residual stresses and consequently distortions in the parts. Therefore, it is required to have in-situ process monitoring to understand the deviations in real-time [11]. Recently, the use of various vision systems including laser scanners, laser line profilers and stereo vision cameras are reported in the literature for in-situ assessment of LDED-PF parts [12-13]. Computer vision algorithms have been tested heavily on feature extraction and error identification on the LDED-PF parts and they have been proven to detect the surface defects of the LDED parts [14]. Subsequently, the prediction of the geometric defects and adaptive trajectory development can be used to improve dimensional accuracy.

## 1.2 Objectives

The major goal of this work is the development of adaptive trajectory control of LDED-PF process using online and offline techniques to build high-quality components. The work involves the offline trajectory development to build complex shaped components with variable overhang angles by considering collision between the nozzle head and built part; adaptive layer thickness for higher dimensional accuracy. In addition, the work is extended to the development of online and intermittent trajectory control using a combination of in-situ surface quality monitoring and machine learning technique. This is further used for developing the intermittent repair trajectory to improve the surface quality of the LDED parts.

In order to achieve this goal, the objectives of this research are defined as follows:

a) Development of collision-free offline adaptive trajectory planning for building components with variable overhang angles and characterization of the built parts.
b) Development of offline trajectory planning using adaptive slicing technique to build parts with variable overhangs followed by geometrical and material characterization of the built parts
c) Development of machine learning technique for in-situ surface quality assessment of LDED-PF built parts.
d) Development of an online adaptive tool path platform for LDED-PF and extensive geometrical, microstructural, and mechanical characterizations on the built parts.

## 1.3 Outline

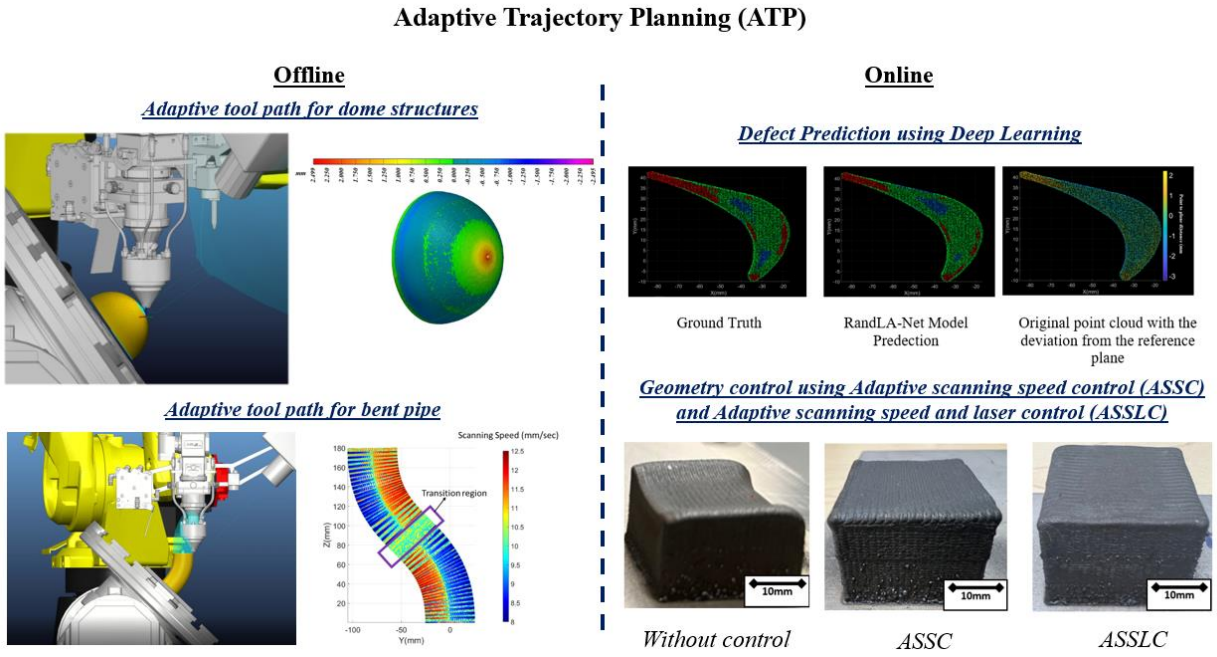


This thesis consists of eight chapters. The first chapter includes the introduction, motivation and objective of the thesis. Chapter two is dedicated to the short literature review on metal additive manufacturing, LDED-PF and adaptive trajectory planning. Chapter three outlines the architecture of the in-house developed LDED-PF system, all the experimental process parameters and characterization techniques and settings. At the beginning of chapters 4-7, a short literature survey related to the objectives of the associated chapter is provided.

The fourth chapter is a journal article published in the journal of Additive Manufacturing Letters:

- F. Kaji, A. N. Jinoop, M. Zimny, G. Frikel, K. Tam, and E. Toyserkani, "Process planning for additive manufacturing of geometries with variable overhang angles using a robotic laser directed energy deposition system," *Addit. Manuf. Lett.*, vol. 2, p. 100035, 2022, doi: https://doi.org/10.1016/j.addlet.2022.100035 [1].

[1] The copyright permission is provided in the Letters of Copyright Permission section

The fifth chapter is a journal article published in the journal of Additive Manufacturing:

- Farzaneh Kaji, Arackal Narayanan Jinoop, Ali Zardoshtian, Patrick Hallen, German Frikel, Mark Zimny, Ehsan Toyserkani, "Robotic Laser Directed Energy Deposition-based Additive Manufacturing of Tubular Components with Variable Overhang Angles: Adaptive Trajectory Planning and Characterization", Addit. Manuf., vol. 61, 103366, 2023, doi: https://doi.org/10.1016/j.addma.2022.103366 [2].

The sixth chapter is a journal article published in the Journal of Manufacturing Processes:

- Farzaneh Kaji, H. Nguyen-Huu, A. Budhwani, J. A. Narayanan, M. Zimny, and E. Toyserkani, "A deep-learning-based in-situ surface anomaly detection methodology for laser directed energy deposition via powder feeding," *J. Manuf. Process.*, vol. 81, pp. 624–637, 2022, doi: https://doi.org/10.1016/j.jmapro.2022.06.046 [3].

The seventh chapter is a journal paper submitted to the Journal of Optics and Laser Technology:

- Farzaneh Kaji, H. Nguyen-Huu, Arackal Narayanan Jinoop, M. Zimny, and E. Toyserkani, Intermittent Adaptive Trajectory Planning for Geometric Defect Correction in Robotic Laser Directed Energy Deposition-based Additive Manufacturing.

Chapter eight includes the conclusions and future work, Figure 1-1 shows the structure of the thesis

[2] The copyright permission is provided in the Letters of Copyright Permission section
[3] The copyright permission is provided in the Letters of Copyright Permission section

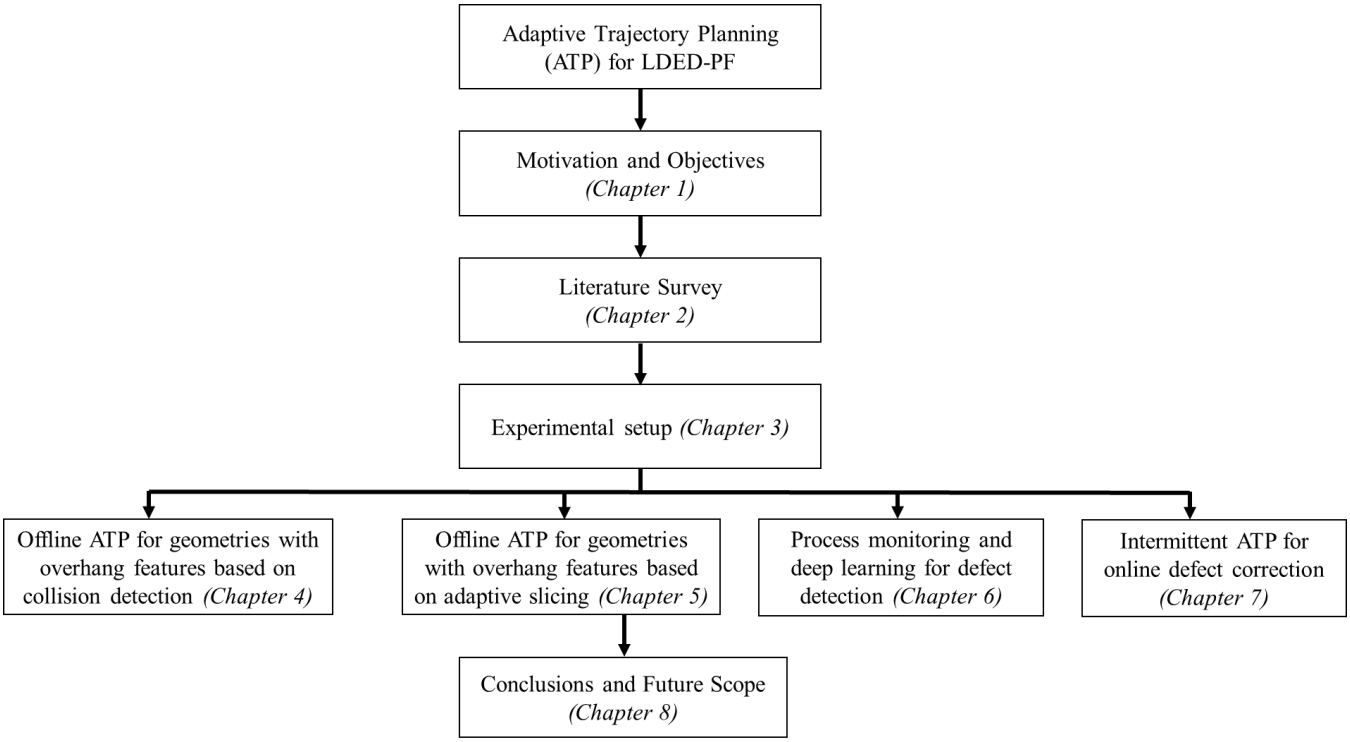


*Figure 1-1: Structure of the thesis*

# 2 Literature Review and Background

## 2.1 Introduction

This chapter provides a brief literature survey in general. Specific and detailed literature review will be provided in chapters 4-7.

## 2.2 Metal Additive Manufacturing

Additive Manufacturing (AM) is a growing technique for processing polymers, metal, and ceramics using layer by layer deposition. It is a direct form of manufacturing to build complicated geometries with minimal wastage [17–19] AM is also a new paradigm for the design and manufacturing of high-performance components for medical, energy, automotive and aerospace applications [19–23].

Among the seven AM processes as per ASTM/ ISO classification, the most commonly used Metal Additive Manufacturing processes are Laser Powder Bed Fusion (LPBF), and Laser Directed Energy Deposition (LDED) [22].

### 2.2.1 Laser Directed Energy Deposition (LDED)

In LDED, a high power laser (e.g., Disk, Fiber, $CO_2$ or Nd:YAG) is used to create a melt pool onto which the feedstock material (wire or powder) is added to deposit a layer. The most commonly used LDED technique is LDED-Powder Fed (LDED-PF), where the metal powder is injected into the melt pool using a powder nozzle in the presence of the shielding gas or inert atmosphere as shown in Figure 2-1. The advantages of LDED-PF include near-net shape manufacturing of high-value and complicated components, manufacturing of functionally graded materials, in-situ alloying, and free-form fabrication [25–27].

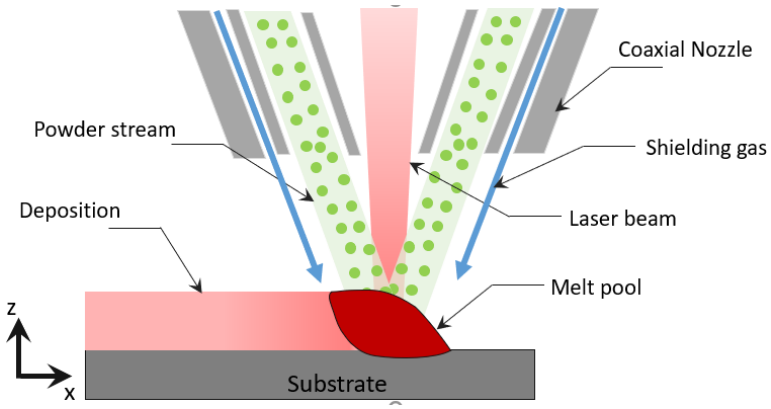


*Figure 2-1 Schematic of LDED-PF Process*

*Table 2-1. Comparison of LPBF and LDED-PF Processes*

| Feature | LPBF | LDED |
|---|---|---|
| Material addition | Pre-placed powder bed [26] | In-situ feeding [24] |
| Layer height | Micron-scale [27] | mm scale [28] |
| Surface Finish | Medium [29] | Low [32–35] |
| Design complexity | Unlimited [34] | Limited [35] |
| Multi-material components | Restricted freedom [36] | Possible [36-37] |
| Overhang Structures | Possible [39] | Limited [40] |
| Support structures | Mainly required [41] | Mainly not required [42] |

Table 2-1 presents a comparison between LDED-PF and LPBF processes. Thus, the major advantages of LDED-PF technology are the higher build rate and multi-material freedom. In addition, due to its ability to join dissimilar materials, provide large area coating with minimal dilution, good metallurgical bond and low distortion levels, the technology has been widely used as compared to other joining and coating techniques such as laser welding, thermal spraying, etc.

As compared to other DED counterparts such as wire-arc DED and electron beam DED, LDED-PF has the advantages of better precision and accuracy leading to the development of components having dimensions close to the original design, paving the way for near-net-shaped parts [43]. It also provides a smaller heat-affected zone and better surface quality. LDED-PF also provides opportunities to build free-form complicated geometries using advanced five-axis toolpath planning by reducing the time to market for prototyping and new product developments [44-45].

On the process side, LDED-PF is a non-equilibrium thermodynamic process that entails very rapid heating and cooling rates often in the order of the $10^3\ K/s$ or even more [46]. The major process parameters for LDED-PF are laser power (*P*), powder feed rate (*F*), scanning speed (*V*), and laser spot size (*d*) [47].A diverse set of process parameters coupled with complex heat transfer including conduction to the substrate, convection to the surrounding atmosphere, evaporation and radiation makes it difficult to understand the effects of process parameters on the overall quality of the LDED-PF process individually [48].Thus, combined process parameters such as laser energy density (LED) and powder fed per unit length (PFL) are used to correlate the process parameters with deposit quality. Equations *2-1* and 2-2 are used to calculate LED and PFL, respectively.

$$LED = \frac{P}{Vd} \qquad 2\text{-}1$$

$$PFL = \frac{F}{V} \qquad 2\text{-}2$$

## 2.3 Advantages and Limitations

The various advantages of LDED-PF are as follows:

a) LDED-PF can manufacture metallic parts with desired density and excellent material properties [49].
b) Compared to traditional welding, LDED-PF can result in lower residual stresses, especially for joining dissimilar materials [50].
c) LDED-PF can be used to join dissimilar materials by creating a smooth transition in the composition of the materials based on the position using the gradient path. This avoids the formation of detrimental phases and sharp interfaces, which can increase joint strength and life [51].
d) LDED-PF can be used for multi-axis deposition using 5-axis CNC machines and robotic systems, making it possible to deposit the material in different orientations. This can provide opportunities to manufacture the components with overhang features without using support structures [52]. Robotics systems show great flexibility for LDED-PF since they provide additional degrees of freedom, if required. LDED using robotics also provides a larger build volume due to the high reachability of the robotic arm. It makes them the best candidate for manufacturing large-size components [53].

Despite all the benefits of the LDED-PF, the process has some limitations. Some of the limitations of LDED-PF are:

a) Being a very rapid thermal process with high complexities, LDED-PF suffers from a lack of repeatability [44].

b) A significant number of experiments are required for establishing the toolpath efficiency and process parameters to achieve the desired density and geometrical stability [54]
c) For parts with complex features, multiple iterations are required to optimize the process parameters for achieving the desired dimensional accuracy and material properties [55].
d) The surface roughness and dimensional accuracy of LDED-PF parts are lower than LPBF processes mainly due to larger met-pool size and higher energy density [56].
e) Fabrication of thin wall structures is challenging [57].

Therefore, manufacturing parts with desirable dimensional accuracy and material properties is time-consuming and expensive using LDED-PF. Thus, modelling techniques such as finite element analysis (FEA) and controlled LDED-PF are being used recently to address these issues and they are still active areas of research in LDED-PF [58-59].

## 2.4 Applications

### 2.4.1 Near-net shape Manufacturing

One of the main applications of LDED-PF is the manufacturing of near-net-shape components for various industries, especially when the application requires hard-to-machine materials. Machining hard materials is a slow and costly process. The machining speed can be accelerated, and cost can be reduced by using LDED-PF, which aids to build the near-net-shaped component and final finishing can be done using traditional subtractive manufacturing. Some examples include the development of Titanium brackets for aerospace applications [60-61].

### 2.4.2 Large area cladding

Cladding is mainly used to develop a high-performance coating on a part surface with strong metallurgical bonding and controlled dilution. Cladding aids to improve the properties of the

component by improving its surface hardness, corrosion resistance, wear resistance, oxidation resistance, etc. to increase the lifetime of the component [62-63]. Multi-axis cladding using LDED-PF permits the cladding of the interior surface of pipes and elbows and surfaces that have non-planar curvatures as shown in Figure 2-2(a).

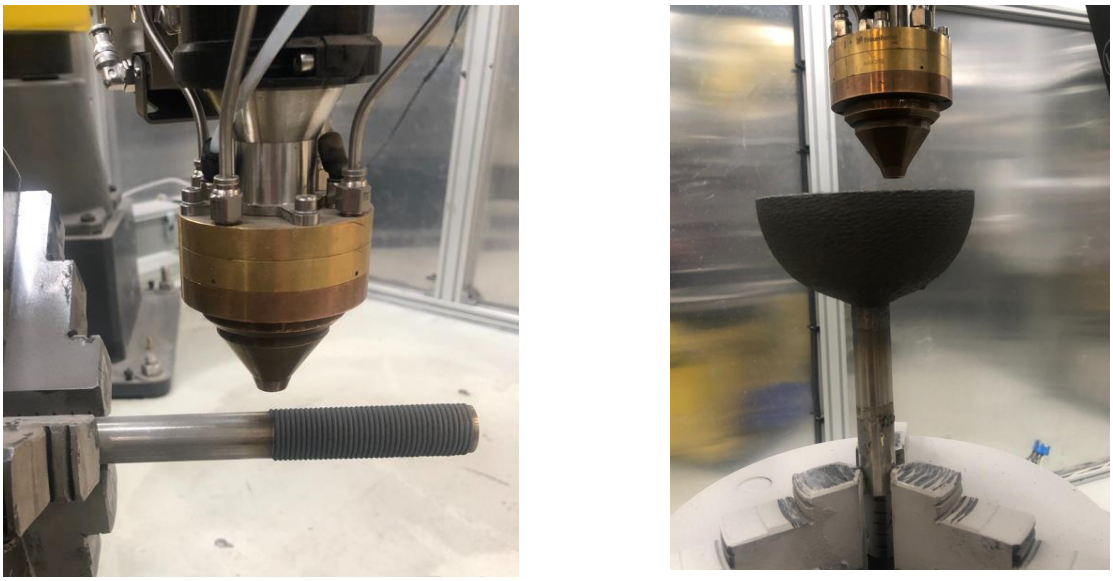

(a) (b)

*Figure 2-2: Applications of LDED (a) Cladding on an SS316 shaft (b) Building features on the existing parts*

### 2.4.3 Feature Addition

LDED-PF can be used to add features to the existing parts, and it is beneficial when the required features are expensive to build using conventional manufacturing techniques. The features can be the same material as the substrate, or new material, which is metallurgically compatible with the base material [64]. An example of a feature addition application is shown in Figure 2-2(b).

### 2.4.4 Repairing or remanufacturing

Repairing/Remanufacturing is one of the most common applications of the LDED-PF, especially in the aerospace and nuclear industries. In the case of high-value components, repairing a worn-out high-value part is more cost-effective than manufacturing a new part. Some of the main examples of repair using LDED-PF are repairing the jet engine gas turbine blade using Ni-based superalloys, repairing the manufacturing molds, etc. [65–67].

## 2.5 Challenges and opportunities

LDED-PF has the potential to replace/ compliment conventional manufacturing in several sectors. However, the process limitations offered by the technology such as lack of dimensional accuracy slow down the wide implementation of the technology. In addition, conventional slicing techniques used for trajectory planning are not yet robust enough to support automatic collision avoidance and variable layer height deposition. The above techniques are necessary to build components with complex shapes and variable overhangs. In addition, during the component fabrication, dimensional inaccuracies are introduced by the thermal cycling, acceleration and deceleration in turns and corners, and laser and powder stream defocusing. Adaptive trajectory planning and control are also required to measure the deviations during the build and develop remedial strategies to reduce the dimensional deviations.

## 2.6 Summary

In this chapter, LDED-PF process, its advantages, limitations, and application were discussed. This research aims to address the limitations of conventional trajectory planning and propose remedial measures to build complex geometries with improved dimensional accuracy. To conquer the above-mentioned challenges, an adaptive collision avoidance technique is introduced in Chapter 4

and an adaptive slicing algorithm for non-uniform layer height deposition is discussed in chapter 5. The dimensional accuracy is addressed by developing a deep learning-based framework to detect the geometrical defects in chapter 6 followed by an adaptive intermittent dimension correction platform to improve the dimensional accuracy in chapter 7.

# 3 Fabrication and Experimental Methodologies

## 3.1 Introduction

In the previous chapters, a short literature review is carried out, gap areas are identified, and objectives are defined. In the present chapter, a discussion on the powder characterization, LDED-PF experimental system, process parameters, and characterization system used for the experiments are presented.

## 3.2 Material

The experiments are carried out by using gas atomized SS 316L powder provided by Carpenter Additive. SS 316L powder is mainly spherical with fine satellites attached to the surface of powder particles as shown in Figure 3-1(a). The powder particle size distribution obtained from the laser particle size analyser is presented in Figure 3-1(b) and the D10, D50 and D90 values are 19.66 µm, 29.54 µm and 44.08 µm, respectively. The powder composition is confirmed using Energy Dispersive Spectroscopy (EDS) and the elemental composition is presented in Figure 3-1(c) and Table 3-1.

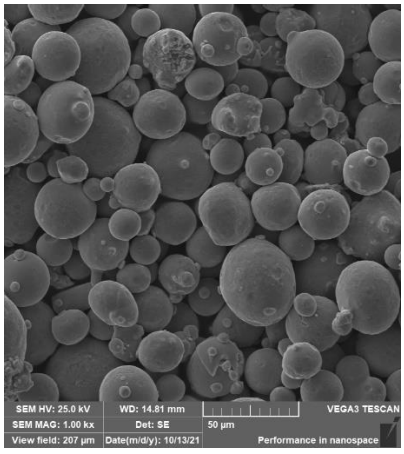


(a)

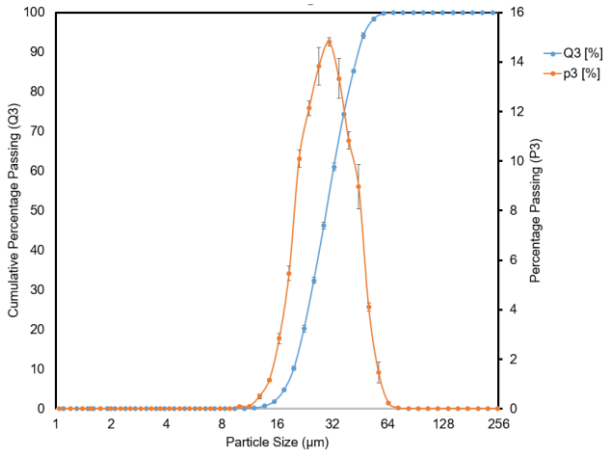


(b)

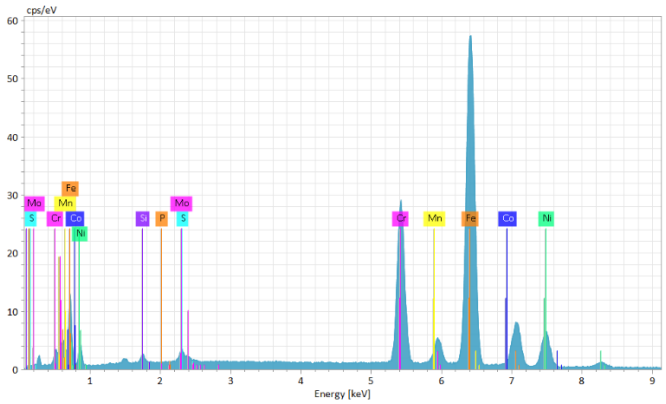


(c)

*Figure 3-1: SS 316L powder (a) Morphology (b) particle size distribution (c) composition (d) material composition*

*Table 3-1: Composition of SS316L powder*

| **Element** | Iron | Chromium | Nickle | Molybdenum | Manganese | Silicon | Cobalt | Sulfur |
|---|---|---|---|---|---|---|---|---|
| **Mass %** | 65.23 | 18.77 | 11.37 | 2.13 | 1.48 | 0.52 | 0.35 | 0.10 |

## 3.3 Laser Directed Energy Deposition -Powder Fed (LDED-PF) system

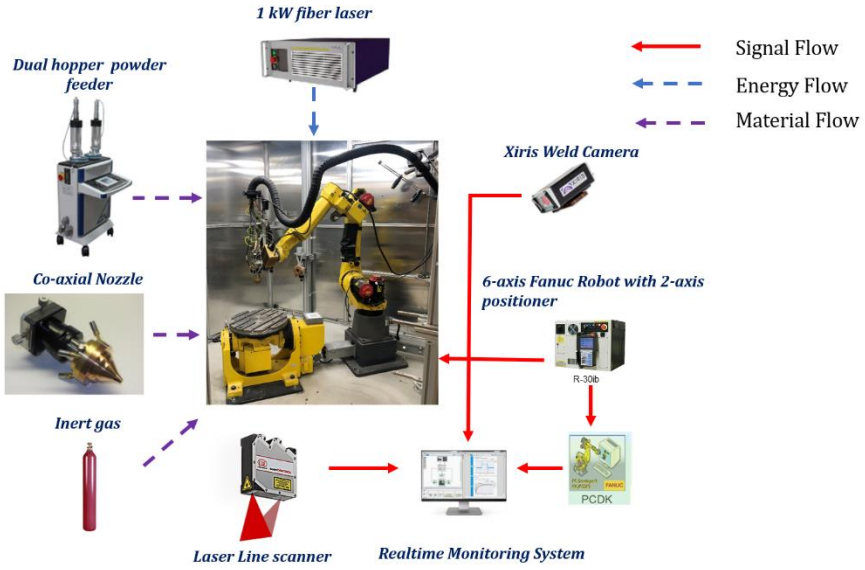


*Figure 3-2: Schematic representation of the in-house LDED-PF system and the flow of material, energy and signals*

Figure 3-2 presents the in-house developed robotic LDED-PF system used for the present research work. The main components of the system are listed below:

a) 6-axis Fanuc M-20iA arm with the repeatability of $\pm 0.1\ mm$ with 2-axis servo positioner H875 and a maximum payload of 500 kg. The robot and the servo positioner are controlled by R30iB controller.

b) Micro-Epsilon scanCONTROL 2950-100-BL line laser profiler as shown in Figure 3-3(a), mounted on the end effector for scanning the components. It has a measuring range of 265 mm in the z-direction and 143 mm in the x-direction. The resolution is 18 µm with a maximum of 2000 Hz. It is rigidly mounted on the robot 6$^{th}$ axis using a bracket as shown in Figure 3-3(b).

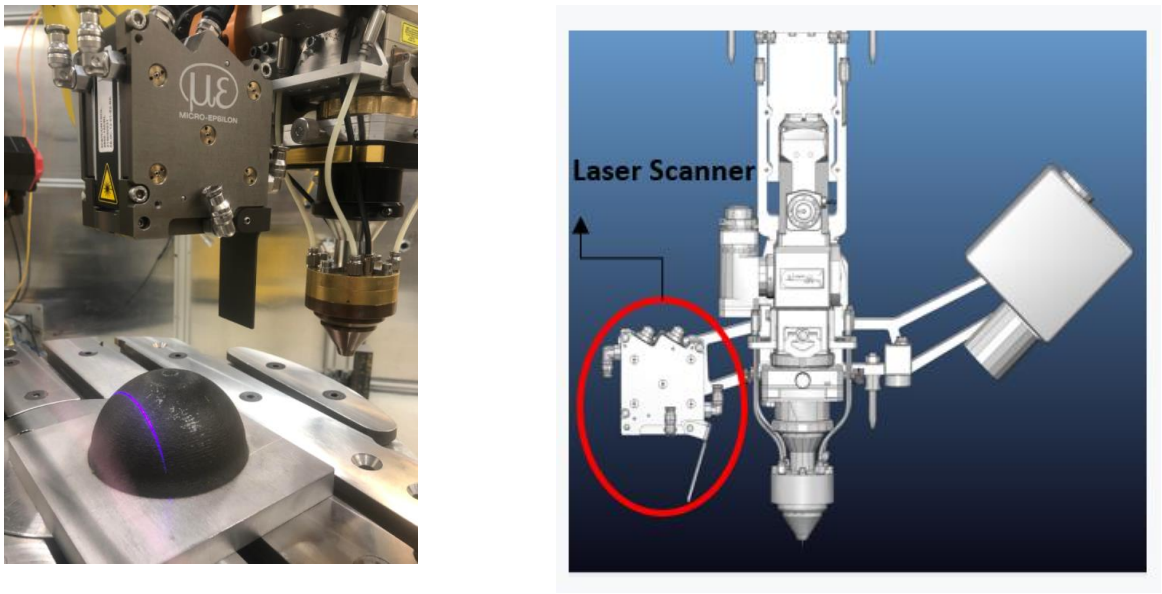


(a) (b)

*Figure 3-3: (a)The mounted laser scanner sensor on the robot, (b) Laser scanner sensor mounting position based on the CAD model*

c) IPG CW YLS-1000 fiber laser source with maximum laser power of 1 kW, laser beam wavelength of 1069 nm and the spot size of 1.2 mm
d) Dual hopper GTV powder feeder is used to deliver the powder using a carrier gas (Argon) to the meltpool
e) Fraunhofer Coaxial nozzle COAX-14 with 4 powder ports
f) In-house developed PROERA 3D CAD/CAM software was used for the tool-path planning

### 3.4 Robot and Positioner setup

The tilt angel of the nozzle will adversely affect the deposition quality due to the effect of gravity on the powder stream in tilted position of the nozzle [68]. The nozzle manufacturer also recommends the maximum tilt angel of 15° [69]. The positioner is used to transfer the tilt angel of the nozzle to the base plate to overcome the limitation of tilt angel of the nozzle.

The 2-axis Fanuc positioner is used for periodic positioning of the workpiece for effective reach or access for manufacturing processes. Fanuc motion planner provides a coordinated motion option which maintains the absolute relative speed between the Tool Center Point (TCP) and the Tool frame of the positioner.

A coordinated motion setup and calibration are required to calculate the position and orientation of the TCP of the positioner [70]. Since the positioner is made by FANUC, a known four-point calibration method can be used [62]. Once the positioner TCP is found, a coordinated pair is set up using the active TCP of the robot. It means that when coordinated motion is used, the TCP of the robot (laser focus point) maintains the absolute velocity and position with respect to the TCP of the positioner. It simply means that if the positioner is rotated in a particular direction, the laser head rotates in the opposite direction. This means to be able to print the parts predominantly using

the external axis, the position and orientation of the laser TCP must be calculated and continuously get updated to maintain the relative position and orientation with respect to the positioner TCP.

The position of the TCP in the FANUC H875 is located at the cross-section of the $E_1$ and $E_2$ as shown in Figure 3-4. The kinematic relationship between the positioner TCP and laser TCP is shown in Figure 3-4. The rotation matrix between the positioner TCP and laser TCP can be expressed in Equation 3-1, where $R_{TB}$ is the $3 \times 3$ rotation matrix between the positioner tool frame and the base userframe (which is located at the corner of the substrate), and $R_{Bl}$ is the rotation matrix between the base userframe and the laser TCP which is computed during the toolpath generation process.

$$R_{Tl} = R_{TB} \times R_{Bl} \qquad 3\text{-}1$$

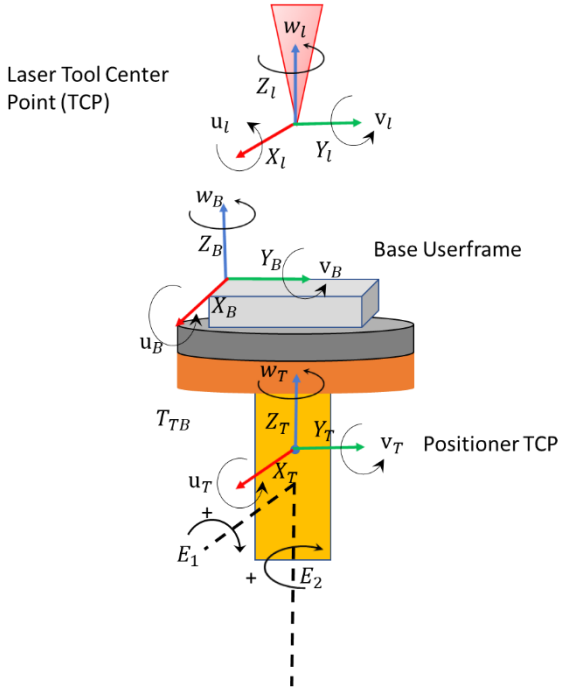


*Figure 3-4: Kinematic relationship between the positioner and laser TCP*

$R_{TB}$ can be presented as Equation 3-2.

$$R_{TB} = R_{TE_1} \times R_{E_1E_2} \times R_{E_2B} \quad 3\text{-}2$$

where, $R_{E_2B}$ is the rotation matrix between the base user frame and the new frame obtained from the rotation of positioner TCP in $-E_1 \times E_2$ direction.

FANUC convention uses the right-hand rule and Euler angles of (u,v,w) which are intrinsic rotations around the X, Y and Z axis, respectively, to calculate the reference frames rotation matrix [71]. The rotation matrix is then calculated using Equation 3-3.

$$R = R_Z(w) \times R_Y(v) \times R_X(u) \quad 3\text{-}3$$

$R_{TE_1}$ and $R_{E_1E_2}$ can be rewritten as Equation 3-4 and Equation 3-5.

$$R_{TE_1} = R_{X_T}(-E_1) \quad 3\text{-}4$$

$$R_{E_1E_2} = R_{Z_T}(E_2) \quad 3\text{-}5$$

The kinematic links of the robot and positioner reside inside the in-house developed toolpath planning engine (PROERA 3D), and it is used to compensate for the laser TCP orientation when the positioner axes are selected as the priority axes.

## 3.5 Process Parameters

Single track experimental trials are carried out by varying the laser power, scan speed, powder feed rate, and shielding gas flow rate. The range of process parameters that yielded continuous deposition is selected for the study. Table 3-2 presents the range of process parameters deployed for the present study.

*Table 3-2: Process parameters used for the experiments*

| | |
|---|---|
| Laser power | 500 - 800 W |
| Powder feed rate | 5 - 12 g/min |
| Scanning speed (deposition) | 4 - 20 mm/sec |
| Shielding gas flow rate | 10 - 15 slpm |
| Laser beam diameter | 1.2 mm |

## 3.6 Characterization

### 3.6.1 Geometrical Analysis

The built parts are scanned using the optical scanner (Make: HEXAGON; Model: AICON SmartScan). The scanning was performed using an S-350 mm lens having a field of view of 260 × 205 mm. Scanning data acquisition was performed using OptoCat 2018R3 software, and the point cloud data was converted to an STL file using a triangulation accuracy of 0.005 mm. Subsequently, the CAD model and the scanned STL file are imported in PolyWorks|Inspector™. In order to analyze the geometrical deviation, automatic alignment is performed. The automatic alignment aids in aligning the CAD model and STL file and to overlay the CAD model of the component with the scanned STL data. To measure the geometrical deviation from the intended dimensions, a CAD to the part comparison was performed.

### 3.6.2 Density analysis

The samples are hot-mounted, and ground and polished using an automatic polisher (Make: Struers; Model: LaboPol-20). The mirror-finished sample surface is observed using a digital microscope (Make: Keyence; Model: VK-X250) to check the presence of defects. The density of

the samples (ρ) was measured using the Archimedes density analyzer (Make: GAOTEK; Model: GT00WI00ZV) using Equation 3-6.

$$\rho = \frac{W_D \rho_w}{W_D - W_w} \qquad 3\text{-}6$$

where $W_D$, $W_w$ and $\rho_w$ are the dry weight, wet weight, and density of distilled water, respectively. The density of each sample was measured three times to obtain the average density values. The density of standard SS316L is measured as 7.9 g/cc to calculate the relative density.

X-ray computed tomography (CT) was performed using a Sub-micron CT Scanner (Make: ZEISS; Model: Xradia 520 Versa) to understand the distribution of the pores in the built samples. The parameters used for the CT scan are as follows: number of projections: 1601, Voltage: 140 kV, and exposure time: 1.0 second per image with the voxel size of 5 - 6 µm. Reconstruction is performed using a beam hardening constant of 0.05, and the obtained images were post-processed and analyzed in Dragonfly 3.1.

### 3.6.3 Microstructure and Micro-hardness

Further, the polished samples are chemically etched using Kalling's2 ($CuCl_2$ 5gm + HCL 100ml + $C_2H_6O$ 100ml) reagent to reveal the microstructural features. The microstructure of the samples is analyzed using a scanning electron microscope (Make: TESCAN; Model: VEGA3) at an HV of 15 kV. Microhardness measurements are taken using a Vickers automated hardness tester (Make: CLEMEX; Model: CMT) by applying a load of 300 gm for a dwell period of 15 s.

## 3.7 Summary

In this chapter, powder characteristics, experimental setup, process parameters, and characterization tools were presented. The subsequent chapter deals with process planning for LDED-PF of components with overhang features.

# 4 Process planning for LDED-PF of components with overhang features

## 4.1 Introduction

In this chapter, a novel LDED-PF process planning methodology is proposed to build a dome structure with variable overhang angles. Overhang structures with different overhang angles were built where the maximum angle of 35° can be used to build overhang structures without the process and structure compromise. The thin-wall hemispherical dome built using the developed methodology shows a maximum deviation of 2% with respect to the diameter of the original CAD model data. The study paves a way for building high-value, lightweight thin-walled structures with complex cylindrical-based shape (e.g., storage tanks, nozzles, combustion chambers) for engineering applications.

## 4.2 Literature review

LDED-PF enables the fabrication of lightweight and complex-shaped structures, which requires process-specific planning and strategy development. LDED-PF systems often use three-axis or five-axis configurations to build intricate components. However, increasing focus on the deployment of five-axis configuration is seen recently due to improved freedom to build complex shaped components with overhang feature [68–70]. Overcoming the challenges of overhanging features is easier in LPBF compared to LDED-PF due to support material generation [41], however, the size of the parts printed using LPBF is limited [75], therefor, 5-axis toolpath planning in LDED-PF is used to facilitate the fabrication of large-scale components with overhanging features. The five-axis configuration allows the nozzle to remain tangent to the surface, which eliminates the need for support structures to build features having a larger overhang angle ($\alpha$)[76].However, this configuration increases the process complexity and probability of collision

between the nozzle and substrate/ previously deposited layers. It is critical to avoid collisions that can damage the LDED-PF nozzles as they are costly and collision sensitive. In addition, focusing on the overhang features is a critical matter for the LDED and extrusion processes. The evaluation of the maximum overhang angle ($\alpha_{max}$) is critical and once the $\alpha$ exceeds the maximum limit, the structure collapses due to a lack of force balance between gravitational forces, surface tension, and capillary forces [77]. Researchers have investigated the fabrication of thin-wall structures with overhang features such as dome structures, which is challenging primarily due to the continuously changing $\alpha$ in two directions and the chances of collision between the nozzle and previously built layers [78]. Kalami et al.[79]. encountered nozzle collision issues while building a dome structure and used the geometrical partitioning method for successful fabrication. However, the transition region between the partitions shows large surface irregularities, which increases the roughness values significantly in these regions [80] . A combination of multi-directional segmentation and single-directional slicing was carried out by Xiangping et al. for building overhang structures [81]. Prahar et.al developed a novel slicing algorithm to tilt and rotate the build platform to avoid support structure using a robotics FDM setup [82]. Thus, the process methodology for building overhang structures using LDED-PF is limited to geometrical partitioning or segmentation.

The literature indicates that there are limited published works available on the development of tool paths for building overhang components such as dome structures in a single step. The present work proposes a novel approach based on the identification of maximum allowable overhang angle and collision detection interactively to directly build the dome structures in a single step, which can pave way for building complex and lightweight components using LDED-PF.

## 4.3 Developed Methodology for Dome Structures

LDED can take advantage of 5-axis techniques such as lean (tilt) and lead angles to avoid collision between the nozzle and the built parts. It must be considered that the lead angle must not exceed the $\alpha_{max}$ [78] as large values of $\alpha$ may result in lack of support for melt pool leading to molten material collapse. Lean (Tilt) angle is the orientation of the nozzle measured in the plane perpendicular to the deposition direction as shown in Figure 4-1(a), where *D* is the deposition direction, *N* is the substrate normal vector, and *B* is the Cross product of *D* and *N*. Lean angle is defined as the orientation of the nozzle measured in the plane parallel to the deposition direction as shown in Figure 4-1(b). When the nozzle tilts in the B-N surface, the angle is called lean (tilt) angle, and when the nozzle leans in the D-N surface it is called lead angle.

To manufacture a dome in a single step using LDED, in this work, the tilt angle is used to avoid the collision between the nozzle and previously built material while keeping in mind that the tilt angle cannot exceed $\alpha_{max}$ . In Figure 4-1(c), $\vec{b}$ is the deposition direction and $\overrightarrow{N_c}(p)$ is the surface normal direction to the surface at the point P. The relationship between the $\vec{b}$ and $\overrightarrow{N_c}(p)$ is $\overrightarrow{N_c}(p).\vec{b} = 0$ to ensure that the deposition can be supported fully by the previously built layers. However due to partial support from previous layers, the deposition range can be extended as shown in Equation 4-1.

$$-\sin \alpha_{max} \leq \overrightarrow{N_c}(p).\vec{v} \leq 0 \qquad 4\text{-}1$$

where, $\alpha_{max}$ , a function of $\frac{\Delta d_{max}}{\Delta l}$, is the maximum allowable overhang angle along the deposition direction of $\vec{b}$, $\Delta d_{max}$ is the maximum offset value that a new layer can overhang from the previous layer without melt pool collapse, and $\Delta l$ is the layer thickness.

Figure 4-1 (d) and (e) presents the schematic indicating the variation in $\alpha$ in the dome and flowchart of the developed methodology, respectively. Initially, the geometry is prepared, which includes the creation of a surface model [78-79]. Subsequently, the $\alpha_{max}$ is given as the input and the starting tilt angle is 0° in the beginning. The input track width and height are used to generate the stock model of the deposited material and the collision of the stock model versus the nozzle head is performed within the interface of PROERA 3D. If the collision is not detected, the toolpath will be generated in the robot native language. If the collision is detected (refer to Figure 4-1(f)), the tilt angle will be increased, and the toolpath will be re-generated. This continues until the methodology converges to the tilt angle that avoids the collision.

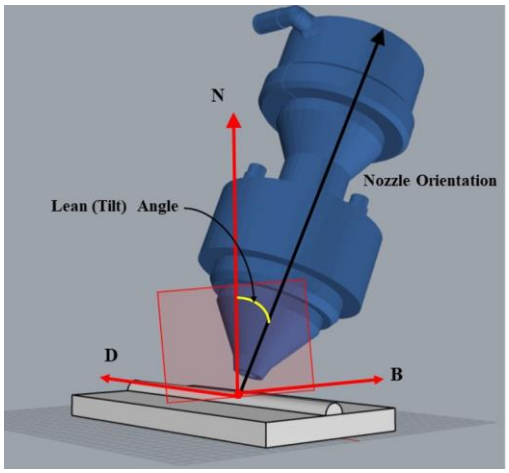


(a)

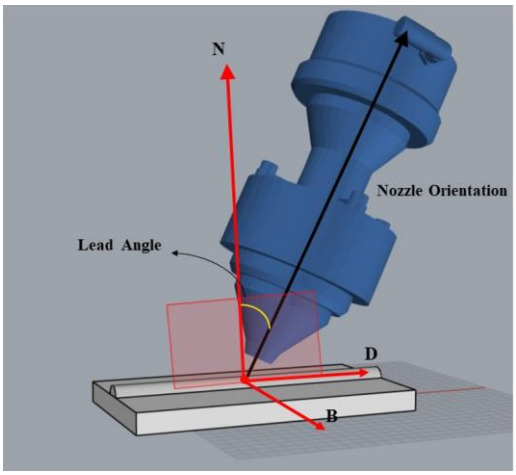


(b)

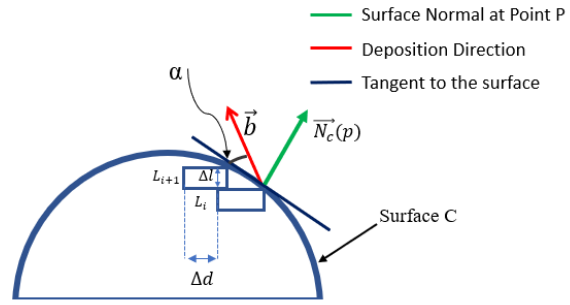


(c)

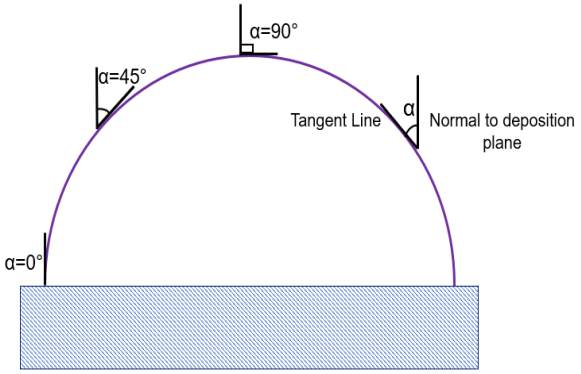


(d)

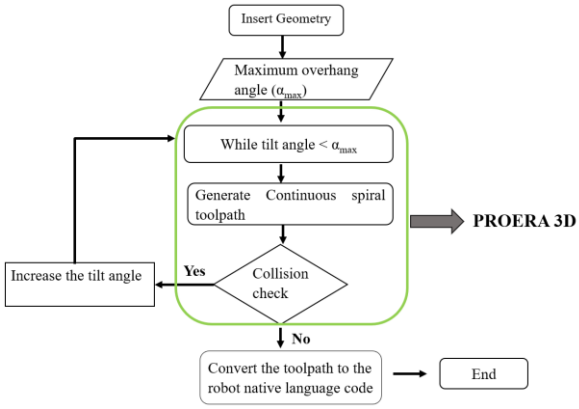


(e)

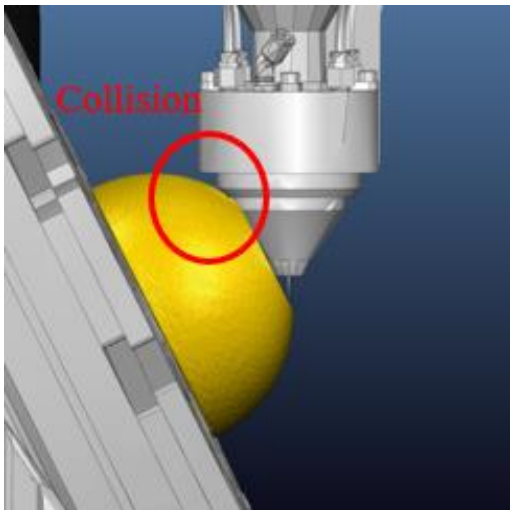


(f)

*Figure 4-1: Dome structure using LDED (a) lead angle schematic (b) lean angle schematic (c) deposition direction and surface normal (d) Varying α for a typical dome (e) algorithm (f) collision issue*

## 4.4 Results and Discussion

Figure 4-2(a) presents the schematic of the overhang structures and photographic view of built cones, respectively. The overhang cone geometry was built by laying overlapped tracks one over the other by shifting the laser spot center as per the required angle. As discussed in the previous section, the primary data for developing the methodology is the $\alpha_{max}$. It was observed the $\alpha_{max}$ of

35° can be used to build cone structures of height 20 mm without the material collapse as the melt pool becomes asymmetrical and collapses when the $\alpha$ exceeds 35º. This can be mainly due to the imbalance between the gravitational forces, viscous forces, and surface tension. The 35º overhang will result in an offset value of 0.4 mm as per Equation 4-2 based on the nominal track height and a track width of 0.5 mm and 1.5 mm, respectively (obtained from process parameter setting).

$$\tan \alpha_{max} = \frac{\Delta d}{\Delta l} \qquad 4\text{-}2$$

Figure 4-2(b) presents the cross-sectional images of cones built with 5-degree, 20 degree, and 35 degree overhang angle. It is observed that the built structures are crack-free and micro-pores are mainly seen along the cross-section. The micro-pores are primarily spherical, with the presence of a few irregular pores. The spherical and irregular pores are mainly due to gas-porosity and lack-of-fusion porosity, respectively. Gas porosity is generated primarily due to gas entrapment inside the melt-pool during solidification. It can also be due to the presence of porosity inside the powder particles, which are generated during powder manufacturing. These pores get transferred to the built part during the fabrication. On the other hand, a lack of fusion porosity is generated due to the insufficient bonding at isolated locations due to insufficient heat input and/or unexpected disturbances during LDED. An increase in the number of lack of fusion pores are seen with increase in overhang angle, which is primarily due to increase in the melt-pool instability at higher overhang angles [45-46].

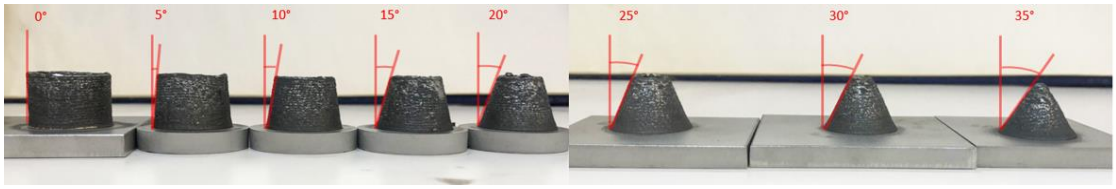


(a)


**5-degree overhang cone**

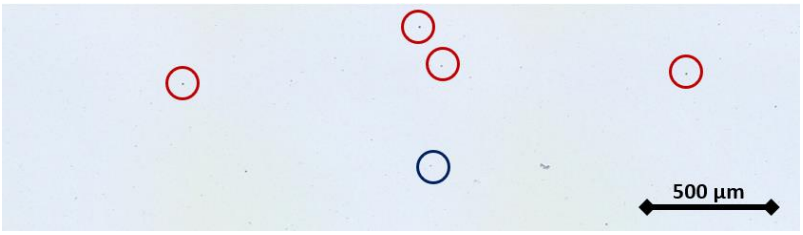


**20-degree overhang cone**

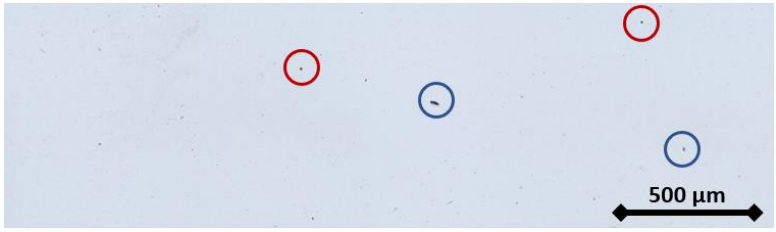


**35-degree overhang cone**

**Gas porosity**

**Lack of fusion porosity**

(b)

*Figure 4-2: LDED of overhang structures (a) Schematic (b) photographic view*

Further, the deposition is simulated (refer to Figure 4-3(a)) and carried out as per the required machine configuration (refer to Figure 4-3(b)). The algorithm verifies that a tilt angle of 32.5º will be suitable to build the dome using the rotary setup. Further, the angle is transferred from the tilt angle to the tilt angle of the rotary table. The orientation of the nozzle is perpendicular to the previously built layer up to 57.5º and the tilting start at this point. The $\alpha$ varies from 0 to 32.5º from the bottom layers to the top of the dome as shown in Figure 4-3(c). $\alpha_1$, $\alpha_2$ , and $\alpha_3$ shows the angle between the normal to the previous layer direction and the nozzle at different curvature angles in the dome at different positions. For the initial layers, $\alpha_1$ is 90º indicating that the nozzle is normal to the previously built layer, while at the top layers $\alpha_3$ is 57.5º and the corresponding α at the top of the dome is equal to $\beta_3$ (Maximum tilt angle), which is equal to 32.5º. Figure 4-3(d) presents the photographic view of the built dome structure and it can be seen that deposition is uniform with reduced surface irregularities as opposed to ones built with partitioning [41][85]. A comparison with the CAD model (refer to Figure 4-4) shows the uniform surface quality and good agreement with the intended dimensions. The deviation is lower than 0.5 mm at the lower to middle layers and the maximum deviation of ~ 1.5 – 2 (about 2% of the dome diameter) mm is observed at the top layers primarily due to the higher degree of overhang.

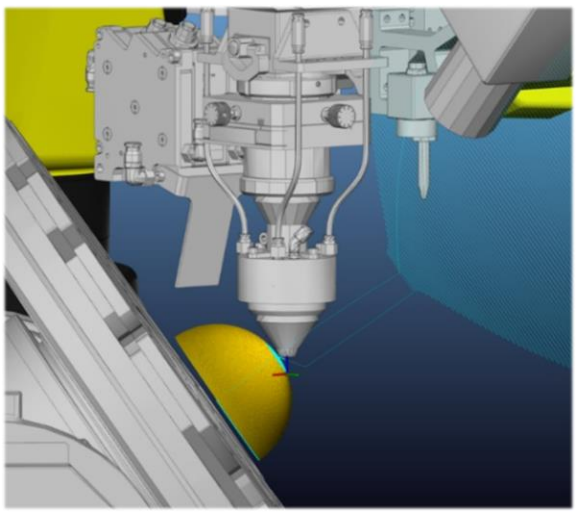

(a)

(b)

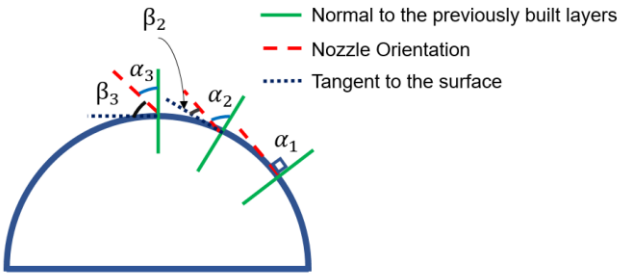


(c)

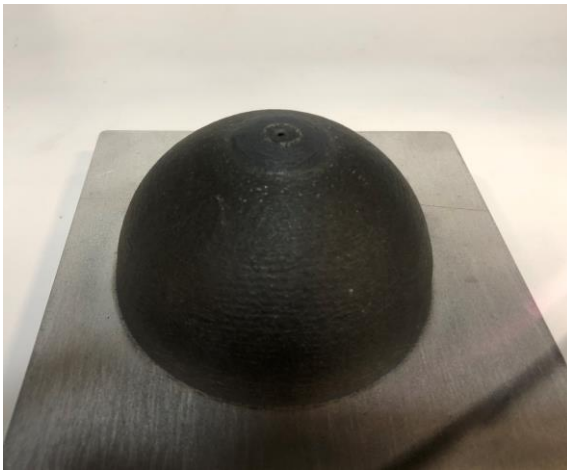

(d)

*Figure 4-3: LDED of dome structures (a) simulation (b) deposition process (c) schematic of varying overhang and tilt angle (d) final part*

Figure 4-4(a) shows the typical overlay of the CAD model cross section and the scanned data cross section. It is observed that the maximum deviation is at the top of the dome printed with maximum overhang angles of 32.5 degrees.

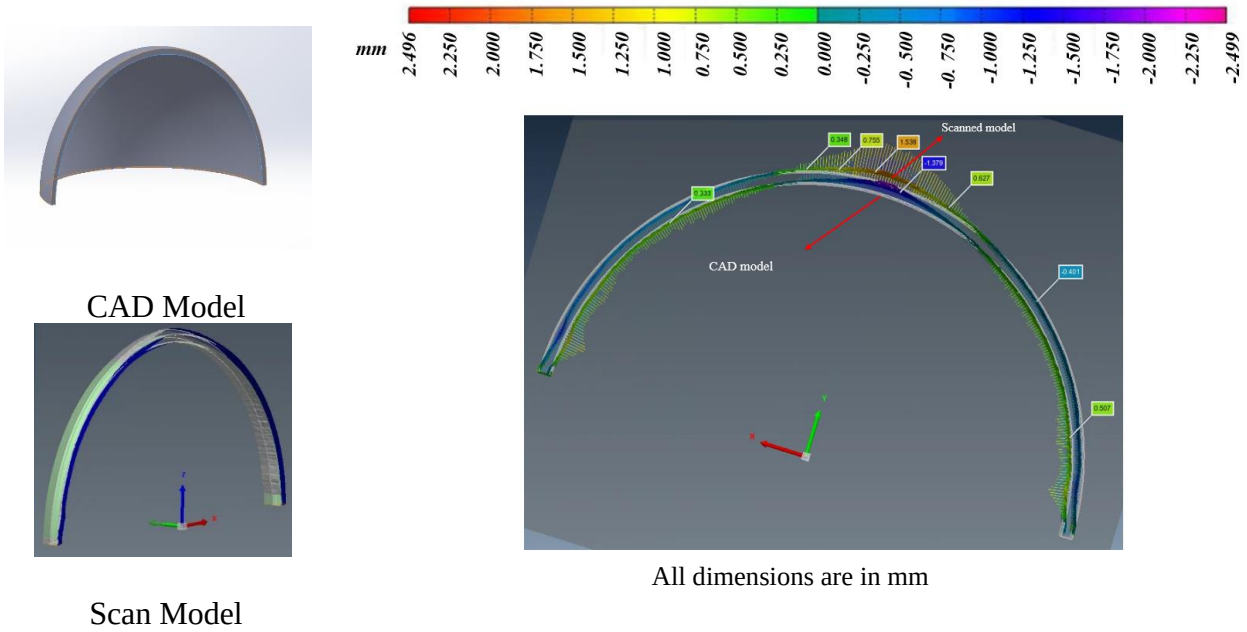


(a)

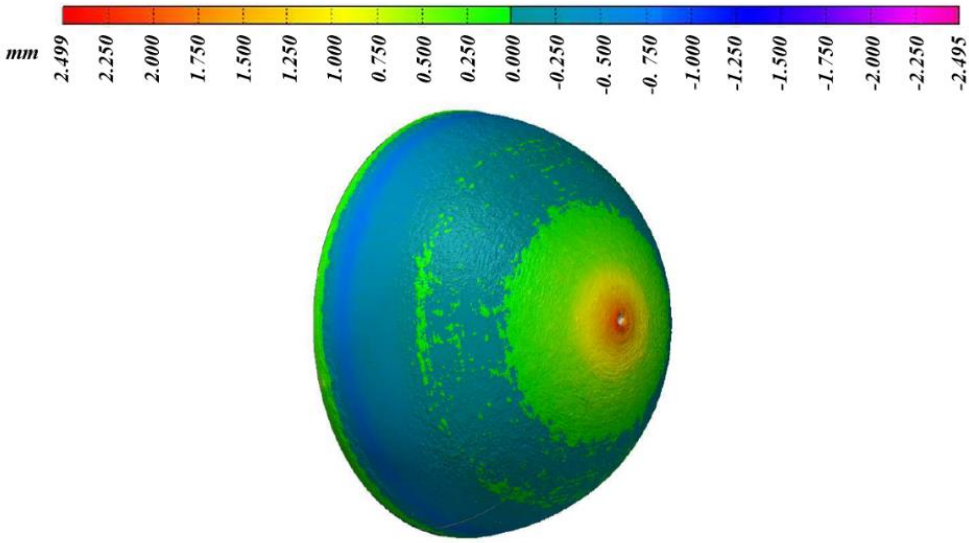


(b)

*Figure 4-4: CAD to part comparison of (a) typical cross-section (b) full dome structure*

Figure 4-5 presents the microscopic images obtained from different locations of the built dome structure. It is observed from Figure 4-5(a) that the deposition is defect-free without cracks and macro scale porosity. However, a deeper investigation of the structures shows that micro-porosity

is seen at different locations as shown in Figure 4-5(b). The micro-pores are mainly gas porosities, with the presence of a few lack of fusion pores at isolated locations.

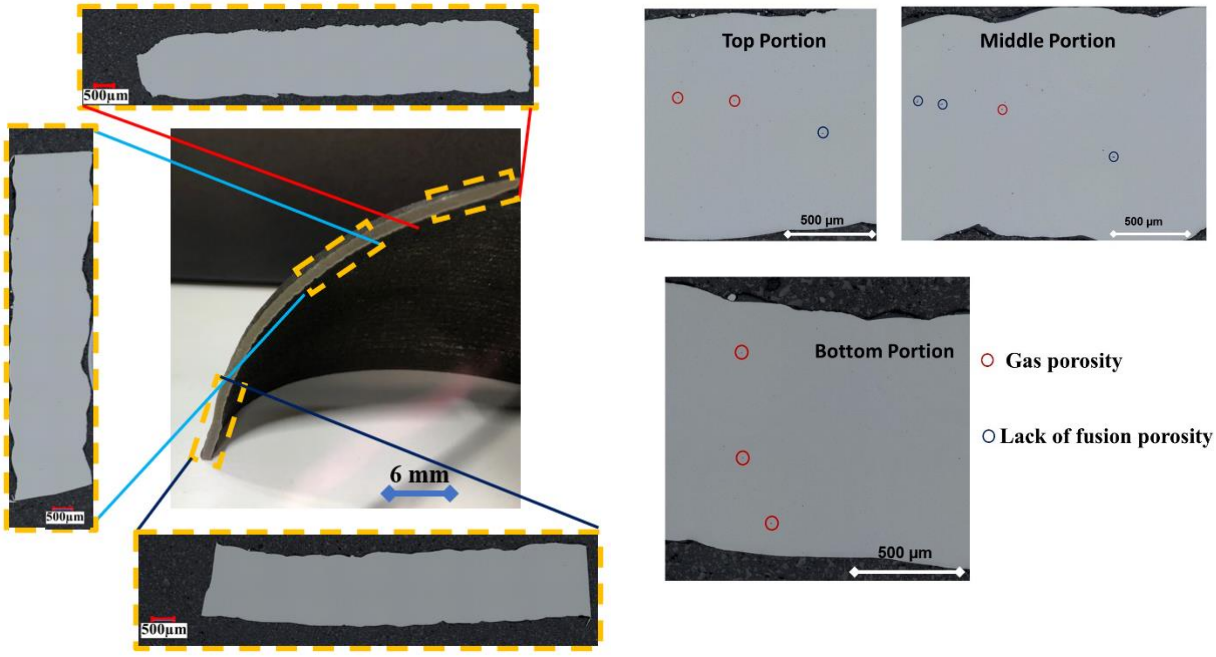


(a) (b)

*Figure 4-5: Cross-sectional images of the dome at different locations (a) lower magnification (b) higher magnification*

## 4.5 Summary

The present work proposes a novel methodology to manufacture the parts with variable overhanging angle. The methodology aids to avoid collision between the nozzle and the previously built layers while providing a proper melt pool stability, which allows the fabrication of the dome in a single step. Further, the methodology is verified by manufacturing the part and CAD to part comparison shows the maximum deviation of 2% with respect to the diameter of original CAD model data. The proposed methodology avoids partitioning of the component and the deployment of computationally expensive algorithms to manufacture overhang dome structures using LDED.

The subsequent chapter will discuss adaptive trajectory planning for geometries with overhang features; adaptive slicing and non-uniform layer height build-up for tubular components.

# 5 Adaptive trajectory planning for geometries with overhang features; Adaptive slicing and non-uniform layer height build-up for tubular components

## 5.1 Introduction

This chapter reports on an adaptive trajectory planning to build tubular components with variable overhang angles using a robotic LDED-PF based Additive Manufacturing process without utilizing support structures. The proposed technique uses a non-parallel slicing methodology to build complex components (e.g., bent pipes) and deploys adaptively varying scanning speed and tool orientation. The variation in scanning speed aids in having point-to-point variable layer height enabling non-parallel deposition while changing the tool orientation during deposition permits the manufacturing of support-free bent pipe parts. The bent pipes with 45° and 90° bents were built using an in-house developed LDED-PF system and the built parts are characterized for geometry, density, microstructure, and microhardness. The geometrical analysis indicates the deviation in the range of +0.5 mm to -0.5 mm, with minimal roundness deviation at different sections. The density analysis of the segments extracted from the bent pipe reveals a density >98%, with the presence of a few lack of fusion pores and gas pores at isolated locations. The microstructure and microhardness studies show that regions built with higher scanning speeds have a finer grain structure and higher average hardness. The study paves a path to build defect-free and dimensionally stable complex-shaped components with varying overhang angles using LDED-PF.

## 5.2 Literature Review

Although LDED-PF permits the fabrication of complex-shaped metallic components with overhangs, undercuts, etc., the fabrication of these structures requires process-specific planning and strategy development. In LDED-PF, the fabrication of overhang structures is challenging as

there is no powder underneath the built layers to support the fabrication of overhang structures. [86]. Generally, overhang structures are built with the help of sacrificial support structures that are built using low energy density/ infill percentage for reduced strength, facilitating easy removal [87]. After the processing stage in MAM, these support structures are removed in the post-processing stage. The deployment of support structures results in material wastage and can hamper the sustainable nature of the MAM process. In addition, support removal is time-consuming, unproductive, and requires human involvement in many steps[88]. This led to the development of five-axis LDED-PF systems that can be deployed for building complex-shaped components with variable overhang angles. These systems permit multi-directional deposition that evades the necessity of the support structures by appropriately positioning the part during the deposition [89].

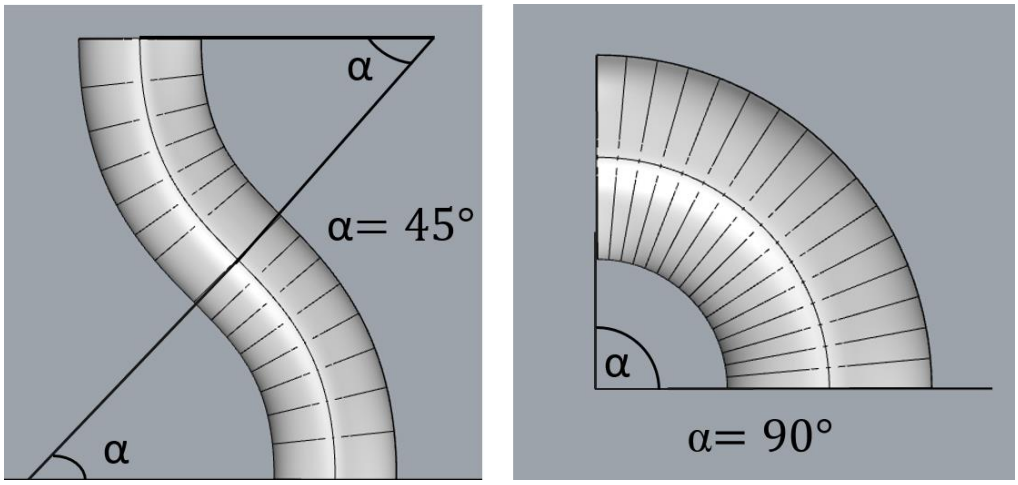


(a) (b)

*Figure 5-1 : Example of bent pipes with inclined angles of (a) two bends of 45°(b) 90°*

In addition, the approaches for building complex-shaped components also depend on the slicing approach. In the traditional parallel slicing, the overhang angles increase until there is no support for the consecutive layers [90]. Maximum overhang angles in LDED-PF depend on process setup and process parameters [77]. Thus, several researchers addressed this issue using non-parallel slicing to keep the tool orientation tangent to the surface curvature for avoiding the overhang

angles [91]. The non-parallel slicing approach uses the tilt angle of the tool and the base to compensate for the overhang angle [92]. The approach becomes more critical when the parts have variable overhang angles. One of the examples of the parts having variable overhang angles along the build direction is the bent pipe. Special geometrical and process-related considerations are required to build bent pipes using LDED-PF [93]. Figure 5-1(a) and Figure 5-1(b) show examples of a bent pipe with inclination angles of 45° and 90°, respectively.

The literature indicates that efforts are being made by researchers to develop novel slicing algorithms to potentially build bent pipe parts. Murtezaoglu et al. [94] used the 3+2 partitioning technique to build the sections of the pipe using parallel slicing and re-orient the part to avoid the overhang angles in the next group of layers. Xiao et al.[95] developed an automated technique to reorient the part during the build using a 5-axis machine. The reorientation allows to part to be built using the traditional uniform slicing approach but without the support. They used volume decomposition to divide the part into printable sub-volumes that each can be built with planar layers without the support structure. Ruan et al. [96] developed an adaptive slicing algorithm to deposit non-uniform layer thickness in a different orientation to avoid the overhang angle. Panchagnula et al. [97] developed an adaptive height slicing technique to deposit variable height deposition using the regression model developed to predict the bead dimensions. Due to the unevenness in the flatness of the top surface, an additional subtractive operation was required. Xiangping et al.[81] developed an adaptive slicing algorithm for the segmentation of parts into sub-volumes which can be built using the traditional uniform layer height. A volume-based decomposition algorithm based on overhang identification between the adjacent segments was used to manufacture the decomposed parts separately. The above-mentioned volume decomposition strategies remain incapable of manufacturing large-scale parts with desired

dimensional accuracy. The volume decomposition divides the part into wedge-like segments as shown in Figure 5-2(a). A big disadvantage of the decomposition method is the creation of several open toolpaths at the boundaries of the segments, which leads to too many linking motions and staircase effect [98] at the boundaries of the segments as shown in Figure 5-2(b). Therefore, the top surface of each wedge-shaped segment will be very uneven. The bottom of the next wedge must be placed on top of this uneven surface, which will lead to obvious surface irregularities at the boundaries between the wedges. A case study by Kalami et al. [79] for building a surface dome using the partitioning technique shows surface irregularities at the boundaries of the wedges.

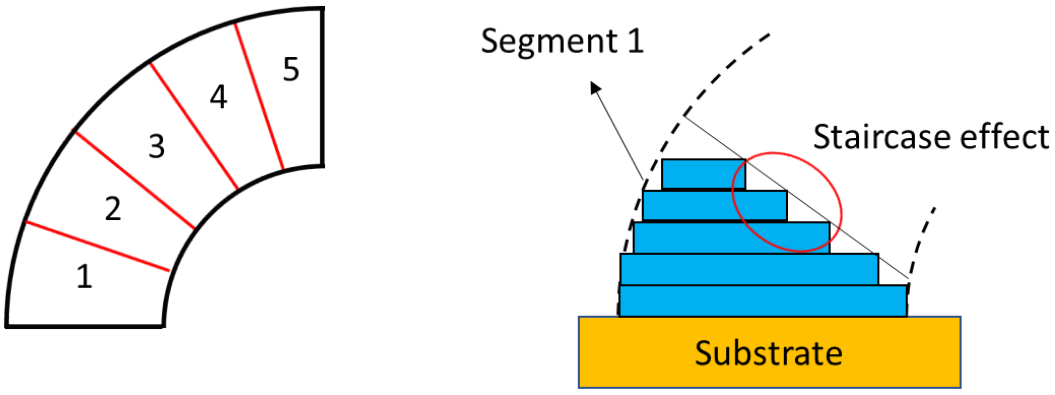


(a) (b)

*Figure 5-2: (a) Volume decomposition of a bend-pipe geometry to wedge-like sub-volumes, (b) Uneven top surface of a wedge-like segment due to toolpath linking motions*

Thus, it can be concluded from the literature that the decomposition methods based on the volume and area difference of planar slices were mostly used for the deposition of geometries with large overhang angles (e.g., Bent pipes, pipes with branches). As these techniques lead to non-smooth toolpath and irregular geometry, there is a need to develop a generic methodology that can be used to build cylindrical components with varying overhang angles that can pave way for building tubular geometries [94-95].

The present work reports a novel slicing technique based on adaptive tool orientation and point-to-point variable layer height using a centroid axis to build tubular components with variable overhangs. A perpendicular plane to the centroid axis is created at each layer for toolpath calculation resulting in smooth toolpath generation without discontinuity. This technique led to the successful manufacturing of two large-scale bent pipes in the first trial without extensive process planning or trial experiments. An extensive ex-situ quality assurance procedure is also performed to evaluate the dimensional accuracy, density, microstructure, and microhardness of the built components.

## 5.3 Adaptive Trajectory Planning Algorithm

LDED permits the supportless fabrication of complex-shaped parts with overhang features. The additional axis of rotation for the base plate aids to position the part in a way to avoid support structures. Figure 5-3 shows the fabrication of the bent pipe using the rotary table, where $A_1$ is the first axis of rotation of the positioner. As the deposition moves from the bottom to the top layer, $A_1$ is incremented in each layer and it is kept constant for through the entire toolpath for the layer so that the previously built layers will act as a support structure for the consecutive layers using the rotary transformation of the piece. Thus, the bent pipe is built by laying self-supporting layers one over the other using positioner tilting. The developed algorithm has two main components, adaptive slicing and non-uniform layer height deposition which are elaborated in the subsequent sections.

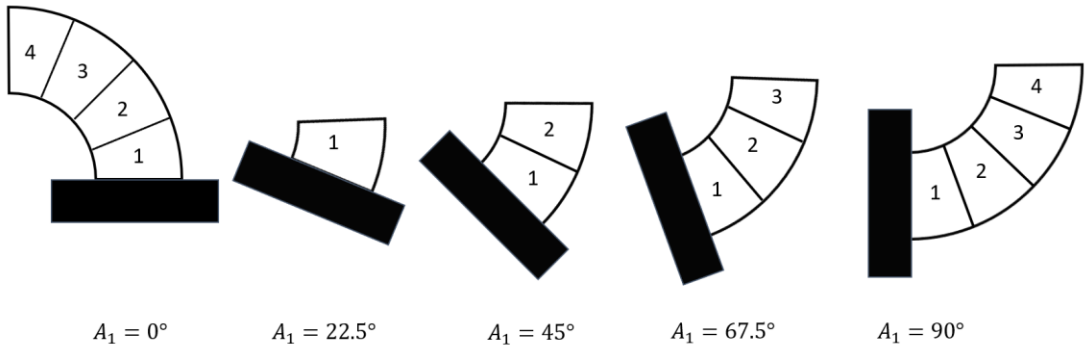


*Figure 5-3: Building of a bent pipe with overhang features using multi-axis LDED*

### 5.3.1 Adaptive Slicing

Figure 5-4 presents the flowchart of the adaptive slicing algorithm. The algorithm starts by importing the input geometry, i.e. the machining surface (the surface on which the deposition is performed), containment boundary mesh (the mesh that contains all the toolpath geometry), and the centroid spine (which the machining surface is rotated about in different layers) as shown in Figure 5-5(a) (step 1). The distance between subsequent layers at the intersection points of the centroid spine and the machining surface *($l_{centroid}$)* and maximum allowable tilt angle between two consecutive layers ($\alpha_{max}$) are provided as the input to the algorithm. $\beta_j$ is the tangent direction along the centroid spine at the $l_{centroid}$. Step 2 begins with the determination of $\beta_j$, which is explained in detail later. The machining surface is rotated (step 2) and the cross-section of the rotated machining surface with the boundary mesh generated contour are obtained as shown in Figure 5-5(b) and Figure 5-5(c) (step 3). Step 2 and Step 3 are repeated until all the layers are processed. Once the contours are generated, they will be linked together to generate the toolpath (step 4). Once the toolpath is generated, the adaptive scanning algorithm adjusts the point-to-point scanning speed as shown in Figure 5-5(d).

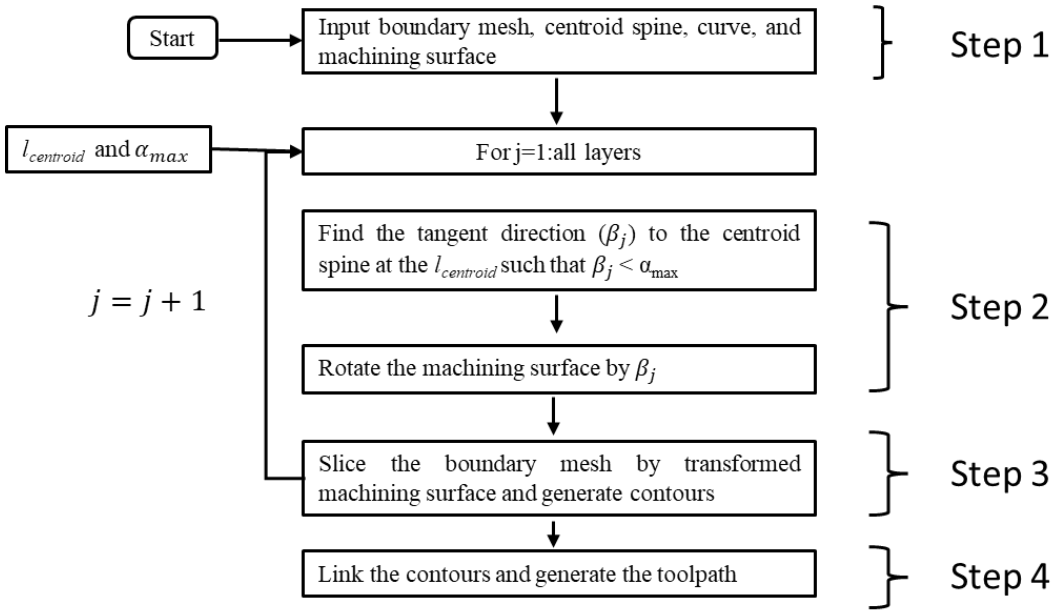


*Figure 5-4: Flowchart of the slicing algorithm*

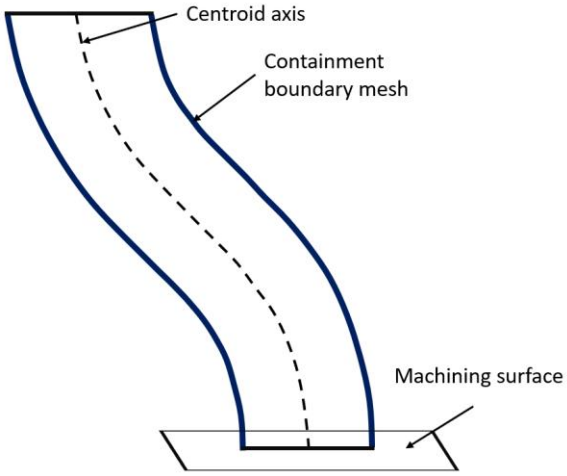


(a)

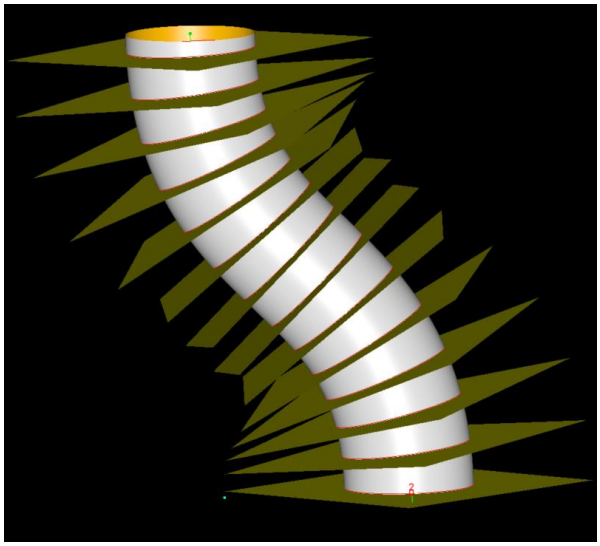

(b)

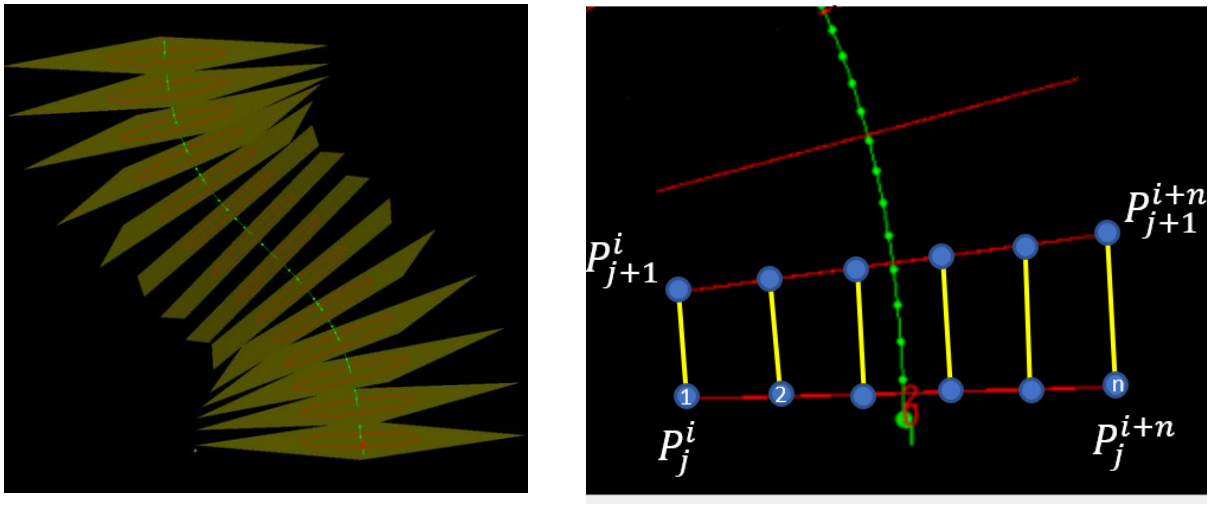


(c) (d)

*Figure 5-5:* Adaptive *slicing for the bent pipe using variable slice height*

The algorithm for estimation of the $\beta_j$ (step 2 in Figure 5-4) and transformation of the machining surface to a new position and orientation is shown in Figure 5-6 . The initial normal vector of the machining surface is denoted as $\vec{n}_j$ and it is equal to the unit vector along the z-axis and $C_j$ is the intersection of the centroid spine and the machining surface as shown in Figure 5-6(a). $C_{j+1}$ is the result of moving $C_j$ at a distance of $l_{centroid}$ along the centroid spine as shown in Figure 5-6 (b). The updated normal vector $\vec{n}_{j+1}$is defined by the tangent to the centroid spine at the $l_{centroid}$ and $\beta_j$ is the angle between $\vec{n}_j$ and $\vec{n}_{j+1}$ as shown in Figure 5-6(b). $\beta_j$ is then calculated using Equation 5-1. If $\beta_j$ is larger than $\alpha_{max}$ , $\vec{n}_{j+1}$will be iteratively computed until $\beta_j$ is less than $\alpha_{max}$ while $\vec{n}_{j+1}$is minimally different from the $\vec{n}_j$. Once $\beta_j$ is found, the machining surface is rotated (by $\beta_j$ ) to keep it perpendicular to $\vec{n}_{j+1}$as shown in Figure 5-6(c).

$$\beta_j = cos^{-1}(\frac{\vec{n}_{j+1}}{\vec{n}_j}) \qquad 5\text{-}1$$

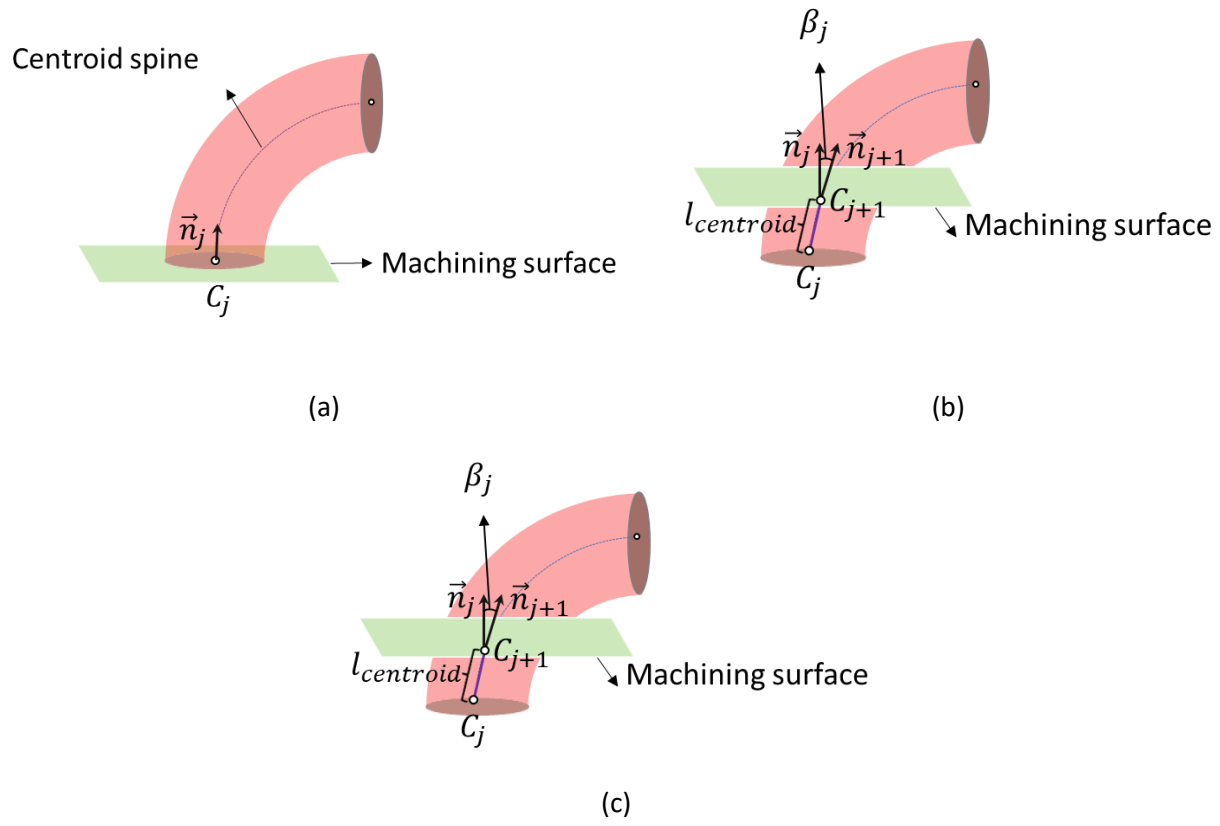


*Figure 5-6: Algorithm for estimation of β and transformation of machining surface*

The flowchart for robotic toolpath generation is shown in Figure 5-7. The scanning speed at each point is adjusted based on Equation 5-2, where, $v_o$ is the average scanning speed and $P_j^i$ and $P_{j+1}^i$ are the two points from layer j and j+1, respectively. $dist(P_j^i, P_{j+1}^i)$ is the layer height between $P_j^i$ *and* $P_{j+1}^i$ of a particular slice, and $C_b$ is estimated experimentally where it depends on $l_{min}$, $l_{max}$ and α. A series of single-track experiments with different scanning speeds were performed to estimate $C_b$. $C_b$ is set to 0.9 for the 90° bent pipe and 1 for the 45° bend pipe based on the experimental results.

$$v_p = C_b v_o \frac{l}{dist(P_j^i, P_{j+1}^i)} \qquad 5\text{-}2$$

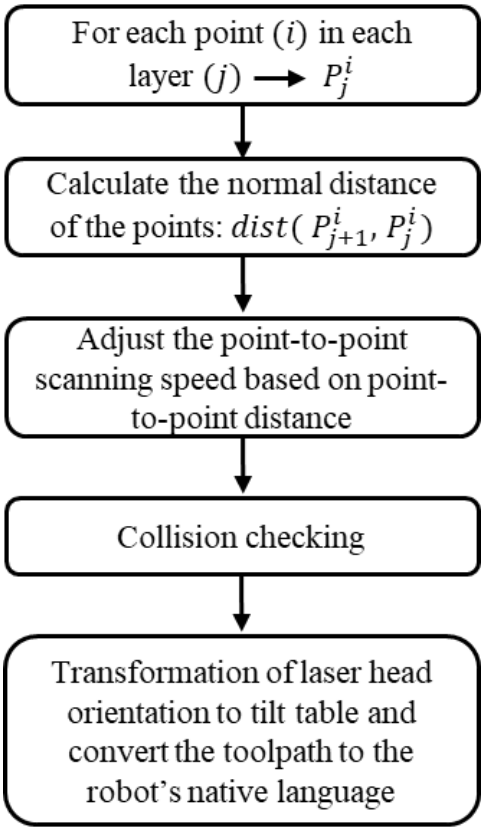


*Figure 5-7: Flowchart for adaptive scanning speed adjustment*

Once the scanning speed is adjusted, the collision checking is performed using ModuleWorks (MW) inverse kinematics for industrial robots. The collision is checked between the robot end-effector, base plate, deposited geometry, and robot axis. If any collision is detected, the trajectory is regenerated. The toolpath contains the tool vector information, as shown in Figure 5-8(a). Since deposition in this configuration is not desirable due to nozzle inefficiency in non-gravity direction, the positioner can be used to position the workpiece in a configuration in which the nozzle can deposit perpendicular to the slicing plane as shown in Figure 5-8(b). This can be achieved by tilting the positioner. Considering the orientation, the tool orientation vector ($N_l$) can be transformed from $l$ coordinate system to $l'$ coordinates system using Equation 5-3 [101]:

$$R_{T'l'} = R_{T'E_1'} \times R_{E_1'E_2'} \times R_{E_2'B'} \times R_{B'l'} \quad 5\text{-}3$$

where, $R_{T'l'}$ is the rotation matrix between the positioner TCP and the updated laser head coordinate system ($l'$), $R_{T'E_1'}$ is the rotation matrix between the posterior TCP and the reference obtained by rotation of the tilt axis, $R_{E_1'E_2'}$ is the rotation matrix between the tilt ($E_1'$) and rotation ($E_2'$) axis, $R_{E_2'B'}$ is rotation matrix between the reference frame of $E_2'$ to the base userframe and $R_{B'l'}$ is the rotation matrix between the base user frame and laser head TCP. Since the rotation of the laser head with respect to the base userframe remain unchanged, the tilt axis is only needed to position the part to take advantage of gravity. Equation 5-3 can be re-written as Equation 5-4:

$$R_{T'l'} = R_{T'E_1'} \times R_{Z_T}(E_2) \times R_{E_2B} \times R_{BL} \quad 5\text{-}4$$

where,

$$R_{T'E_1'} = \begin{bmatrix} 1 & 0 & 0 \\ 0 & \cos\emptyset & -\sin\emptyset \\ 0 & \sin\emptyset & \cos\emptyset \end{bmatrix}$$

and Ø is the tilt angle of the positioner in $E_1$ direction.

Once the collision-free toolpath is available, it is converted to the robot's native language and sent to the robot controller to start the deposition.

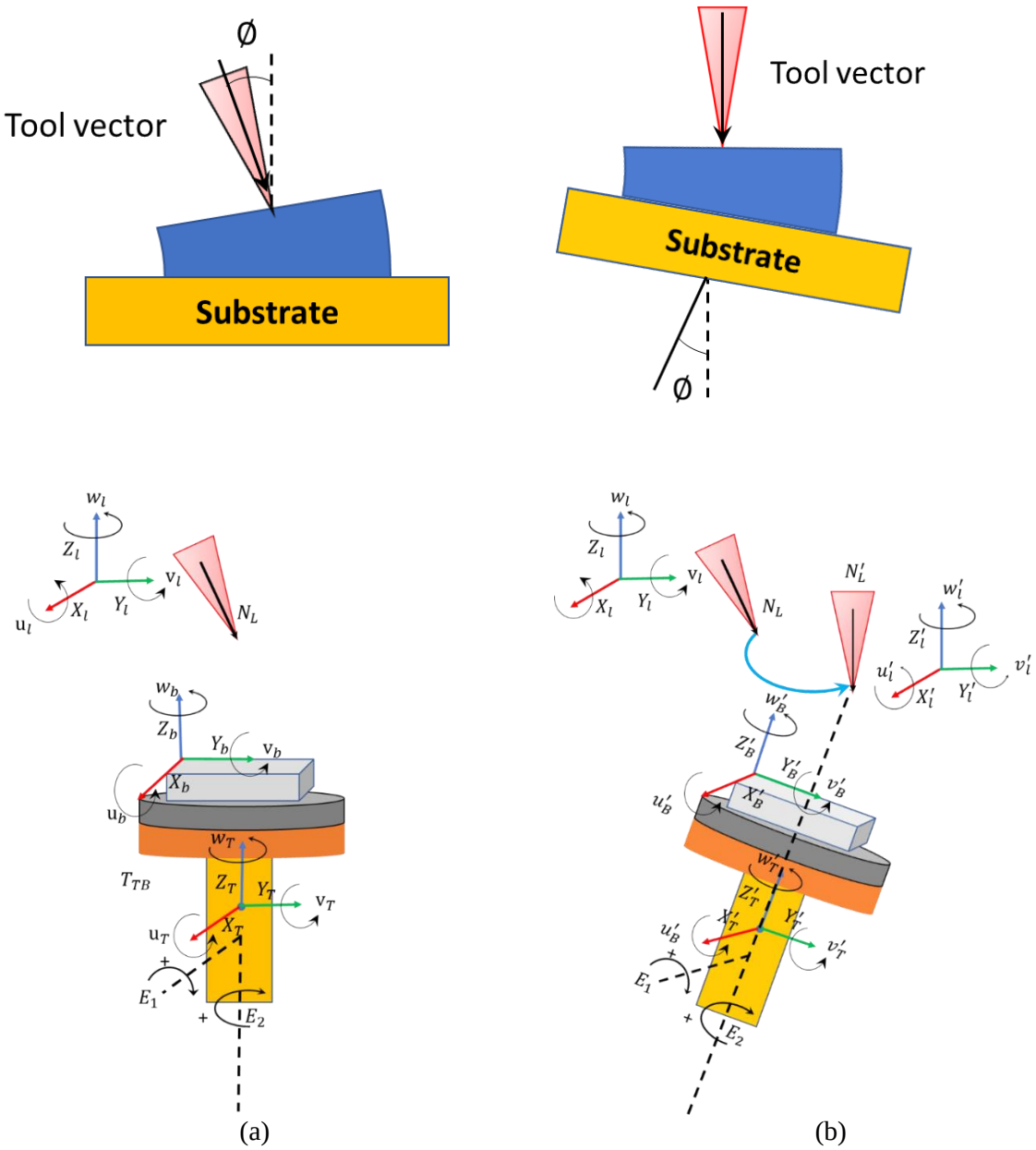


*Figure 5-8: Transformation of the laser head orientation corresponding to the table tilt*

### 5.3.2 Deposition of non-uniform layer height

The developed algorithm was implemented on two bent pipe geometries having a single bend of 90° and a double bend of 45°. The radius of the spine curve is 50 mm, and the length of the spine curve is calculated using Equation *5-5*, where $r_s$ and $\theta_L$ are shown in Figure 5-9(b) and α is the bend angle of the pipe. An average layer height of 0.5 mm is considered to estimate the number of

layers (N) using Equation *5-6*. Further, Equation *5-7* is used to estimate the bent angle between each layer ($\boldsymbol{\alpha_L}$). A bent angle of 90° is considered for the single bent pipe, and 45° is considered for the double bent pipe. Figure 5-9(a) shows a typical single layer in adaptive slicing, which is used to estimate $\boldsymbol{l_{min}}$ and $\boldsymbol{l_{max}}$. For the 90° bent pipe, the calculated values of $\boldsymbol{l_{min}}$ and $\boldsymbol{l_{max}}$ are 0.25 mm and 0.75 mm, respectively. As mentioned in section 2.2, the variation in layer height is achieved by varying the scanning speed. The single-track analysis indicates that the scanning speed required to deposit layer heights of 0.25 mm and 0.75 mm is 18 mm/sec and 6.4 mm/sec, respectively. Table *5-1* presents the corresponding layer height and scanning speed at each segment. Similarly, the calculated $\boldsymbol{\alpha_L}$ for the 45° bent pipe is 0.286°. Considering an average layer height of 0.5 mm, the calculated values of $\boldsymbol{l_{min}}$ and $\boldsymbol{l_{max}}$ are 0.4 mm and 0.625 mm, respectively, for the 45° bent pipe.

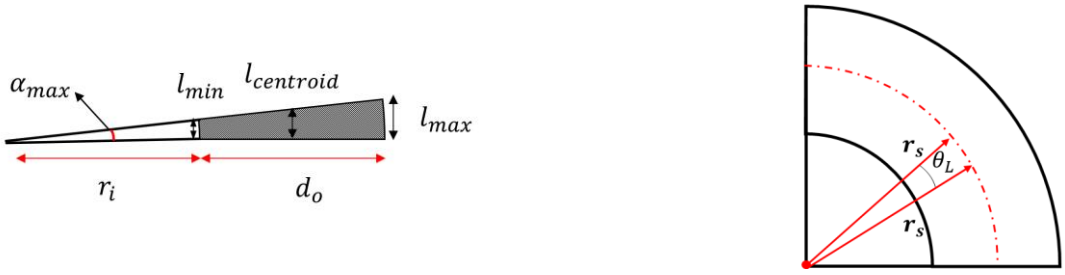


(a) (b)

*Figure 5-9: (a) Single layer in adaptive slicing, (b) spine length based on curvature angle*

Figure 5-10 (a) - (d) present the schematic showing the segmentation of each layer into partitions based on distance from the previous layer. Each layer in the toolpath is decomposed to $\boldsymbol{n(20)}$ segments with constant angular increments. In each segment, the Euclidean distance to the previous layer is calculated, and the scanning speed is adjusted according to Equation 5-2. The corresponding layer height and scanning speed for each segment for a typical layer are presented. In Figure 5-11. The relationship between scanning speed and distance to the previous layer for the

45° and 90° bent pipe is provided in Table *5-1*. Figure 5-12 presents the variation of the scanning speed along the build direction. The outer portion of the bent pipes was built with a higher scanning speed, and the inner portion of the bent pipes was built with a lower scanning speed facilitating non-uniform height deposition. It can be noted that in the transition region from the first bend to the second bend, multiple layers were printed without the scanning speed adjustment since the point-to-point distance to the previous layer was constant within the layer, as shown in Figure 5-12(b). It may be noted that the length of the spine belonging to the transition region is not considered for the estimation of the $\boldsymbol{\alpha_L}$.

$$l_{spine} = \int_0^{\alpha} r_s \theta_L \qquad 5\text{-}5$$

$$N = \frac{l_{spine}}{l} \qquad 5\text{-}6$$

$$\alpha_L = \frac{N}{\alpha} \qquad 5\text{-}7$$

Table 5-1:Layer height and scanning speed at each segment of the path

| Segment | Layer height(mm)- bend pipe with 90° bend | Scanning Speed (mm/sec)- bend pipe with 90° degrees bend | Layer height(mm)- bend pipe with double 45° bend | Scanning Speed (mm/sec)- bend pipe with double 45° bend |
|---|---|---|---|---|
| $h(i,1)= h(i,20)$ | 0.25 | 18 | 0.4 | 12.5 |
| $h(i,2)= h(i,19)$ | 0.305 | 14.75 | 0.425 | 11.76 |
| $h(i,3)= h(i,18)$ | 0.36 | 12.5 | 0.45 | 11.11 |
| $h(i,4)= h(i,17)$ | 0.415 | 10.85 | 0.475 | 10.52 |
| $h(i,5)= h(i,16)$ | 0.47 | 9.57 | 0.5 | 10 |
| $h(i,6)= h(i,15)$ | 0.525 | 8.5 | 0.525 | 9.52 |

| | | | | |
|---|---|---|---|---|
| $h(i,7)= h(i,14)$ | 0.58 | 7.75 | 0.55 | 9 |
| $h(i,8)= h(i,13)$ | 0.63 | 7.14 | 0.575 | 8.69 |
| $h(i,9)= h(i,12)$ | 0.695 | 6.5 | 0.6 | 8.33 |
| $h(i,10)= h(i,11)$ | 0.75 | 6.4 | 0.625 | 8 |

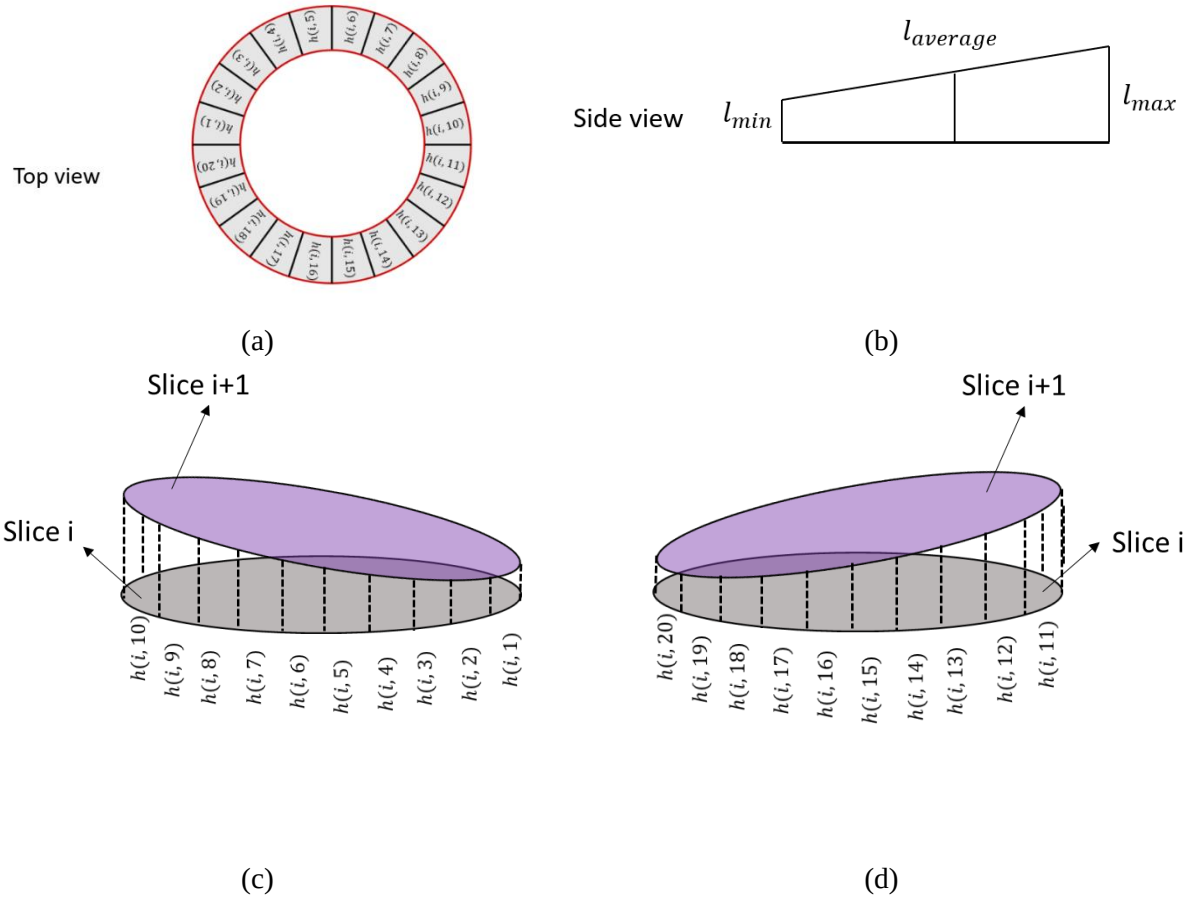


*Figure 5-10: Segmentation of each slice to partitions (a) 2D view (top), (b) 2D view (side) (c) 3D view(back),(d) 3D view(front)*

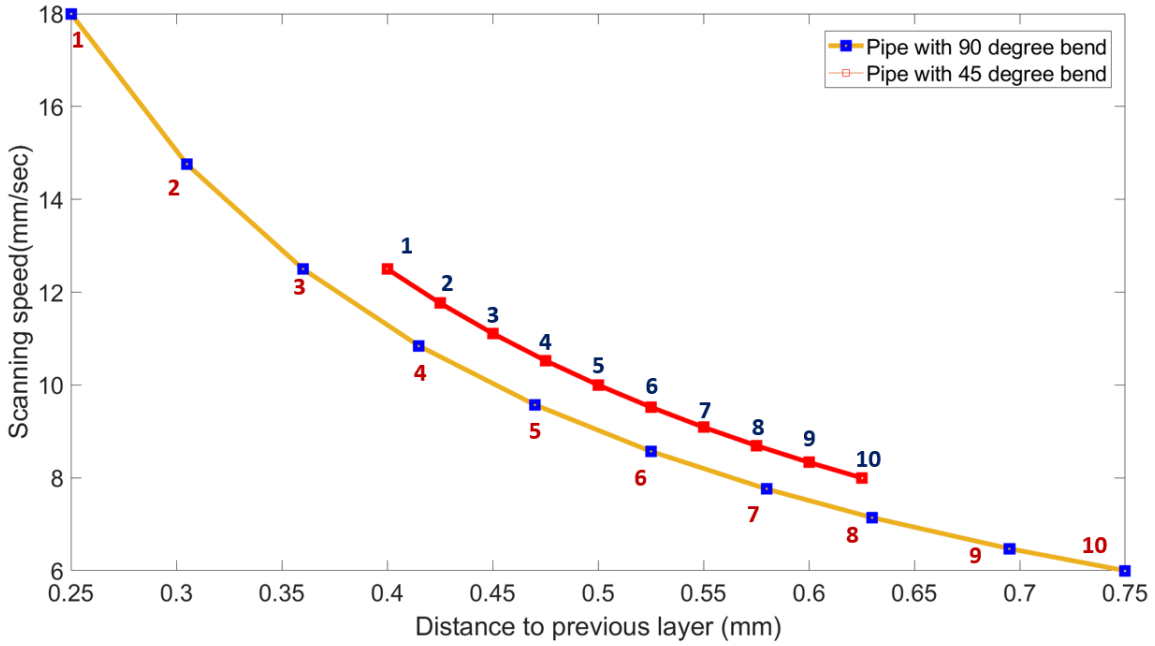


*Figure 5-11: Adaptive scanning speed based on the normal distance to the previous layer*

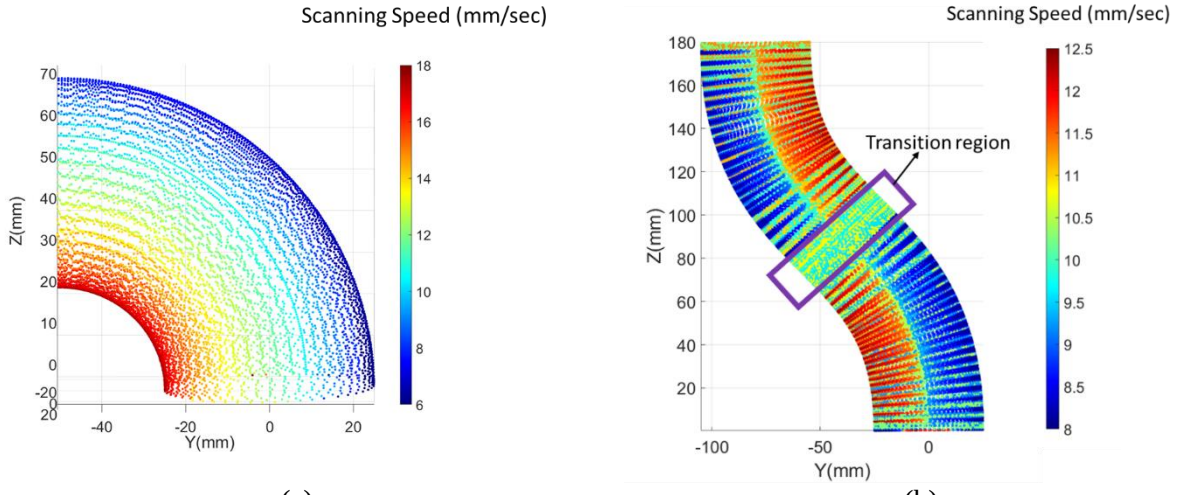


(a) (b)

*Figure 5-12: Variation of scanning speed in toolpath for (a) 90° bent pipe, (b) 45 ° double bent-pipe*

Figure 5-13 presents the simulation of the toolpath at various stages. It shows the change in the positioner orientation during the deposition to build the overhang structures without support structures. During the deposition using positioner tilt, $\emptyset$ is the tilt angle of the $E_1$, and it is used for the positioning of each layer, and it is kept constant for the entire layer of the deposition. The toolpath simulation video is provided as a supplementary file.

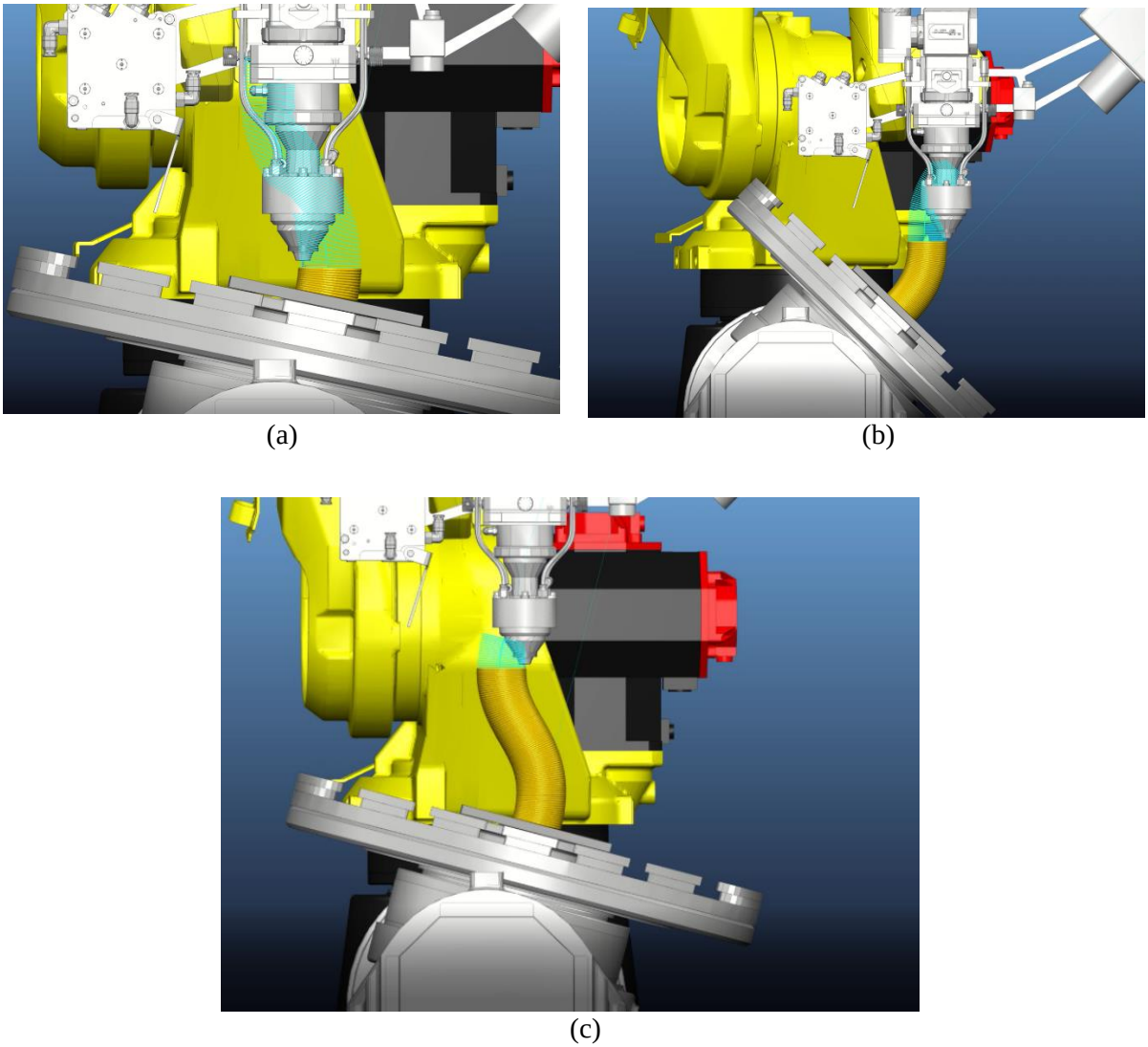

(a) (b)

(c)

*Figure 5-13: Toolpath simulation for building 45° bent pipe*

## 5.4 Results and Discussion

Figure 5-14(a) and Figure 5-14(b) present the photographic view of the 90° and 45° bent pipes respectively. The bent pipe structures are subjected to detailed geometrical, density, microstructural, and mechanical characterizations towards the qualification of the built parts to enter the additive manufacturing market. This section reports on comprehensive geometrical and material characterizations of the bent pipes.

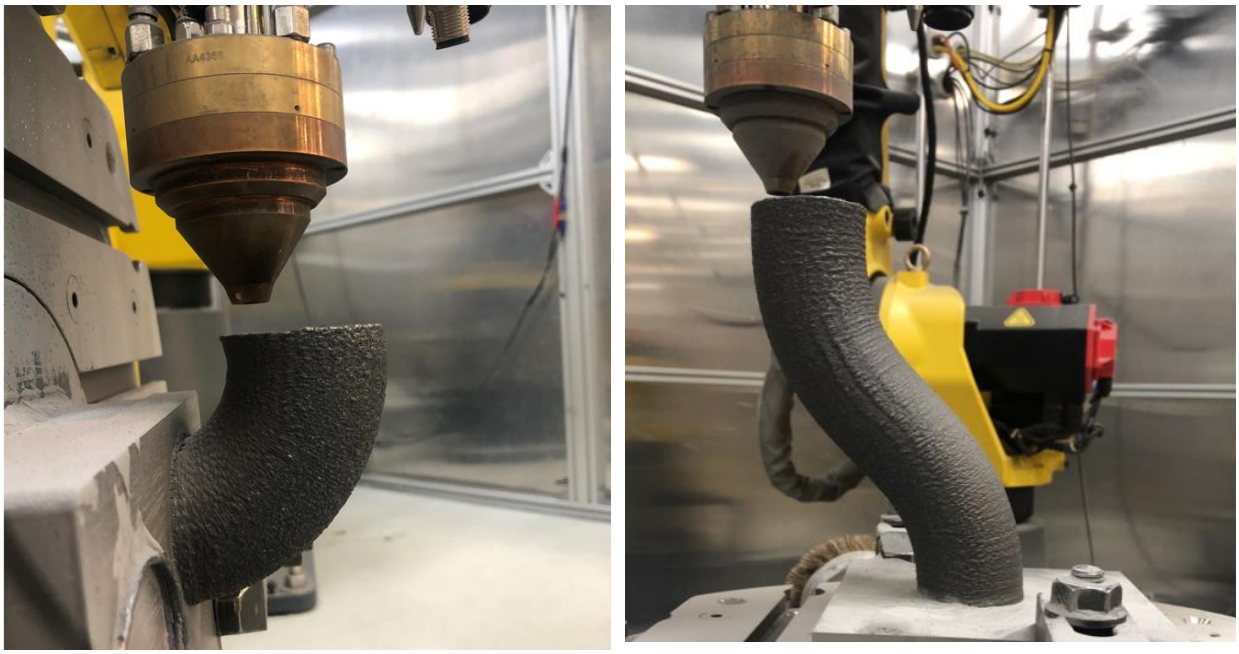

(a) (b)

*Figure 5-14: Photographic view of (a) 90° bent pipe, (b) double 45° bent pipe*

### 5.4.1 Geometrical Analysis

CAD-to-part comparisons of the built bent pipe structures are performed. Figure 5-15(a) presents the dimensional deviation between the CAD and built component of the double 45° bent pipe. The average deviation ranges from +0.5 mm to -0.5 mm. This indicates a good match between the built geometry and the input CAD model. The maximum deviation at the top surface can be due to the

surface waviness of the top layers. In addition, sections are taken at two different locations along the height of the bent pipe as shown in Figure 5-15(b). The sections are taken from the bottom and top regions to understand the profile of the bent pipe in the vertical region of the pipe. The least squares fitting method is used to fit circles to the extracted cross-section [102] as shown in Figure 5-15(c). The root-mean-square roundness deviation ($\Delta R_{rms}$) [100-101] is used to find the deviation of the points from the nominal circle as shown in Equation 5-8, where $R_l$ is the Euclidean distance of each point belonging to the extracted point cloud to the center of the least square circle and $R_{ls}$ is the radius of the least square circle, and $\Delta R_l$ is defined using Equation 5-9.

$$\Delta \mathrm{R_{rms}} = \sqrt{\frac{1}{2\pi}\int_0^{2\pi} \Delta R_l^2 d\theta} \qquad 5\text{-}8$$

$$\Delta R_l = \left| R_p - R_{ls} \right| \qquad 5\text{-}9$$

The radius of the fitted least square circles, Root Square Mean Error (RSME) of the fitting and roundness deviation from the reference least square circles for the 45° pipe are shown in Table 5-2 . The extracted point cloud is fitted to a circular profile using the least square circle fitting method, and the radius of the profiles is 25.47 mm, and 25.39 mm at the bottom, and top sections, respectively. $\Delta R_{rms}$ values of 0.14 mm and 0.05 mm in section 1 and section 2, respectively show the dimensional stability of the built bent pipes.

Table 5-2:Roundness deviation from the reference least square circles for 45° bent pipe

| Section | Radius of the fitted least square circles (mm) | RSME (mm) | $\Delta R_{rms}(mm)$ |
|---|---|---|---|
| 1 | 25.47 | 0.293 | 0.14 |
| 2 | 25.39 | 0.172 | 0.05 |

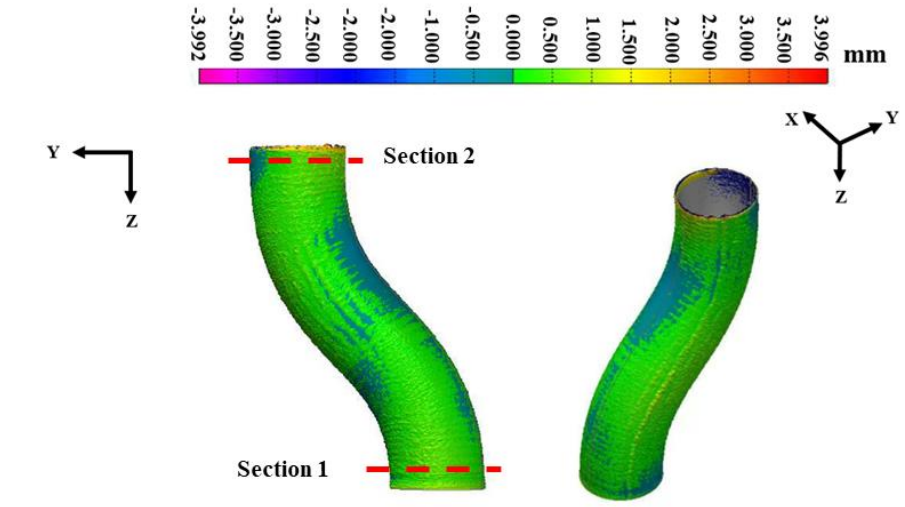


(a)

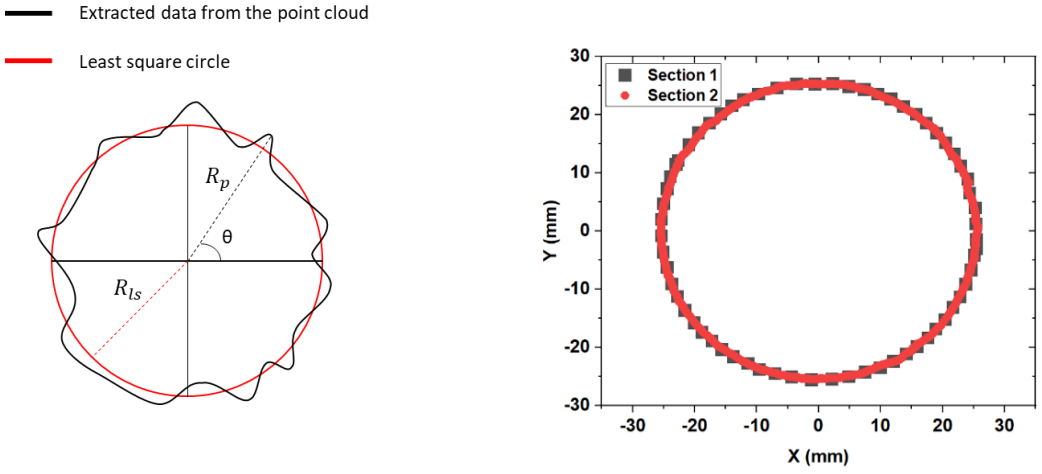


(b) (c)

*Figure 5-15: Geometrical analysis of 45° bent pipe (a) CAD to part comparison, (b) Fitted least square circle (c)cross-section at top and bottom region*

Similarly, the CAD to the part comparison of the 90° bent pipe shows that the average deviation ranges from +0.5 mm to -0.5 mm as seen in Figure 5-16(a). It can be seen in both cases that the positive shift in the deviation is more significant, which can be primarily due to the outward flow of the melt pool during the deposition process. However, a deviation of 1-2 mm is seen at localized points. The higher deviation is mainly seen at the top layers of the outer curve and regions of higher curvature radius, which can be due to higher melt-pool flow and dynamics in these regions.

Sections are taken from the top, and bottom regions to analyze the cross-section along the build direction, as shown in Figure 5-16(b). The radius of the fitted least square circles, RSME of the fitting and roundness deviation from the reference least square circles for the 90° pipe are shown in Table 5-3. The generated point cloud is fitted to a circular profile using the least square circle fitting method, and the radius of the circle is 25.15 mm, and 25.45 mm at the bottom, and top regions, respectively. $\Delta R_{rms}$ values of 0.07 mm and 0.09 mm at section 1 and section 2, respectively indicate the dimensional stability of the built bent pipes.

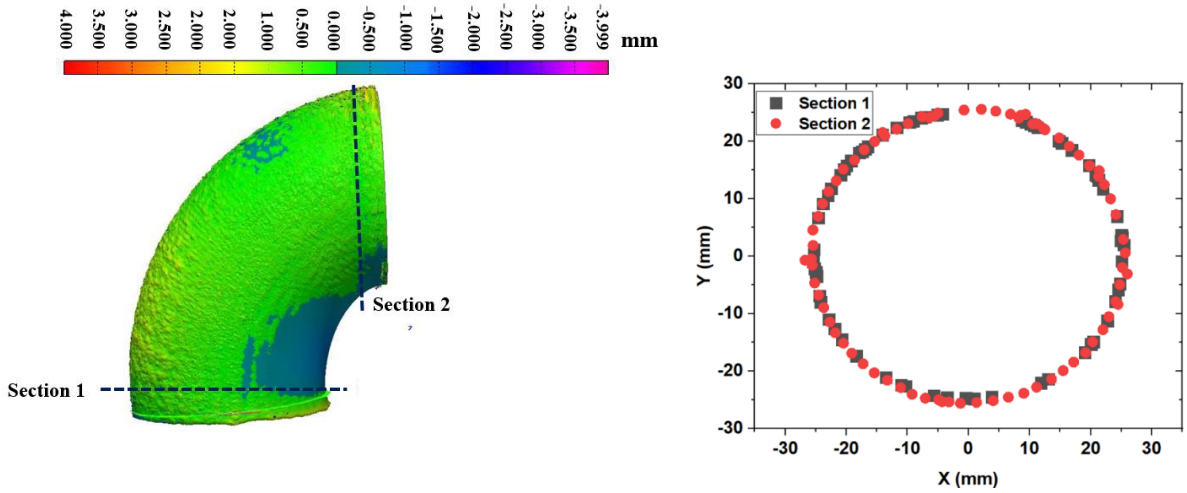


(a) (b)

*Figure 5-16: Geometrical analysis of 90° bent pipe (a) CAD to part comparison (b)cross-section at top and bottom region*

*Table 5-3:Roundness deviation from the reference least square circles for 90° bent pipe*

| Section | Radius of the fitted least square circle (mm) | RSME (Least Square fitting Error) (mm) | $\Delta R_{rms}(mm)$ |
|---|---|---|---|
| 1 | 25.46 | 0.251 | 0.07 |
| 2 | 25.48 | 0.266 | 0.09 |

The wall thickness of the printed parts is extracted from the acquired point clouds, as shown in Figure 5-17(a). Once the cross-section of the point cloud is extracted, the statistical outlier technique is used to denoising the point cloud data and the result are shown in Figure 5-17(b). The width of each section is then calculated using the Euclidean distance between the curves. The average wall thickness of 2.2 ± 0.2 mm and 1.8 ± 0.3 mm is calculated for the outer curve and inner curve, respectively. The slightly higher wall thickness for the outer circle can be due to the lower scanning speed used for depositing the outer region of the pipe. It can be noted that the variation in the wall thickness between the outer curve and inner curve is not significant, indicating good dimensional stability.

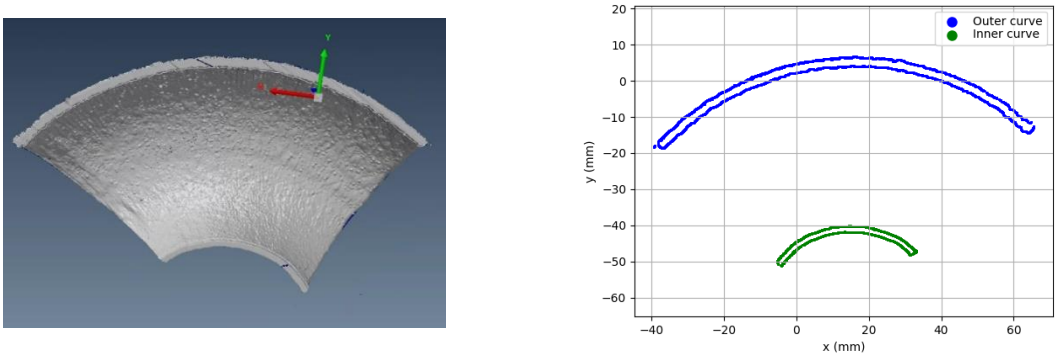


(a) (b)

*Figure 5-17: Wall thickness of the bent pipe (a) scanned model (b) profile*

### 5.4.2 Density analysis

Figure 5-18 presents the section of the bent pipe indicating the location of extracted pieces (segment 1 and segment 10) for density, microstructure, and microhardness analysis. Segment 1 and segment 10 are printed with higher scanning speed and lower scanning speed, respectively. Figure 5-19 presents the optical microscopy images of the mirror-polished samples to analyze the presence of defects. It is observed that bent pipe sections are crack-free on the micro-scale, with

few micro-pores at isolated locations. The micro-pores are a combination of gas porosity and lack of fusion porosity. The primary reasons for gas porosity can be the pores inside the feedstock powder used for deposition and gas entrapment during the deposition [105]. On the other hand, the lack of fusion porosity results from incomplete consolidation at a few locations [105]. A comparison of the images indicates that a higher fraction of lack of fusion pores is observed in segment 1 of the bent pipe, which is built using a higher scanning speed. This can be due to the reduction in the laser energy density (LED), which is a ratio between laser power and the product of scanning speed and beam diameter. A reduction in LED can lead to incomplete material consolidation leading to more fraction of the lack of fusion pores. In order to quantify the above, the Archimedes density analysis was carried out by extracting samples along the cross-section of the bent pipe. The measured density values range from 7.75 -7.81 g/cc, and the relative density of the samples was > 98% for all the sections. The relative density of the sample extracted from segments 10 and 1 is 98.11% and 98.89%, respectively. Further, CT analysis of the samples was performed at two selected segments, as shown in Figure 5-20(a) and Figure 5-20(b). Micro-scale pores are seen at random locations, and the results support the Archimedes results indicating higher relative density for both samples.

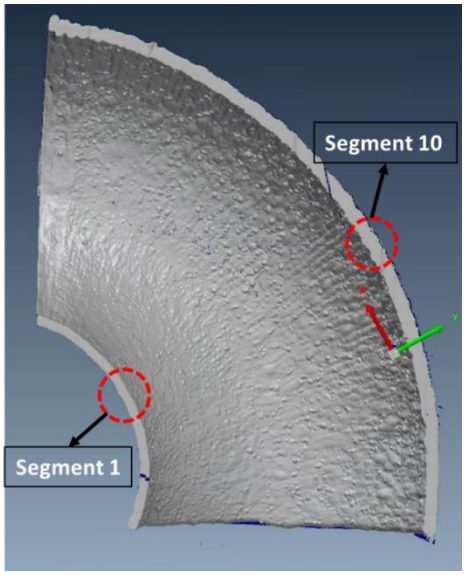


*Figure 5-18: Location of extracted pieces for density, microstructure, and microhardness analysis*

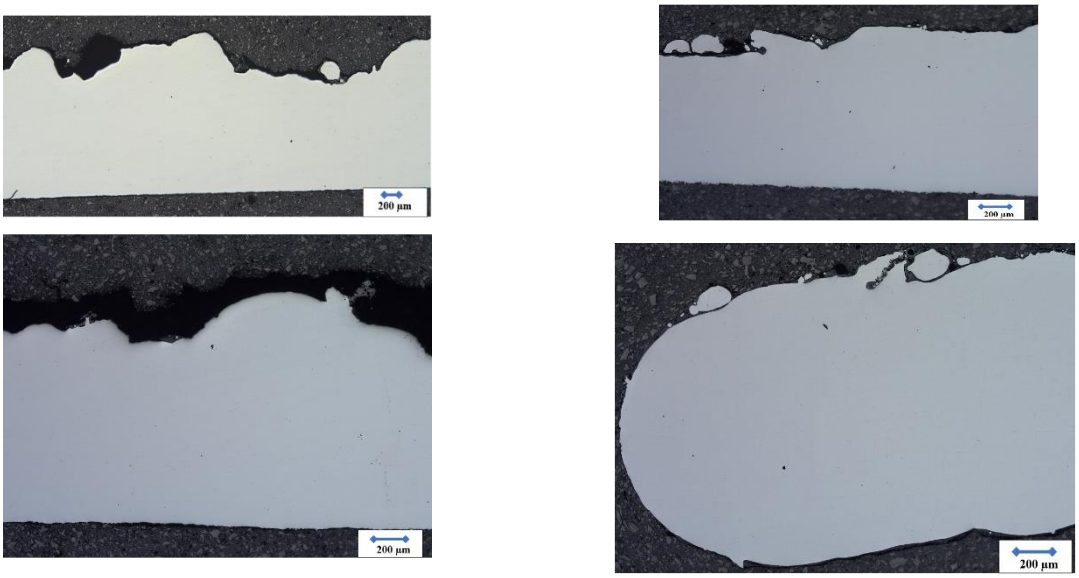


(a) (b)

*Figure 5-19: Optical microscopy images of (a) segment 10 (b) segment 1*


(a)

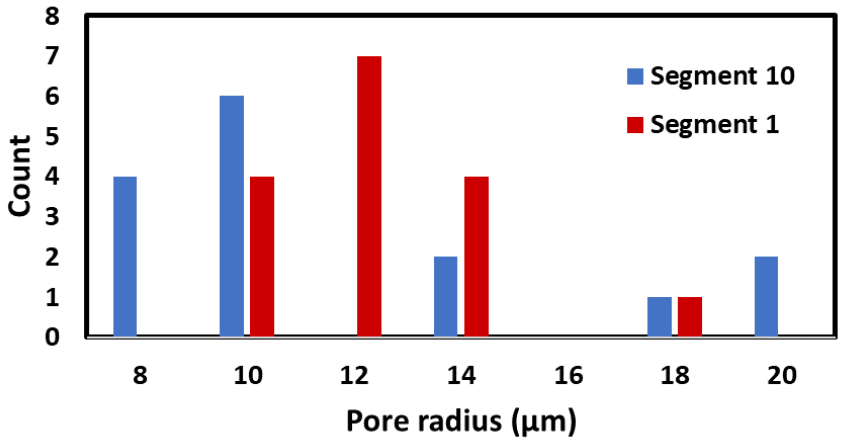


(b)

*Figure 5-20:CT-scan data of Segment 10 and Segment 1 (a) 3D pore distribution (b) pore size*

### 5.4.3 Microstructure

Figure 5-21 (a) and Figure 5-21(b) present the microstructure of segment 10 and segment 1 (refer to Figure 5-18), respectively, at the middle layers. The morphology of the microstructure during LDED is primarily a function of the extent of constitutional undercooling, which is mainly linked to the solidification velocity (R) and the temperature gradient (G). Equations 5-10 and 5-11 indicate the effect of process parameters and material properties on *G* and R, where *T, $T_0$, β, P, K*, and $V_s$ are the liquidus temperature, substrate temperature, laser absorption coefficient of the material, laser power, thermal conductivity, and scanning speed, respectively. θ is the angle between $V_s$ vector's direction and the normal vector of the solid-liquid interface at the tail of the melt pool [32].

$$G = \frac{2K\,(T - T_O)^2}{\beta P} \qquad 5\text{-}10$$

$$R = V_s \cos\theta \qquad 5\text{-}11$$

Figure 5-21 shows the microstructure of samples extracted from segments 1 and 10, which are mainly cellular. In the LDED-built samples, the cellular microstructure is usually formed as a result of higher values of G/R [106]. However, from the measurement on the sample extracted from segment 10 (Figure 5-21(a)), the cell's sizes are in the range of 6-8 μm, while for the segment 1 (Figure 5-21(b)) the cell size value ranges from 2-5 μm, proving the finer microstructure for the latter. This can be due to higher values of scanning speed used for deposition in segment 1, which resulted in notably higher R values based on Equation 5-11 . Moreover, the higher scanning speed increases G × R, which is the cooling rate of the segment [69]. Therefore, at the same process parameters, by increasing the scanning speed, it is expected to see finer microstructures such as those of segment 1 (Figure 5-21 (b)) [107].

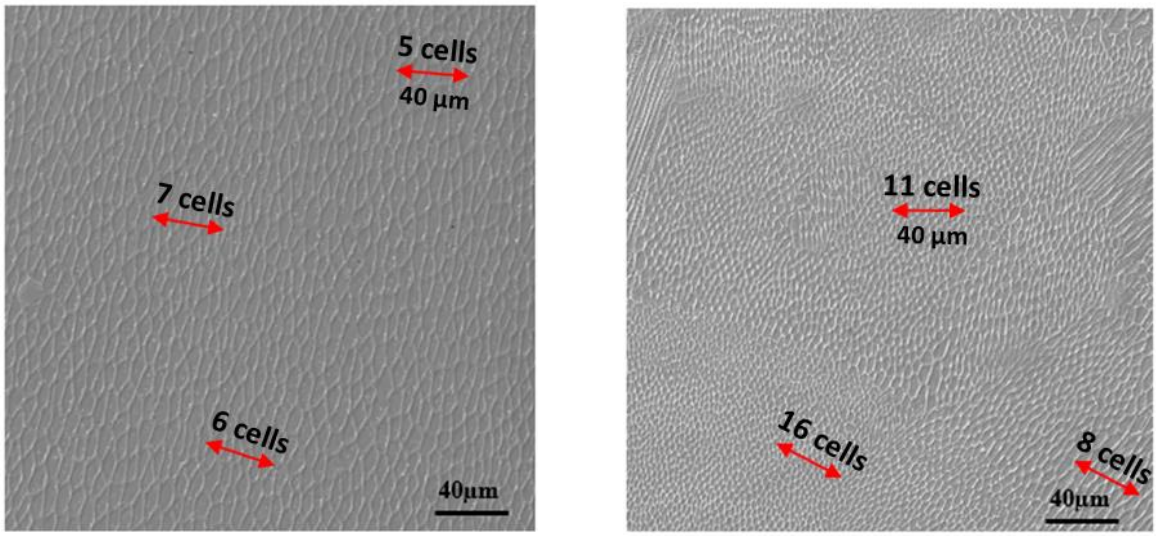


(a) (b)

*Figure 5-21: Microstructure of (a) Segment 10 (b) Segment 1*

### 5.4.4 Microhardness

Micro-hardness values were examined along segments 10 and 1 to evaluate the mechanical properties through the different segments using the experimental setup explained in section 3.6.3. Figure 5-22(a) and Figure 5-22(b) present the indentation along segments 10 and 1, respectively. To have a comprehensive analysis, the three indentations were taken along a single line, and the average value along each line was calculated. Figure 5-22(c) presents the average hardness measured along the section, and it is seen that the microhardness values of segment 1, which ranges from 188 to 203 HV, are found to be higher than segment 10, which ranges from 163 to 179 HV. The higher microhardness values for segment 1 as compared to segment 10 are mainly due to the finer microstructure. This is mainly due to the inverse relationship between the microstructure (cell size in the present case) and microhardness values as per the Halls-Petch relationship. The cell boundaries impede the dislocation motion, which provides a strengthening effect to the material

[108].Thus, the presence of more cell boundaries for finer cellular structure leads to increased strengthening effects, which consequently leads to higher values of microhardness at segment 1.


(a)

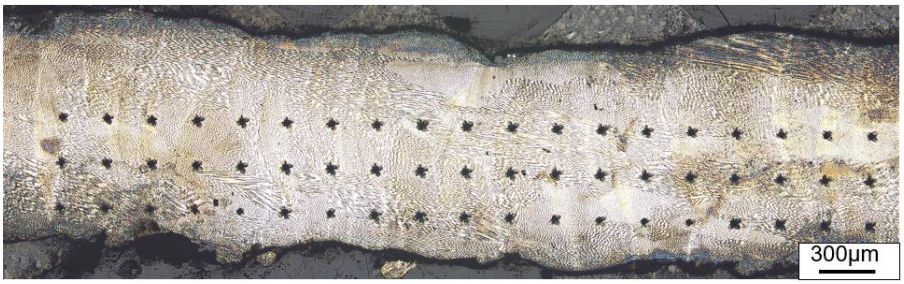


(b)

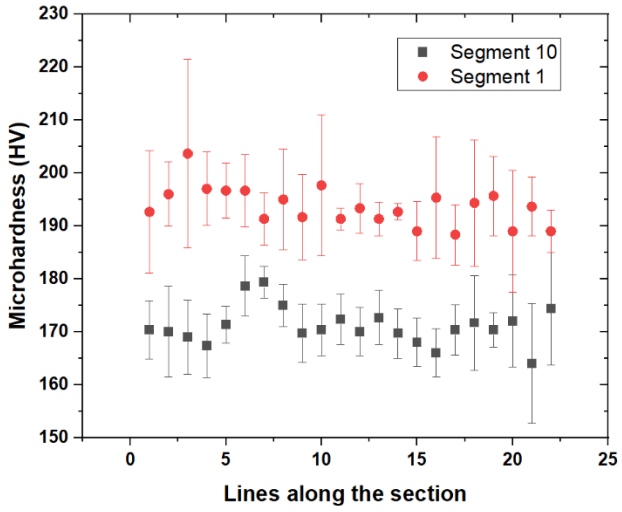


(c)

*Figure 5-22: Microhardness (a) indentations along segment 10 (b) indentations along segment 1 (c) average values along the segment*

## 5.5 Conclusion

The present work focused on the development of process methodology to encounter the challenges involved in the development of complex-shaped near-net-shape tubular components using LDED-PF processes. The developed methodology is validated by building the part, and a comparison with the CAD model shows minimal roundness deviation at different sections. The built bent pipes show density >98% with the presence of few micropores at isolated locations. The microstructure is mainly cellular, and the average microhardness for regions built with lower scanning speed and higher scanning speed is 170 HV and 193 HV, respectively. Thus, the built tubular structures are dense with good dimensional stability without significant variation in the microstructure and mechanical properties between different segments of the tubular geometry.

The subsequent chapter will discuss process monitoring, workpiece localization and point cloud segmentation and deep learning for defect detection of LDED-PF parts.

# 6 Process monitoring, Workpiece localization and Point cloud segmentation and deep learning for defect detection of LDED-PF parts

## 6.1 Introduction

This chapter outlines the development of a novel in-situ monitoring software platform that can be used for the surface anomaly detection of LDED-PF parts using machine learning techniques. Despite the existing methods in the literature, this technique has shown high robustness and high confidence in defect detection regardless of the geometry, and varied density of point clouds. First, a novel method is developed to calibrate the laser line scanner with respect to the robotic end-effector with the sub 0.5 mm accuracy. Subsequently, 2D surface profiles obtained from the LDED-PF built part surface using the laser scanner are stitched together to create an accurate 3D point cloud representation. Further, the point cloud data is processed, and defect detection is carried out using unsupervised learning and supervised (deep) learning techniques. The overall accuracy and mean IoU of 91.3 % and 83.3 % are achieved, respectively. The study paves the way for the development of automatic tool path generation for the LDED-PF process to build high-quality components.

## 6.2 Literature review

LDED-PF has several advantages such as material design freedom, higher build rate, ability to build large-size components [109] and superior material properties [110]. Despite the promising quality of the parts manufactured using the LDED-PF process, defects may occur during the manufacturing process. It is important to identify such defects and take measures to avoid them. The major defects of the LDED-PF include porosity, change in the chemical composition of the material due to segregation and loss of all oying elements, and geometric deviations. Among them, one of the major challenges in the direct deployment of LDED-PF components for real-life

applications is the geometric defects in the LDED-PF parts. The major reasons for geometrical defects in LDED-PF are provided below:

**a) Heat accumulation and residual stresses**

Deviations in dimensional accuracy in different layers are mainly due to heat accumulation; thermal stress generated due to rapid heating and cooling cycles [111]. Scanning strategies used for LDED-PF plays an important role in determining the heat accumulation during LDED. Researchers have investigated the effect of different scanning strategies on the dimensional accuracy and properties of LDED-PF built components [112]. For instance, one of the major effects of the scanning strategy is the built-up that happens at and around edges of turn points due to deceleration of the kinematics system, as shown in Figure 6-1[110-111]. Zheng et al. [115] studied the effect of different scanning strategies on the final dimensional accuracy of the LDED-PF parts. It was concluded that the spiral and circular strategies are suitable for cylindrical shapes. However, the smaller circles or spirals introduce high acceleration to the machine axis and affect the accuracy of the motion system, which eventually can cause build-up errors. The correlation of different scanning strategies such as zigzag, unidirectional, and offset are also studied and their effect on the dimensional accuracy was investigated [116].

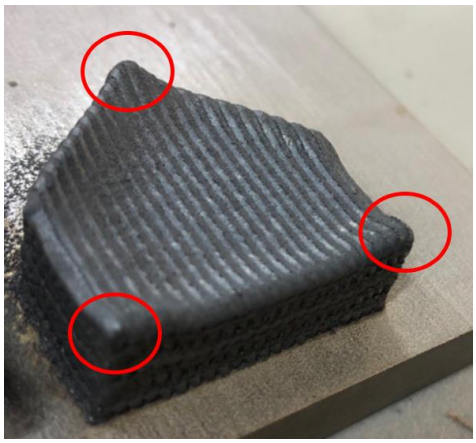

*Figure 6-1: Build-up of the material around the corners in a LDED-PF part*

**b) Non-uniform scanning speed**

Speed profile change during the deposition can cause over deposition in those areas as shown in Figure 6-1. During the deposition in corners and turns, the laser orientation changes suddenly between the successive points, causing a reduction in the scanning speed, which will increase the powder fed per unit length, leading to oversized depositions. Boisselier et al. [114] studied the effect of scanning speed variation and its effect on the dimensional accuracy of the LDED-PF geometry. They also found an experimental correlation between the track height and the scanning speed. The effect of the scanning speed variation in the final bead geometry is shown in Figure 6-2, where the start and end points of the tracks in LDED-PF are also prone to acceleration and deceleration of the laser head, which leads to over deposition at start and end points of a single track as shown in Figure 6-3.

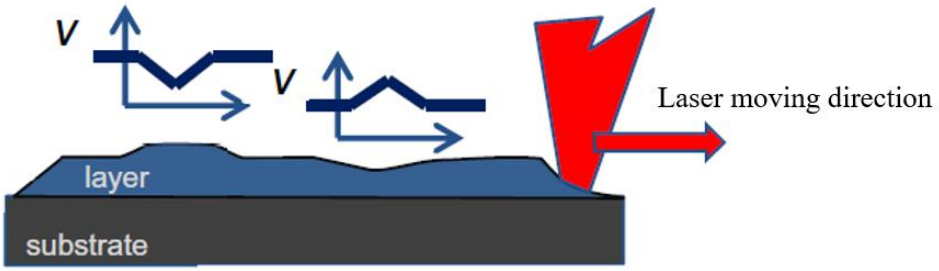


*Figure 6-2: Effect of scanning speed variation in the geometry of the beads in LDED-PF*[77]

Liu et al.[117] studied the effect of toolpath smoothing on the dimensional accuracy of LDED-PF parts. Although this technique can improve dimensional accuracy, they require extensive pre-process planning, and they are highly dependent on scanning strategies.


*Figure 6-3: Effect of acceleration and deceleration of the deposition head on the start and end point of a single track*

**c) Unstable working distance between the nozzle tip and the substrate**

Another source of inconsistency in the accuracy of the dimensions in LDED-PF can be related to inconsistent layer growth in contrast to the nominal layer height. This can lead to surface unevenness on the top layers, especially for thin-walled parts. When the layer growth is not equal to the nominal layer height, the laser and powder defocusing distance increases [118]. Based on the process parameters, the defocusing distance value can be negative or positive. In the LDED-PF process, a slight difference usually exists on the top surface of the part [119]. This is mainly

due to fluctuation in the process parameters, or unevenness of the substrate. Once there are some height differences in the first layer, the difference will increase after each layer due to the accumulation of error. In the case of the positive defocusing distance (increasing the distance between the nozzle tip and the powder focus), this difference will become more and more and the layer growth will not be enough to compensate the theoretical layer height in each layer as shown in Figure 6-4(a). In case of negative defocusing distance, layer growth will be more than the theoretical layer height and energy density will be altered and the process will become unstable as shown in Figure 6-4(b) [120]. The proper alignment of the powder and laser will result in manufacturing a part with a flat top surface as shown in Figure 6-4(c).

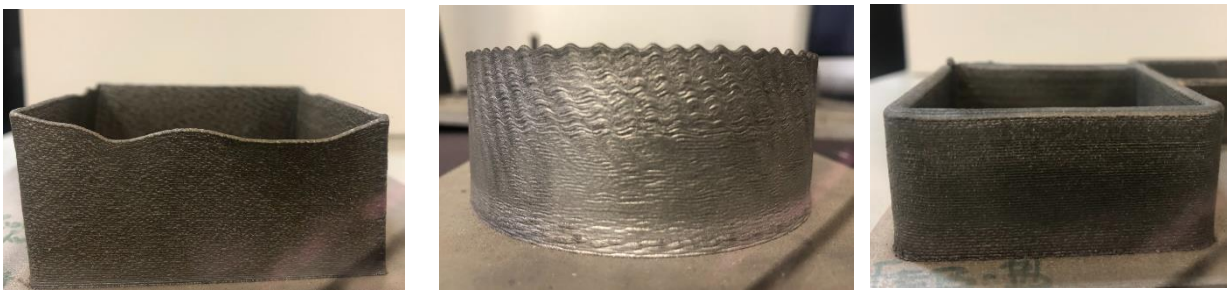

(a) (b) (c)

*Figure 6-4: Effect of (a) negative defocusing distance on the top surface evenness, (b) focused laser and powder top surface, (c) effect of positive defocusing distance on the top surface evenness*

Another source of inconsistency is the higher values of layer growth at the top layers as compared to the bottom layers due to the higher powder catchment efficiency at the top layers. This is mainly due to the preheating effect at the top layers resulting in larger melt pool dimensions at the top layers. This will lead to defocusing of the powder and laser, which will eventually cause the process failure [121].

### 6.2.1 In-situ monitoring and process control

In-situ monitoring and process control are used to improve the quality of the parts and eliminate the defects generated during LDED-PF. These techniques allow the user to ensure the geometrical and structural quality (dense parts without internal defects such as pores and cracks) [122]. In-situ monitoring and process control are used to improve the quality of the parts and eliminate the defects generated during LDED-PF. These techniques allow the user to ensure the geometrical and structural quality (dense parts without internal defects such as pores and cracks)[123]. Contactless sensor-based techniques are mainly used for process monitoring in LDED-PF due to the high temperature involved during the process. The most commonly used contactless sensors for monitoring the melt pool (temperature, brightness and intensity) are thermal cameras, infrared sensors, and photodiodes [12][120-121]. Also, CMOS and CCD cameras are used both co-axially and off-axis to monitor the dimensions of the melt pool [123–127]. The off-axis configuration is direction-dependent, and it is normally used for monitoring the deposition of single tracks. This configuration permits the measurement of track height and track width. Whereas the co-axial configuration can be used to monitor and measure the track width. However, off-axis configuration may produce inconsistent measurement data depending on the orientation of the deposition head [127-128].

Laser line scanners show great potential for 3D surface quality assessment in LDED processes [133]. Compared to other vision techniques, they have a higher resolution, which allows the generation of accurate data without computationally extensive 3D reconstruction. The working principle of the laser line scanner in a robotic system is shown in Figure 6-5. The distance between the target and the camera is measured by the triangulation principle. The sensor consists of a laser

projector, which projects a laser strip onto the target surface and a light-receiving element (normally a CMOS camera) is used to detect the light emitted from the laser line to the surface.

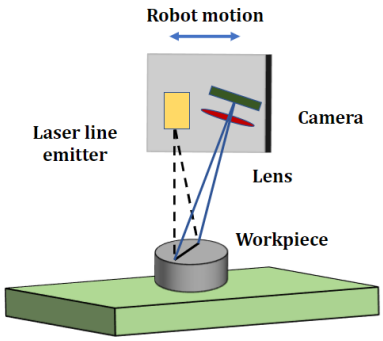


*Figure 6-5: Working principle of laser profiler for 3D surface topography*

The deployment of a laser line scanner for process monitoring is reported by several researchers. Heralic et al. introduced the combination of the laser line scanner and CMOS camera for controlling the track geometry (track height and track width) [134]. Tang et al. proposed adaptive process parameter control within different layers based on the height measurement of the previous layer using a laser line scanner [135]. Iker et al. presented a solution to maintain a constant working distance during deposition based on the height measurement. Due to the harsh process environment during LDED-PF, the deposition was stopped during the process and the workpiece height was measured using a structured light laser scanner [132-133]. Ertveldt et al.[12] developed a platform for process monitoring and control of the LDED-PF process where intra-layer height measurement is carried out using a laser line scanner and the melt pool width is analysed using the coaxial CMOS camera. The authors aimed to use the melt pool and laser line scanner information in a machine learning platform to integrate it with the control algorithms for robust geometry prediction and control.

During LDED-PF, inconsistency with the predicted workpiece growth results in powder defocusing, which leads to a significant reduction in dimensional accuracy. It was shown that the quality is better when the powder focal plane is slightly above the laser focal plane [138]. In the uncontrolled LDED-PF process, a theoretical layer height lower than the actual growth is used to maintain the powder focus below the substrate. This will lead to constraints for part growth and building rate as well as lowering the catchment efficiency and increasing the powder wastage.

CMOS and CCD cameras are widely used as economical solutions for relatively fast feedback to adjust the process parameters and thereby maintain the required height without stopping the process. However, they introduce complexity to the system as they often require calibration based on the process parameters. Therefore, a complementary solution is required to modify the deposition trajectory based on the actual height for the complex geometries. Chen et al. [139] developed an in-situ surface reconstruction software platform for a robotics system using Robot Operating System (ROS). The authors identified the surface defects of LDED-PF parts in-situ without stopping the process. Supervised and unsupervised machine learning techniques are used to identify the error regions on the deposition surface. Li et al. [140] used a stereovision system to obtain the surface topography of the LPBF parts. The cameras have overlapped views of the monitored surface and the pixels are converted to the point clouds using Digital Image correlation.

García-Díaz et al.[141] introduced a real-time visualization platform using a laser line scanner (combination of a laser strip coupled to a CMOS detector) and near infra red camera. The laser line scanner was used to monitor the surface of the LDED-PF parts in real-time. ROS was also used for the integration of the sensors with the robotics system.

### 6.2.2 Error quantification using machine learning

Statistical techniques are commonly used for surface quality assessment of AM built components. Being a multi-physics phenomenon, the underlying reasons for the defect formation in AM are complicated. Statistical techniques can provide prediction and modelling tools for error formation occurrence and characteristics, respectively. Machine learning is an emerging technique for error and defect classification in AM technologies. The literature survey indicates that various machine learning models were employed to correlate the surface defects with the process parameters [142].

one of the fast-growing approaches in material processing, especially for complex multi-physics processes such as welding [140-141], and AM for process monitoring and quality prediction [142-143]. Deep learning techniques for 3D semantic segmentation have also shown promising results [147].

Taherkhani et al. [85] developed a data-driven platform for defect detection of LPBF parts using the signal collected from a photo diode monitoring the melt pool. Ren et al. [148] applied Convolution Neural Network (CNN) technique for minimizing the surface deviation resulting from the residual stress and distortion. The model was used to predict the best scanning strategy for the next layer to avoid surface errors. Chen et al. [139] applied a combination of unsupervised learning and supervised learning to identify the surface errors in the LDED-PF process. Statistical features of the error regions are extracted and identified in unsupervised learning as the input for supervised learning, which used 73 samples. Ogoke et al. [149] presented a deep reinforcement learning framework to control the LPBF process to maintain the melt pool dimensions in real-time by controlling laser power and scanning speed.

### 6.2.3 Deep learning for point clouds

Applying deep learning techniques to segment point cloud data is a challenging task. Some of the challenges are [150] :

a) Irregularity in the distribution of the points. The irregularity in the distribution of the points across the different areas of the target surface leads to some areas having dense points, while other areas having sparse points.
b) Lack of structure in the point cloud: Point clouds are not structured on regular grid-like 2D images. Point to point distance is different for each point and the points are scanned independently.
c) Lack of order in the point cloud: Point clouds are a series of points represented in XYZ usually stored as a list. However, the order that the data has been stored, does not match the order of the object representation.

The above-mentioned properties of the point clouds are very challenging for deep learning techniques, especially CNN. Specific libraries have been developed for segmentation of point cloud data based on two techniques:

a) 2D projection networks: Many networks have been developed to leverage the power of CNNs to project 3D point clouds to 2D images for object detection. However, geometric features and details may be lost during the transformation. The model achieves good accuracy on segmentation, but they are computationally expensive [147–149].
b) Point-based networks including: PointNet[154], PointNet++ [155].: The fundamental idea of PointNet is learning a spatial encoding for each point followed by aggregation of all individual point features to a global point cloud registration. PointNet based works show good results on

smaller point clouds, but they cannot directly process and segment point clouds due to memory and computational cost.

The comprehensive literature review section provides the baseline for new research opportunities to improve the efficiency and productivity of LDED-PF. LDED-PF normally suffers from the lack of dimensional accuracy and surface quality, however, in-situ surface quality assessment and automatic toolpath generation may provide remedies to overcome the challenges. Laser surface scanning proves to be one of the techniques that can be used for in-situ monitoring of surface defects generated during LDED-PF. However, the current techniques for surface quality assessment of LDED-PF parts suffer from technological gaps such as:

a) The in-situ monitoring techniques reported in the literature mainly uses intermittent surface quality assessment, where the process is stopped for scanning after deposition of a few layers, which is followed by process planning for improving the dimensional accuracy.
b) Point cloud pre-processing techniques are time-consuming, and they introduce delays and latencies into the surface quality assessment.
c) Previous efforts on the deployment of laser scanning for quality assurance of the LEDD-PF mainly focus on simple planar geometries, where the main advantages of LDED-PF such as 5-axis deposition and free-form manufacturing are not challenged.

The literature indicates that the proposed objectives are original and may develop a reliable platform to address some of the current quality challenges of LDED.

## 6.3 Software architecture

A Lab-VIEW-based software platform is developed for communication between the robot controller through TCP/IP protocol using the FANUC's PCDK (PC Developer's toolkit) to retrieve the position, velocity, and status of the robotic arm in real-time. It is also connected to the laser profiler using Ethernet/IP. A 3D point cloud of the printed LDED-PF parts can be generated using the position of the laser scanner frame during the scan and the laser scanner profile coordinates, which are both acquired and processed by the LabVIEW interface. The software architecture is shown in Figure 6-6.

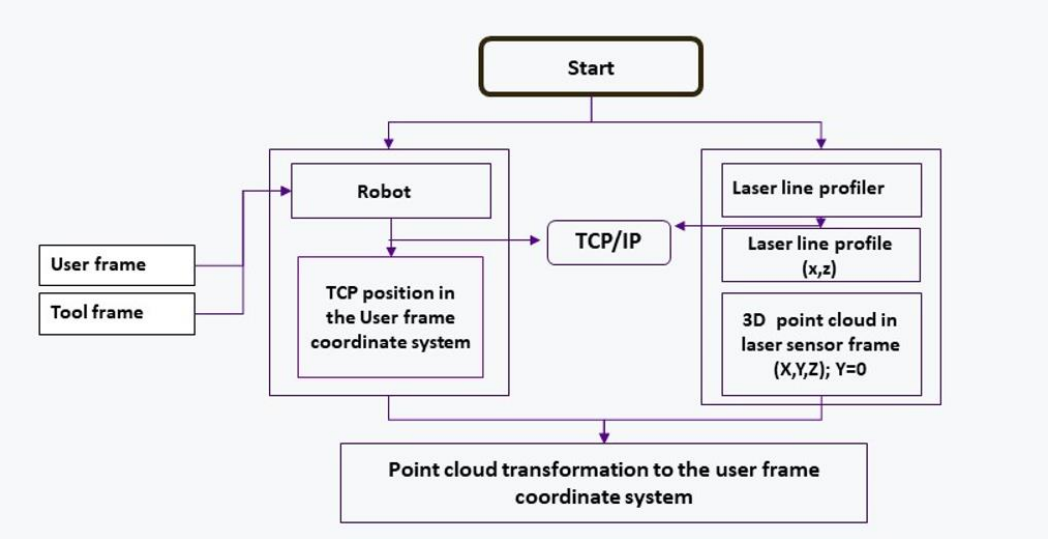


*Figure 6-6: Software Architecture*

## 6.4 Workpiece localization

The localization of the workpiece in the robot base frame is the first step for in-situ surface quality assessment of LDED components built using a robotic system. The transformation between the laser sensor frame and the robot 6$^{th}$ axis frame is required. The procedure of finding the geometric relationship of the laser profiler sensor frame and the robot 6$^{th}$ axis frame is known as the *hand-eye* calibration method [156]. This method tries to estimate the homogenous transformation matrix

between the robot 6th axis frame and the laser scanner sensor that is mounted on the robot 6th axis with an offset.

To perform the hand-eye calibration, it is necessary to locate a fixed object in the robot world coordinate system. In this research, a calibration sphere with a diameter of 25.4 mm is used as a fixed point with the coordinates of $P_l = [\, x_L, y_L, z_L, 1]^T$ . $T_{RF1}$ and $T_{RF2}$ are the transformation matrices between the robot global fixed coordinate system and the robot 6th axis frame, respectively as shown in Figure 6-7. $T_{FS}$ is the 4×4 transformation matrix between the robot 6th axis coordinate system and the laser profiler sensor coordinate system and it is assumed to be constant, if the sensor is rigidly mounted on the robot 6th axis. Therefore, the hand-eye calibration technique can be formulated as shown in Equation 6-1 [157].

$$T_{RF1}\, T_{FS} P_{L_1} = T_{RF2} T_{FS} P_{L_2} \qquad 6\text{-}1$$

where, $P_{L_1}$ and $P_{L_2}$ are the center of the calibration sphere in the laser profiler sensor frame in the first and second configuration of the robot as sown in Figure 6-7(a) and Figure 6-7(b) respectively. Therefore, the $T_{FS}$ is the only unknown in Equation 6-1 .

Equation 6-1 can be alternatively written as Equation 6-2 by multiplying both sides of Equation 6-1 by $T_{RF2}^{-1}$ and $P_{L1}^{-1}$.

$$AT_{FS} = T_{FS} B \qquad 6\text{-}2$$

where, $A = T_{RF2}^{-1}\, T_{RF1}$ and $B = P_{L_2}\, P_{L1}^{-1}$.

6-2 can be simplified to $AX = XB$ , where $X = T_{FS}$. In the literature, different techniques are presented to solve the $AX = XB$. One of the most practical techniques used in industry is called a two-stage technique. This technique solves 6-2 by decomposing it into two consecutive parts.

Initially, the rotation matrix between the robot 6th axis frame and the laser profiles sensor frame is estimated. In the second part, the translation matrix between the robot 6th axis frame and the laser profiler sensor is estimated.

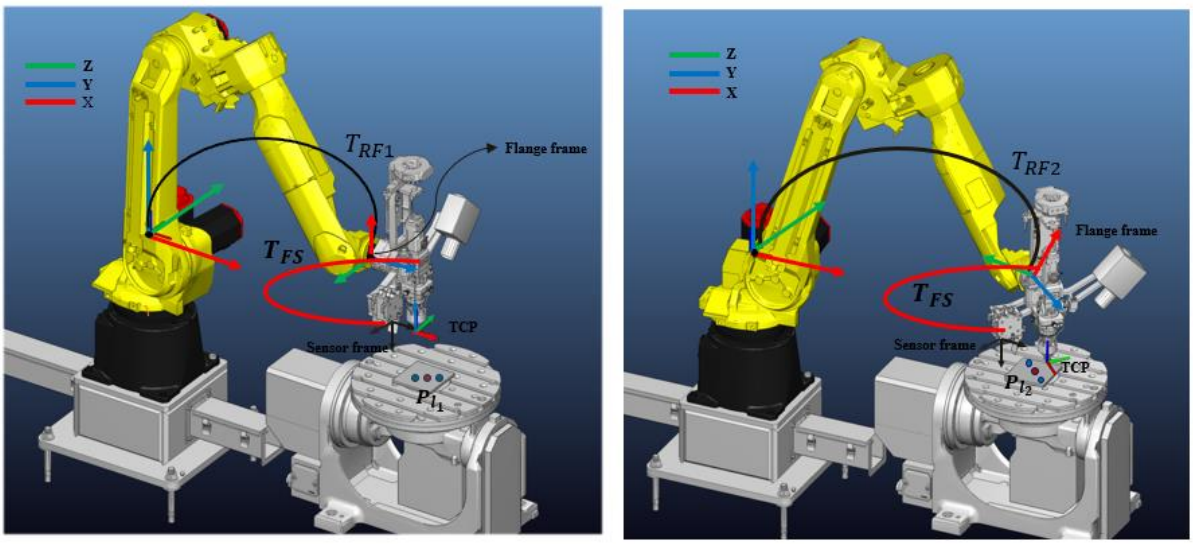


(a) (b)

*Figure 6-7 :Schematic representation of hand-eye calibration steps for the Fanuc M-20iA robot and laser profiler sensor (a) robot in a first known kinematic position (b) robot in the second known kinematic position*

### 6.4.1 Calculation of center of calibration sphere in laser scanner coordinate system

6-2can be re-written as Equation 6-3 where $P_R$ is the center of the calibration sphere in the robot world coordinate system; $R_{RF}$ and$t_{RF}$ $a$re the rotation and translation matrix of between the robot world coordinate system and the flange coordinate system, respectively; $R_{FS}$ and $t_{FS}$ are the rotation and translation matrix between the robot 6th axis and the laser scanner frame, respectively; $P_l$ is the center of calibration sphere in the laser scanner frame.

$$\begin{bmatrix} P_R \\ 1 \end{bmatrix} = \begin{bmatrix} R_{RF} & t_{RF} \\ 0 & 1 \end{bmatrix} \begin{bmatrix} R_{FS} & t_{FS} \\ 0 & 1 \end{bmatrix} \begin{bmatrix} P_l \\ 1 \end{bmatrix} \quad 6\text{-}3$$

First, the center of the calibration sphere in the laser scanner frame is calculated. When a laser stripe is projected to the sphere surface, a 2D profile can be obtained from the laser scanner as shown in Figure 6-8(a) and Figure 6-8(b). The obtained curve is shown in Figure 6-8(c). A circle is fitted to the arc using the least square method and the center and the radius of the circle is calculated. The calculated center is denoted as $S_x$ and $S_z$. Further, the calculated radius of the fitted circle is used to find the value $S_y$ as shown in Figure 6-8(b) (refer to Equation 6-4), where $R_s$ is the radius of the calibration sphere, and $r$ is the radius of the circle fitted to the profile obtained from the laser scanner.

$$S_y = \pm\sqrt{R_s^2 - r^2} \quad 6\text{-}4$$

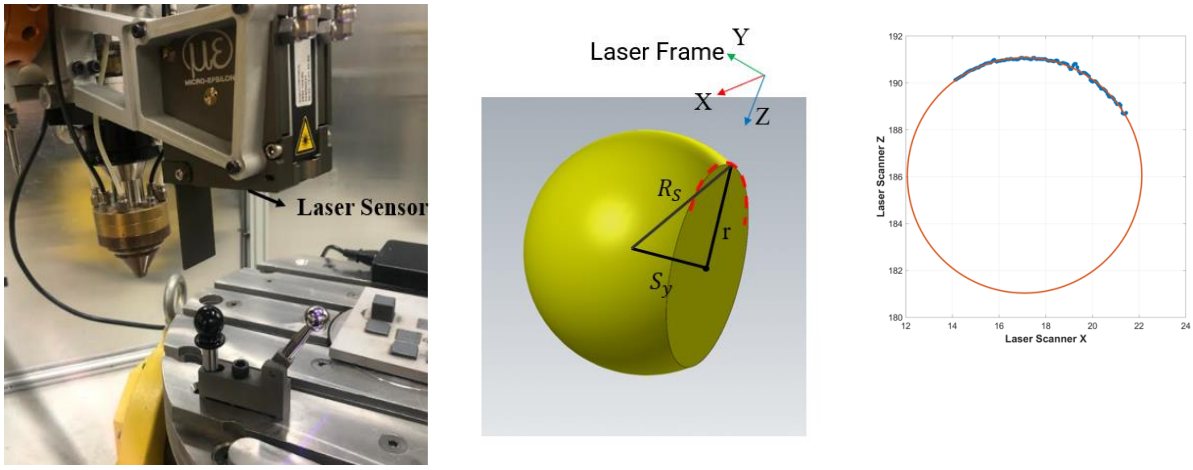


(a) (b) (c)

*Figure 6-8: (a) Laser scanner stripe on the calibration sphere, (b) Calculation of center of calibration sphere, (c) fitted circle to the projected laser stripe*

### 6.4.2 Calculation of rotation matrix component

For two consecutive profile measurements, Equation 6-3 can be rewritten as Equation 6-5.

$$R_{RF}^{k}.R_{FS}^{k}.P_{L}^{k} + R_{RF}^{k}.t_{FS}^{K} + t_{RF}^{k} = R_{RF}^{k+1}.R_{FS}^{k+1}.P_{L}^{k+1} + R_{RF}^{k+1}.t_{FS}^{k+1} + t_{RF}^{k+1} \quad 6\text{-}5$$

If the orientation of the robot 6th axis frame is unchanged during the two consecutive profile measurements, Equation 6-5can be re-written as Equation 6-6.

$$\boldsymbol{R_{FS}}.\left[P_{L}^{k} - P_{L}^{k+1}\right] = [R_{RF}]^{-1}.[{t_{RF}}^{k+1} - {t_{RF}}^{k}] \quad 6\text{-}6$$

If we consider that $D = \left[P_{L}^{k} - P_{L}^{k+1}\right]$ and $E = [R_{RF}]^{-1}.[{t_{RF}}^{k+1} - {t_{RF}}^{k}]$, Equation 6-6 can be re-written as Equation 6-7.

$$R_{FS}.D = E \quad 6\text{-}7$$

$R_{FS}$ is a 3×3 matrix and *D and E* are 3 ×2 matrices. Since *D and E* are not square matrices, $R_{FS}$ can be estimated using the Singular Value Decomposition (SVD) of the $DE^{T}$ and using its right ($V$) and left ($U$) values as shown in Equation 6-8.

$$R_{FS} = VU^{T} \quad 6\text{-}8$$

It has to be noted that the two profile measurements for this step do not provide the required accuracy, and thus, eight measurements are needed to improve the accuracy.

### 6.4.3 Calculation of translation matrix component

In the second step of the two-stage solution, the translation between the two consecutive robot poses will be kept constant, when the profile measurement is taking place. Therefore Equation 6-9, is substituted in Equation 6-5 to obtain Equation 6-10.

$$t_{RF}^{k} = t_{RF}^{k+1} \quad 6\text{-}9$$

$$[R_{RF}^{k} - R_{RF}^{k+1}].\boldsymbol{t_{FS}} = [R_{RF}^{k+1}.R_{FS}.P_{L}^{k+1} - R_{RF}^{k}.R_{FS}.P_{L}^{k}] \quad 6\text{-}10$$

If $A = [R_{RF}^{k} - R_{RF}^{k+1}]$ and $[B = R_{RF}^{k+1}.R_{FS}.P_{L}^{k+1} - R_{RF}^{k}.R_{FS}.P_{L}^{k}]$, Equation 6-10 can be re-written as a system of the linear equation as shown in Equation 6-11.

$$Ax = B \quad 6\text{-}11$$

Further, Equation 6-11is solved to calculate $\boldsymbol{t_{FS}}$.

### 6.4.4 Validation of hand-eye calibration

Once the position and orientation of the laser sensor frame were obtained, it was provided to the robot controller as a tool frame. Then the surface of the calibration sphere ($D = 25.4\,mm$) was scanned in three different robot positions. The point cloud obtained from each measurement was fitted to a sphere using the least square technique and the center and the radius of the fitted sphere were calculated. Figure 6-9 shows the validation process and the spheres fitted to the point clouds. Table 6-1 shows the standard deviation of the sphere coordinates ($S_x, S_y\ and\ S_z$) and the radius of the sphere ($R_s$). These results show a good accuracy (sub 1mm) in workpiece localization, and it verifies that the robot can be used for in-situ surface reconstruction of LDED-PF parts.

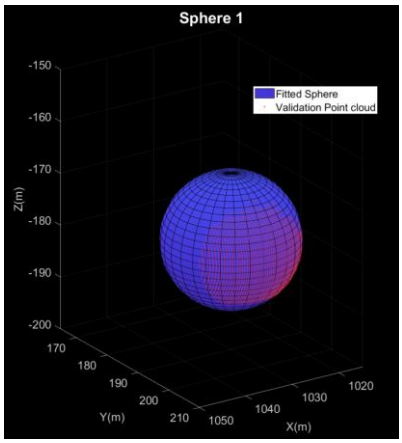


| Robot Position and Orientation | | | |
|---|---|---|---|
| X | 918.10 | W | 89.96 |
| Y | 577.43 | P | 18.95 |
| Z | -365.45 | R | 89.89 |

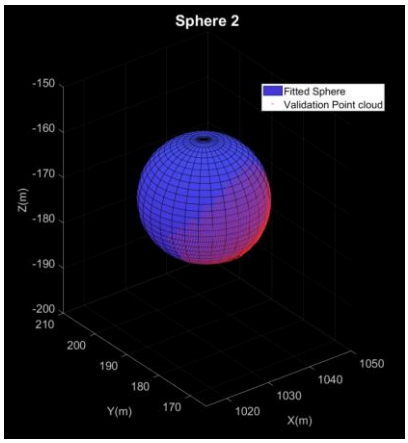


| Robot Position and Orientation | | | |
|---|---|---|---|
| X | 872.72 | W | -90.10 |
| Y | -150.46 | P | -18.89 |
| Z | -4.93 | R | -89.89 |

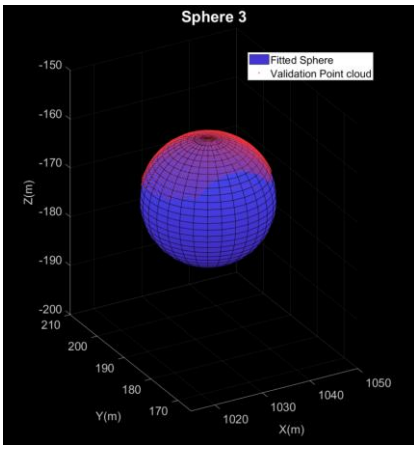


| Robot Position and Orientation | | | |
|---|---|---|---|
| X | 896.76 | W | 91.749 |
| Y | 363.52 | P | -71.281 |
| Z | 105.54 | R | 88.392 |

*Figure 6-9: Validation of the hand-eye calibration technique*

*Table 6-1: Standard deviation of center and radius of the fitted sphere to the point clouds*

| Coordinates | $S_X(mm)$ | $S_y(mm)$ | $S_Z(mm)$ | $R_s(mm)$ |
|---|---|---|---|---|
| Standard deviation of measurements | 0.752 | 0.568 | 0.452 | 0.389 |

## 6.5 Surface quality assessment using point cloud processing

The geometrical deviations in LDED-PF made parts can be categorized as three main groups: 1) Normal surface, 2) Convex surface and 3) Concave surface as shown in Figure 6-10. In this research, the areas that potentially contain these surface defects are isolated initially and they are automatically annotated as defects. The annotated data is then used for defect detection using a deep learning algorithm.

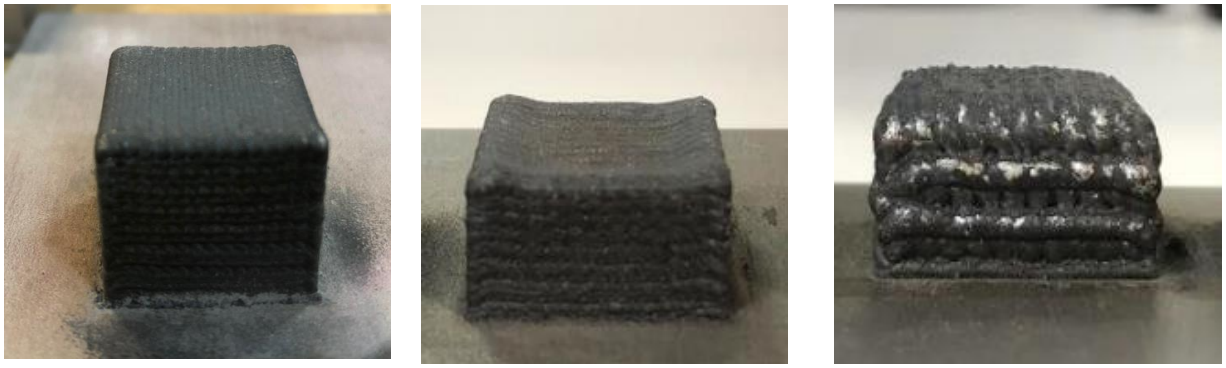

(a) (b) (c)

*Figure 6-10(a) example of normal surface, (b) example of concave surface, (c) example of the convex surface*

## 6.6 Point cloud pre-processing

Once the surface profile point cloud is transformed, it needs to be pre-processed, filtered, and segmented. The point cloud pre-processing algorithm flowchart is shown in Figure 6-11.

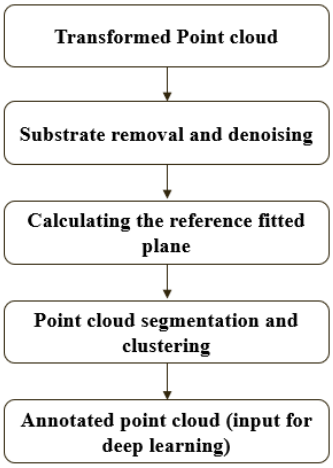


*Figure 6-11: Point cloud pre-processing algorithm flowchart*

Figure 6-12 (a) shows a typical specimen built using LDED-PF. The raw point cloud from the sensor contains the substrate and other objects including fixtures as shown in Figure 6-12(b). The user frame of the robotic system is defined in a way that the height of the substrate in the active

user frame is zero in the active tool frame coordinate system. It is critical to isolate the target surface from the substrate to be able to identify the geometrical defects. The M-estimator SAmple Consensus (MSAC) algorithm is used to remove the substrate from the point cloud using statistical outlier removal [158]. MSAC uses repeated sub sampling to divide the data into inliers and outliers. Inliers are the data whose distribution can be explained by the model parameters. In the point cloud and substrate case, the inliers are the points that can fit into a plane. The substrate is considered to be a plane and any other data points are considered as outliers that do not fit the model. The raw point cloud also includes the noise (as shown in Figure 6-12(c)) that is caused by the steep vertical walls that cannot be properly captured due to the physical limitations of the scanner, and the reflection of the deposited surface. The expected height of the deposited layer can be estimated using the layer height resulting from a set of process parameters. The average height of the points in the point cloud and their standard deviation are used for statistical outlier removal. The noise removal algorithm iterates through the points and removes the sparse points that do not belong to the target deposition surface out of the range as shown in Equation 6-12.

$$h_{max}, h_{min} = Mean(PC_z) \pm \beta \sigma_{PC_z} \quad 6\text{-}12$$

where, $PC_z$ is the height of each point in the point cloud, $\sigma_{PC_z}$ is the standard deviation of $PC_z$ , $\beta$ is experimentally estimated using different datasets and its value is set to 5 based on the experiments and $h_{max}\ and\ h_{min}$ are the z value of the maximum and minimum points in the point cloud, respectively.

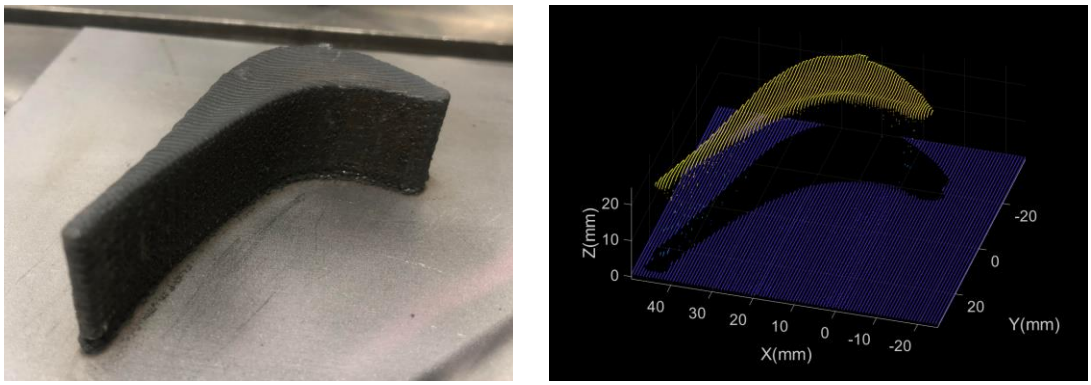


(a) (b)

(c) (d)

*Figure 6-12: (a) Printed LDED-PF sample, (b) Raw point cloud obtained from the sensor, (c) processed point cloud after substrate removal, (d) clean point cloud*

## 6.7 Point cloud segmentation

After the substrate removal and point cloud denoising, a plane is fitted to the point cloud using the total least squares (TLS) method [159]. The principle of the TLS method is shown in Figure 6-13. The point cloud data is stored in a N×3, where N is the number of points in the point cloud. The normal vector of the best-fitted plane using TLS is found using Equation 6-13.

$$M = UDV^T \qquad 6\text{-}13$$

Where $M$ is the N×3 point cloud matrix and U, D and V are the Right, Bottom and Left components of the Singular value decomposition, respectively. The corresponding left singular vector is the normal vector of the best fitting plane.

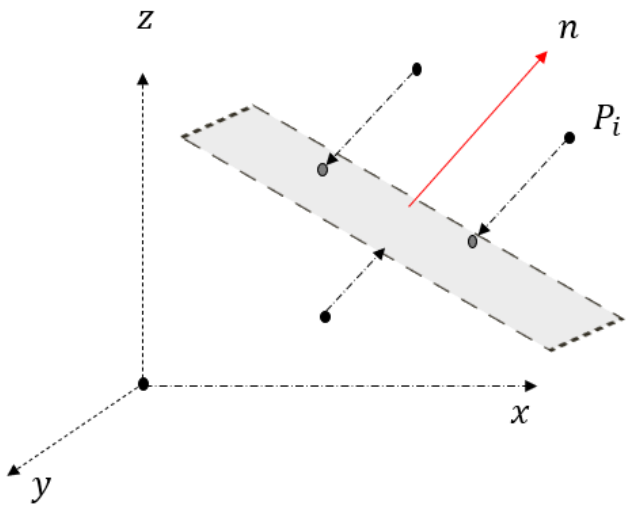


*Figure 6-13: Principal of Total Lease Square (TLS) surface fitting*

After finding the plane using TLS, the plane equation can be written as Equation 6-14:

$$ax + by + cz + d = 0 \qquad 6\text{-}14$$

For each point of the obtained point cloud, the Euclidean distance from the reference plane can be calculated as shown in Equation 6-15:

$$\left|l_{P_i}\right| = \frac{aP_{x_i} + bP_{y_i} + cP_{z_i}}{\sqrt{a^2 + b^2 + c^2}} \qquad 6\text{-}15$$

where, $i$ is the index of the points in the point cloud, and $l_{P_i}$ is the calculated Euclidean distance from that point to the fitted reference plane.

The direction of the $l_{P_i}$ can be found using the Normal vector of the plane calculated as presented in Equation 6-16:

$$N = \frac{[a, b, c]}{\sqrt{a^2 + b^2 + c^2}} \quad \text{6-16}$$

Based on the value of $l_p$, the point clouds are divided into 3 subclasses (refer to Figure 6-14) as follows:

a) Points with deviation higher than the $+l^*$ from the fitted reference plane are grouped as a convex class (Equation 6-17):

$$P_{convex} = \{p_i \in PC \mid l_{pi} > +l^*\} \quad \text{6-17}$$

$$\text{where, } l^* = \frac{1}{2} \times layer\ height$$

b) Points with deviation lower than the $-l^*$from the fitted reference plane are grouped as a concave class (Equation 6-18):

$$P_{concave} = \{p_i \in PC \mid l_{pi} < -l^*\} \quad \text{6-18}$$

$$\text{where, } l^- = -\frac{1}{2} \times layer\ height$$

c) Points with deviation higher than $-l^*$ and lower than $+l^*$ from the fitted reference plane are grouped as a normal class (Equation 6-19):

$$P_{normal} = \{p_i \in PC \mid -l^* < l_{pi} < +l^*\} \quad \text{6-19}$$

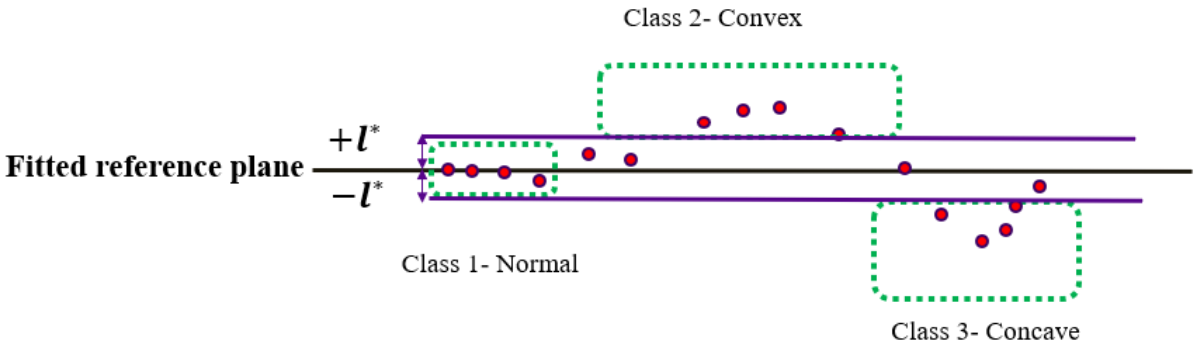


*Figure 6-14: Classification of surface defects based on the Euclidean distance from the fitted reference plane*

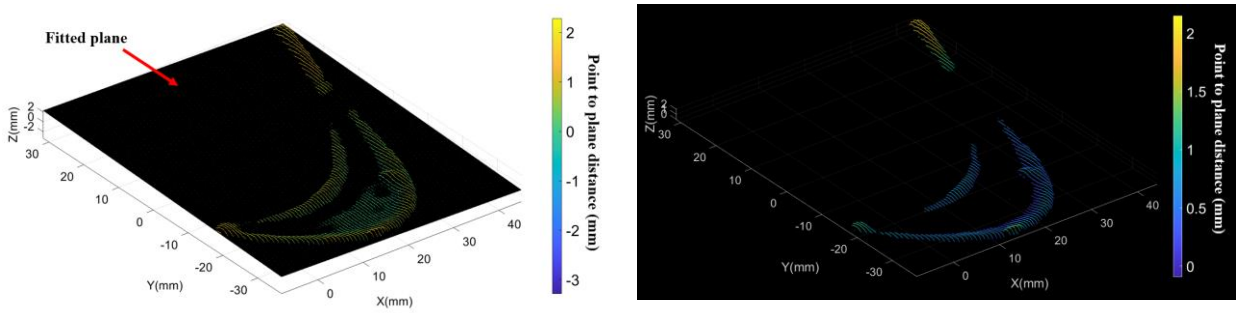


(a)




(b)

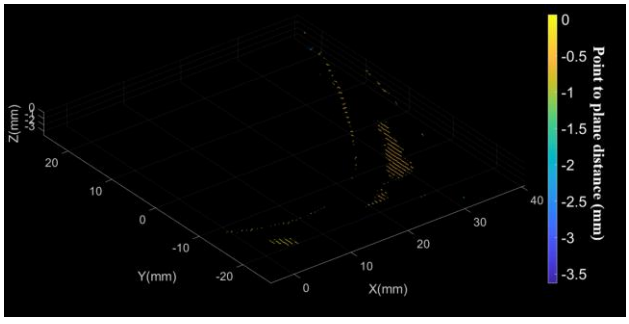


(c)

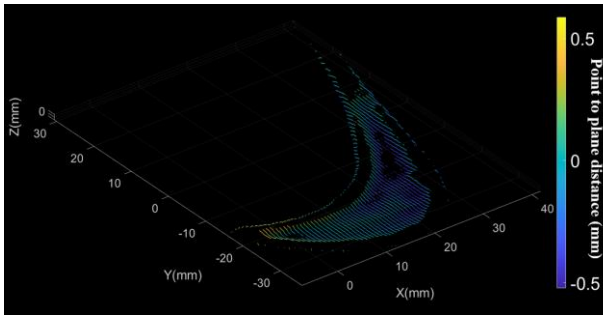


(d)

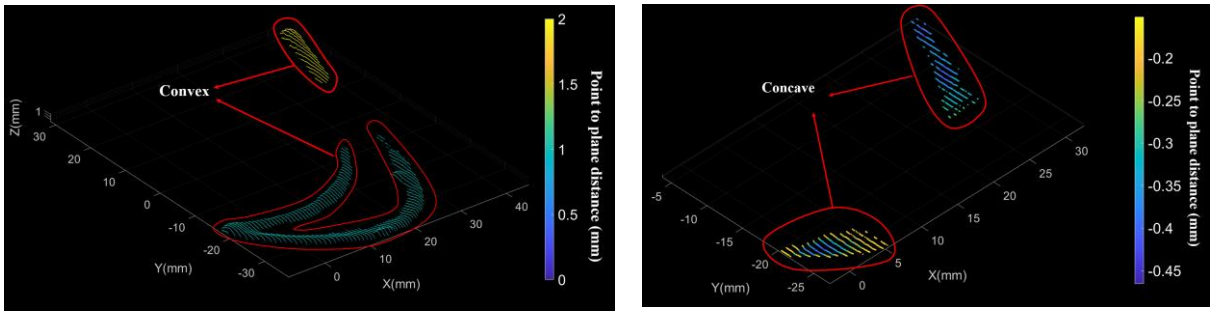


*(e)* (f)

*Figure 6-15: (a) TLS plane fitted to the point cloud, (b) point cloud segmentation, convex region, (c) point cloud segmentation, concave region (d) point cloud segmentation, normal region, (e) Defect region segmentation, Convex, (f) Defect region segmentation, Concave*

The fitted reference plane overlaid on its reference point cloud is shown in Figure 6-15(a). The convex, concave regions of the point cloud are shown in Figure 6-15(b) and Figure 6-15(c), respectively. Once the convex, concave, and normal regions of the point cloud are found, a density-based clustering algorithm following the minimum Euclidean distance between points from different clusters is used to segment the point cloud into clusters (DBSCAN (Density-based spatial clustering of applications with noise)). The DBSCAN cluster extraction algorithm [160] is selected due to its efficiency and capability to find clusters with random shapes and dimensions from a large set of points. The two main hyperparameters for the DBSCAN algorithm are $\varepsilon$ (the distance measure that will be used to locate the neighbourhood of any point) and $minPt$(the minimum number of points required for a region to be considered as a cluster).

## 6.8 Results

The results of the DBSCAN clustering method for a sample part is shown in Figure 6-15(e) and Figure 6-15(f). The performance of this clustering technique was measured using Equation 6-20.

Table 6-2 presents the per cluster accuracy of the clustering technique for different classes of the surface.

$$Per\ cluster\ accuracy = \frac{number\ of\ correctly\ predicted\ labels}{total\ predeictions} \qquad 6\text{-}20$$

Table 6-2.Results of per cluster accuracy

| | Concave | Convex | Normal |
|---|---|---|---|
| Per cluster accuracy | 81% | 87% | 88% |

Thus, it can be seen that the statistical techniques (used in 4.6) for defect segmentation and clustering shows promising results. However, the threshold distance and other input hyper-parameters need to be dynamically modified using experiments for the algorithm to provide robust results. This also requires a lot of domain knowledge. The following are the advantages of this approach:

a) Good accuracy of classification especially for normal and convex regions.
b) Very quick inference time (~60 µs).
c) No training data is required.

The drawbacks of this approach include:

a) Performs poorly on point clouds with varying densities. Since the point clouds acquired from the LDED-PF parts are obtained using different scanning speeds, the point cloud density can vary.
b) Does not perform well on non-planar geometries and thin-wall geometries.
c) Introducing new defect classes such as wavy will require a lot of domain knowledge.

d) Clustering hyper parameters need to be tuned for different geometries with different dimensions.

## 6.9 Classification of defects in LDED-PF using Semantic Segmentation

### 6.9.1 Using RandLANet for Segmentation of the point clouds

The clustering algorithm (presented in section 6.6) is used for automatic annotation of the point clouds to be processed by the 3D semantic segmentation network. The 3D semantic segmentation aims at finding the different defects in the 3D point clouds and classifying each defect into a pre-defined class.

Although the statistical outlier technique and clustering using the DBSCAN are very robust, they are highly dependent on the part size and point clouds, and the threshold distance needs to be adjusted for different sizes. Thus, it cannot be used as a robust and rapid technique for surface error identification in LDED-PF. Despite the limitation of deep learning for point cloud segmentation, RandLANet is capable of processing large point clouds directly in a short time using random sampling and local feature aggregation. The random down-sampling techniques used in RandLANet is a key enabler for processing large point clouds since it lowers the computational time and cost as compared to the other computationally extensive sampling techniques. While random sampling can discard the key information of the point clouds, especially the sparse points, the local feature aggregation technique can capture the complicated local features over smaller point sets. In each layer of RandLANet, the large point clouds are down sampled significantly using random sampling and it is still capable of retaining important features for segmentation. The process of random down sampling and local feature aggregation used in RandLANet is shown in Figure 6-16.

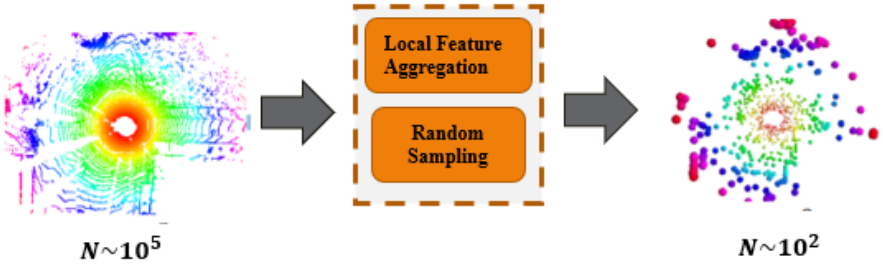


*Figure 6-16: Efficient random down sampling and local feature aggregation in RandLANet* [161]

The local feature aggregation includes the following units:

1- Local Spatial encoding (LocSE)

2- Attentive pooling

3- Dialated residual block

### 6.9.2 Local Spatial Encoding

The local spatial encoding unit embeds the x, y, and z coordinates of all neighbor points, therefor the corresponding point features are aware of their relative spatial positions.

The LocSE includes the following units:

#### 6.9.2.1 Finding Neighbor points

The neighbor points of the j[th] point are generated using K-nearest neighbors (KNN) algorithm based on the point-wise Euclidean distance.

#### 6.9.2.2 Relative Point Position Encoding

For each of the nearest K points $\{p_j^1, \dots, p_j^k, \dots, P_j^K\}$ of the center point $p_j$, the relative point position is explicitly encoded as Equation 6-21.

$$r_j^k = MLP(p_j \cup p_j^k \cup (p_j - p_j^k) \cup \|p_j - p_j^k\|) \quad 6\text{-}21$$

Where $p_j$ and $p_j^k$ are the coordinates of each point, $\| . \|$ is the Euclidean distance operator and $\cup$ is the concatenation operator. $r_j^k$ is encoded from redundant points and this helps the network to learn local features and acheive the required performance.

#### 6.9.2.3 Point Feature Augmentation

The relative point positions $r_j^k$, For every neighboring point $p_j^k$, are concatenated with its point features $f_j^k$ to find the feature vector $\widehat{\boldsymbol{f_j^k}}$.

### 6.9.3 Attentive Pooling

The attentive pooling MLP is used to find the aggregation of the set of neighboring point features $\widehat{\boldsymbol{F_J}}$. The typical min/max pooling used in [162] and [155] to integrate the neighbor features, results in the information being lost. Inspired by [163], the attentive pooling include the following steps:

#### *6.9.3.1 Computing Attention Scores*

A shared function $g()$ is developed to learn a attention score for every feature. $g()$ includes a shared MLP and softmax as shown in Equation 6-22.

$$s_i^k = g(\hat{f}_j^k . W) \quad 6\text{-}22$$

Where, W is the weights of the shared MLP and $\widehat{\boldsymbol{f}}_{\boldsymbol{j}}^{\boldsymbol{k}}$ is a local feature.

#### *6.9.3.2 Weighted Sum:*

The attention scores can be subsequently used as a soft mask to select the most important features. The weighed sum of the features is shown in Equation 6-23.

$$\tilde{f}_j = \sum_{k=1}^{K} (\hat{f}_j^k \cdot s_j^k) \qquad 6\text{-}23$$

where $\tilde{f}_j$ is the informative feature vector.

After the LocSE and Attentive pooling function, the original point cloud *P*, for its j[th] point, $p_j$, the geomatical features of is K nearest neighbors are aggregated to generate the feature vector $\tilde{f}_j$.

### 6.9.4 Dilated Residual Block

Large point clouds are down sampled substantially using random sampling; therefore, it is required to increase the receptive fields of every point to preserve the geometric details of the original point cloud. In general, the local feature aggregation, effectively reserves the complex geometrical features by explicitly considering neighbor geometries and increasing the receptive fields. The modules include only feed forward MLPs and therefore it is computationally efficient.

## 6.10 Implementation

The total number of 284 samples were built using random LDED-PF process parameters in the process window range specified in Table 3-2. Some of the built parts are shown in Figure 6-17. The scanning strategies for each sample were randomly selected from the scanning strategies templates to randomize the surface features.

The result of the 3D semantic segmentation for surface defect detection of LDED-PF parts is classified into three classes as presented in Figure 6-10.

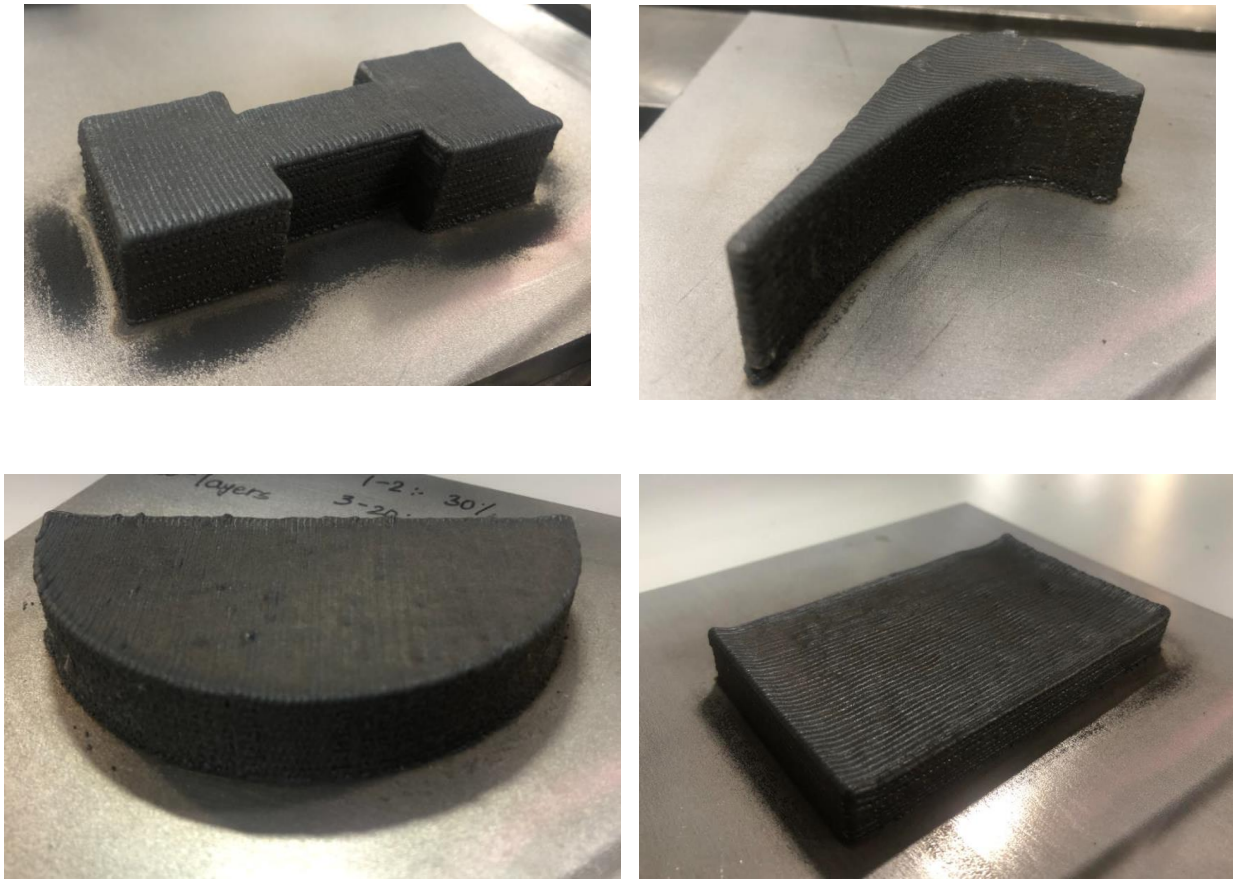

*Figure 6-17: Examples of LDED-PF parts printed for surface defect detection using deep learning*

The detailed architecture of the RandLA-Net (shown in Figure 6-18) is explained below.

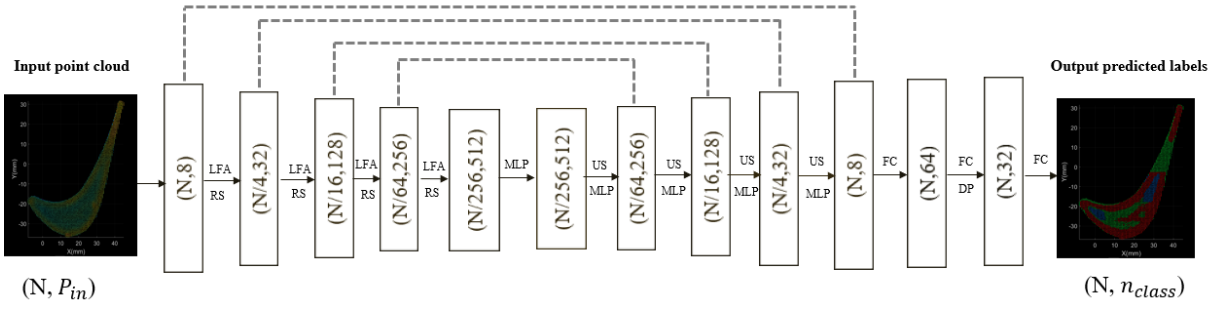


*Figure 6-18: The architecture of RandLA-Net: US: Up-sampling, (N,p): number of points and coordinates, LFA: Local Feature Aggregation, RS: Random Sampling, MLP: Multi-Layer-Perceptron, FC: Fully Connected Layer. DP: Dropout*

a) **Network Input**

The input is a point cloud acquired from the LDED-PF parts with the size of $N \times P_{in}$ , where $N$ is the number of points and $P_{in}$ is the 3D coordinates of each point. The Poisson disc sampling algorithm [164] is used to down sample the point cloud to the same size for inputting them into the network. Poisson disc sampling produces points that are tightly packed, but not closer to each other than a specified minimum distance. The minimum distance and the number of points is the input for this algorithm.

**b) Encoding Layers**

Four encoding layers are stacked to reduce the size of the point cloud and increase the per-point feature dimension. The point cloud is down sampled by ¼ after each layer and the per-point feature dimension are increased by 4 to retain more information. Each encoding layer includes a random sampling and local feature aggregation module.

**c) Decoding Layers**

Four decoding layers are stacked after the encoding layers. In each layer of the decoder, K nearest neighbors (KNN) is used to find the nearest neighbour point for each query point. The Euclidean distance is used for the KNN algorithm. The k nearest neighbors of a point is found using the Euclidean distance fusion as shown in Equation 6-24 [165].

$$dist((x_1, y_1, z_1), (x_2, y_2, z_2)) = \sqrt[2]{(x_1 - x_2)^2 + (y_1 - y_2)^2 + (z_1 - z_2)^2} \quad 6\text{-}24$$

For the given value of k by the user, the algorithm finds the k-nearest neighbors of the point and it assigns the class label to the input data with the largest probability.

After up sampling the point feature set, up sampled features are added by encoding layers. The MLP is then used for the concatenation of feature sets.

**d) Final Label Prediction**

The label of each point in the point cloud is calculated using shared fully connected layers. The dropout ratio of 0.5 is used.

**e) Network Output**

The output of the network is per point label with a size of N×$\boldsymbol{n_{class}}$, where $\boldsymbol{n_{class}}$, is the number of classes.

### 6.11 Implementation

The RandLANet architecture implementation in Open3D [166] based on the Tensorflow library was adopted for training and validation. A fixed number of points are sampled (~12,000 points) from each sample point cloud as input. All experiments are performed using NVIDIA RTX A5000 GPU.

Hyperparameters of the network (shown in Table 6-3) were selected by experimental and grid search techniques for optimization.

*Table 6-3:RandLANet Hyperparameters*

| RandLANet Hyperparameters | |
|---|---|
| Learning rate | 0.01 and decreased by 5% after each epoch |
| Gird size | 0.01 |
| # Epochs | 250 |
| Batch size | 32 |
| K nearest point for local encoding | 48 |

The performance of the network is evaluated using the k-fold cross-validation technique. In k-fold validation, the data is split evenly in k folds in which, k-1 folds are used for training of the data and one remaining fold is used for validation of the network performance. The **m**ean **i**ntersection **o**ver **u**nion (mIoU) and **o**verall **a**ccuracy (OA) are used as evaluation performance criteria. To calculate the mIoU, the bounding box for the ground truth label and predicted bounding box from the model are required.

The data obtained from scanning the experiment LDED-PF parts are split into the training and validation set by the ratio of 8:2.

The segmentation results fall into one of the following cases:

a) True Positive (TP): Model prediction is a positive sample point, and actual point label is a positive sample point as well.
b) False Positive (FP): Model prediction is a positive sample point, and the actual label is a negative sample.
c) True Negative (TN): Model predicts a negative sample point, and the actual label is a negative example as well.
d) False Negative (FN): Model predicts a negative sample point, but the actual label in a positive sample.

The IoU definition is the ratio of the intersection of the union of predicted value and actual value as shown in Equation 6-25 [167].

$$IoU = \frac{TP}{FP + FN + TP} \tag{6-25}$$

IoU is calculated based on the class and after each class calculates its IoU, the average IoU of all classes (mIoU*)* can be calculated.

Overall accuracy (OA) is defined as the percentage of the points that are classified correctly as shown in Equation 6-26.

$$OA = \frac{TP+TN}{TP+FP+TN+FN} \qquad 6\text{-}26$$

## 6.12 Results and Discussion

The average overall accuracy and average mIoU result of the 5-fold cross-validation of the RandLA-Net on the 3D point cloud dataset of the LDED-PF parts are shown in Figure 6-19 and Figure 6-20, respectively. The 5-fold cross-validation shuffles the dataset randomly and splits the data into k (5) groups. For each group, the group is divided into training and validation data and the model is fitted to the training data and tested on the validation data. Importantly, each observation in the data sample is assigned to an individual group, this means that each sample is given the opportunity to be used in the validation data set one time and to be used to train the model k-1(4) times.

The average overall accuracy and average mIoU accuracy values are shown in Table 6-4.

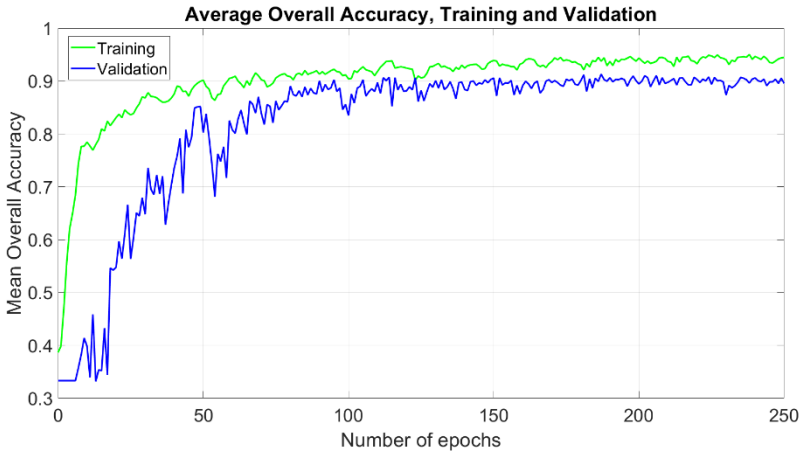


*Figure 6-19: Average overall accuracy for 5 folds*

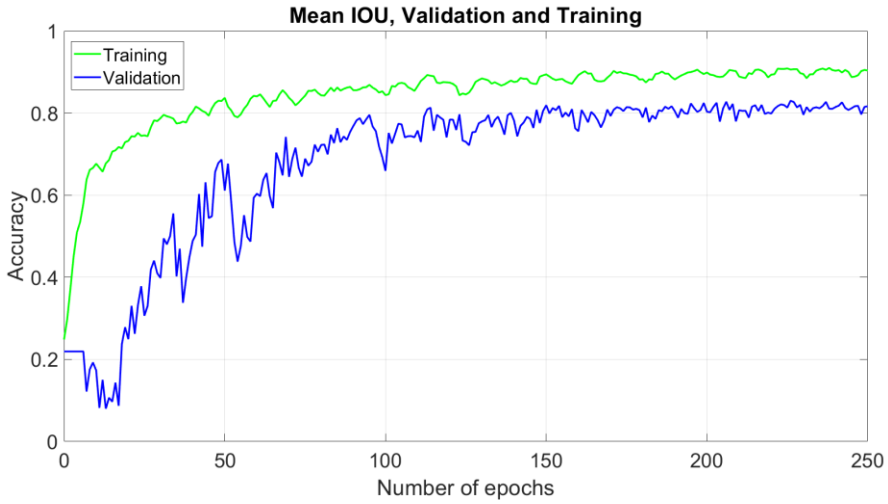


*Figure 6-20: Average mIoU accuracy for 5 folds*

*Table 6-4: Individual class overall average accuracy*

| **Class** | **Overall accuracy** | **IoU** |
|---|---|---|
| **Normal** | 95.1% | 89.4% |
| **Convex** | 89.6% | 81.4% |
| **Concave** | 88.3% | 79.3% |

The accuracy result shows good performance of the network overall on the normal and convex surfaces. However, the model struggles to detect the concave surface. Since the concave surfaces are mainly global features, they are the hardest to be detected by the DBSCAN clustering algorithm, and the RandLANet model. Comparing the point cloud data obtained from the surface of the LDED-PF part to the desired CAD geometry and increasing the training dataset will be the solutions to increase the convex and concave surface detection.

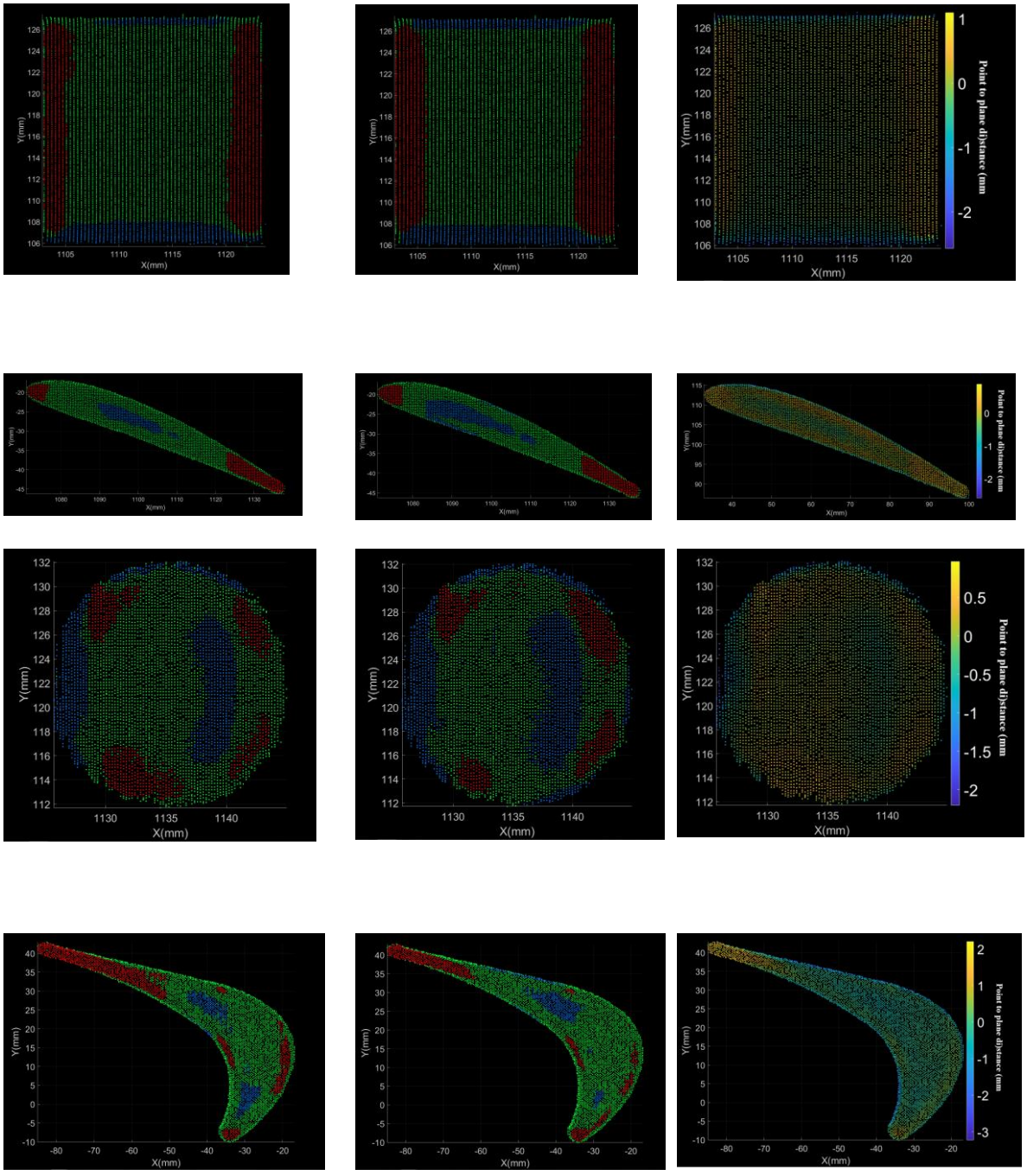


Ground Truth | RandLA-Net Model Predection | Original point cloud with the deviation from the reference plane

*Figure 6-21: Comparison of the Ground truth (GT) with the prediction of the RandLA-Net. Red: Convex surface, Blue: Concave surface, Green: Normal surface*

The qualitative result of the RandLA-Net on the validation split of our dataset is shown in Figure 6-21.

## 6.13 Summary

In the present work, a platform for deep-learning-based in-situ surface anomaly detection in LDED-PF was developed. The following conclusions can be drawn from the work:

1. The hand-eye calibration is implemented to calibrate the laser scanner sensor to reconstruct the surface of the printed geometries. Sub 0.5-millimetre accuracy is obtained for the hand-eye calibration, which can be effectively used for evaluating and addressing the surface quality issues during the LDED-PF process.
2. The output of the statistical analysis method is annotated and fed into a deep neural network called RandLA-Net and the average overall accuracy of 91.3% and mean IoU of 83.3% are achieved.
3. The methodology for defect detection can be used for immediately pausing the process in case of surface defect detection and preventing further quality deterioration leading to unpredictable failures.

The next chapter will discuss intermittent adaptive trajectory planning for geometric defect correction in robotic laser directed energy deposition-based additive manufacturing.

# 7 Intermittent Adaptive Trajectory Planning for Geometric Defect Correction in Robotic Laser Directed Energy Deposition-based Additive Manufacturing

## 7.1 Introduction

In this chapter, development of an adaptive tool path trajectory platform to correct the dimensional inaccuracies in-situ to build high-quality components using LDED-PF is carried out. The study deploys a laser line scanner to scan the part after the deposition of the definite number of layers followed by detection of concave, convex, and flat surfaces using deep learning. Further, the developed adaptive trajectory planning algorithm is deployed by using three different strategies to control material deposition on concave, convex, and flat surfaces. The material deposition is controlled by using adaptive scanning speed, and a combination of laser on-off and scanning speed. Subsequently, the built geometries are subjected to geometric, microstructure, and mechanical characterizations. It is observed that the deviation of the part was reduced by 30% , and 27.5% using adaptive scanning speed, and a combination of laser and scanning speed, respectively. The structures built using the three strategies show some micropores at isolated locations. However, solidification cracks are observed at few regions on samples built with laser control. The microstructure is mainly cellular under all conditions with a similar average microhardness of ~ 210 HV. The study provides an integrated and comprehensive approach for building high-quality components using LDED-PF with minimal dimensional deviation from the original CAD model.

## 7.2 Literature review

Closed-loop controller development for maintaining the dimensional accuracy has been an active area of research in recent years [168]. Process parameters such as scanning speed and laser power can be adjusted in real-time based on feedback from various sensors such as melt pool dimensions,

temperature, and surface tomography data. Fathi et al. implemented an analytical technique to estimate the melt pool depth in LDED-PF process offline [127]. Jeon et al. [169] used an integrated infrared camera and laser line scanner to estimate the melt pool depth in the LDED-PF process online. Toyserkani et al. developed a closed-loop control system based on the image acquired from multiple CCD cameras and PID controller to adjust the laser power to achieve the uniform clad height [170]. Ding et al. developed a PID controller to adjust the laser power to achieve the uniform melt pool dimension in different directions [171]. The performance of the controller was verified by building a corner wall, where the nozzle slows down in the corner and results in material build-up. A part was successfully built without the build-up using the PID controller.

Although real-time melt pool monitoring techniques improve the LDED-PF process significantly, there are many studies on this topic. Moreover, they provide real-time feedback for the correction of local anomalies without considering the global dimensional inaccuracies. In contrast to sensing techniques of the melt pool and real-time control of the process, recently some researchers used intermittent scanning and dimensional control of LDED-PF. Heralic et al. used a combination of laser line scanner and melt pool monitoring system to extract the geometry of deposited layers and dimensions of the melt pool at the corresponding location to use the data in machine learning applications to control the process [134]. Gardemnia et al. [172] developed an intermittent controller to adjust the scanning speed based on the local height of previous layers. The process was stopped after each layer, the top surface was scanned using a structural light scanner and the scanning speed was adjusted accordingly in the next deposition layer. The work was extended to the development of a more comprehensive controller to scan the part after a certain number of layers are deposited, adjust the working distance, and regenerate the toolpath for the rest of the part based on the acquired height from the scan [136]. Chen et al. [139]used a combination of

unsupervised and supervised learning to cluster the surface defects in LDED-PF parts. They achieved over 90% of accuracy to predict the cluster labels using k-nearest neighbours (KNN). Xu et al. [173] developed an in-situ trajectory generation technique to compensate for the surface defects by filling the underfill areas up to the maximum height. They used an in-house developed software tool chain to generate the repair toolpath and they reported the similar material properties between the samples built with and without this dimension correction strategy. Qin et al. [174]used a laser line scanner to scan the surface of the parts built using LDED-PF. Least square and d projection techniques were used to denoise and process the resulting point cloud. After the defects were identified, repair toolpath generation was generated to fill the underfill areas. Wilson et al. [63] developed a semi-automatic technique to repair the turbine blade tips using laser scanning and the difference Boolean operation between the desired geometry and the scan data (converted to STL files using triangulation). Kono et al. [175] presented an adaptive layer height control technique to control the standoff distance without considering the surface topography of the previously deposited layer.

Although the aforementioned dimension correction techniques improve the dimensional accuracy of built components, they suffer from various limitations. The techniques adopted in the literature do not consider the actual surface topography of the deposited layer during the correction. In addition, the techniques are based on CAD-based Boolean operation and reconstruction methods, which are computationally expensive. These techniques depend on the Boolean difference between the desired CAD data and the measured surface.

Thus, there is a need to develop an adaptive tool path trajectory platform to correct the dimensional inaccuracies in-situ to build high-quality components using LDED-PF. Therefore, in this research, deep learning-based surface defect detection is extended using efficient adaptive trajectory

planning strategies such as adaptive scanning speed control (ASSC), and a combination of laser on-off and scanning speed control (ASSLC) techniques to improve the dimensional accuracy of the LDED-PF parts in-situ. The developed parts are subjected to geometrical, density, microstructure, and mechanical property investigations.

## 7.3 Process parameters and specimen dimension

The process parameters used for the experiments are shown in Table 7-1. Argon is used as carrier gas and shielding gas to carry the powder to the deposition zone and avoid melt pool oxidation, respectively.

*Table 7-1: Process parameters for LDED-PF process*

| **Process parameter** | **Value** |
|---|---|
| Powder feed rate | 5 g/min |
| Laser Power | 700 Watts |
| Reference Scanning Speed | 10 mm/sec |
| Laser spot diameter | 1.2 mm |
| Shielding gas flow rate | 15 lpm |
| Carrier gas flow rate | 10 lpm |

Three different geometries were built to check the effect of the developed technique on the dimensional accuracy of the built parts. They are as follows:

(a) A cuboid with theoretical dimensions of 30 mm in length and width and a height of 24 mm

(b) A cylinder with a theoretical radius of 15 mm and height of 20 mm

(c) An I-beam shape (as shown in Figure 7-1) with a height of 12 mm

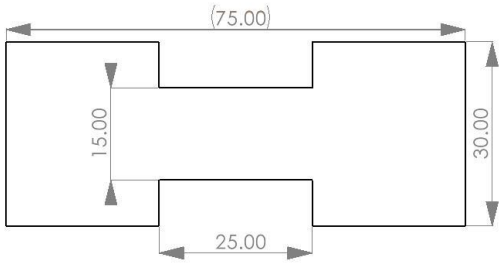


*Figure 7-1: Dimensions of the I-beam (All dimensions are in mm)*

## 7.4 In-situ surface defect detection

In this research, the deep learning-based method used in [176] is used to identify the surface anomalies in the LDED-PF parts. A laser profiler (Micro-Epsilon ScanCONTROL 2950-100/BL) is used to measure the surface topography of LDED-PF parts. The laser line scanner specification is shown in Table 7-2.

*Table 7-2: Specifications of the laser profiler*

| | |
|---|---|
| Model | ScanControl 2950-100 |
| Z-axis measuring range | 265 mm |
| X-axis measuring range | 143.5 mm |
| Measurement speed | 2,000 Hz |
| X-axis resolution | 1,280 points per profile |

The laser line scanner is rigidly mounted on the 6$^{th}$ axis of the robot arm. Hand-eye calibration is performed to obtain the accurate position of the laser profiler with respect to the faceplate of the robot's 6th axis. Once the position and orientation of the laser line scanner are found, the surface topography of the LDED parts can be obtained by transforming the point from the laser line profiler

coordinate system to the active user frame of the robot based on Equation 7-1, Where, $T_L^F$ is the $4 \times 4$ homogenous transformation matrix between the robot 6$^{th}$ axis frame to the deposition head frame (can be obtained from the robot controller), ), $T_S^F$ is the $4 \times 4$ homogenous transformation matrix between the scanner frame and the robot 6th axis frame (obtained using the technique describe in [9]) and $T_S^L$ is the transformation matrix between the laser scanner frame and the deposition head frame as shown in Figure 7-2(a).

$$T_S^F = T_L^F . T_S^L \quad 7\text{-}1$$

Once the $T_L^S$ is found, it is used to obtain the desired point cloud in the active tool frame (which is the deposition head frame) and active user frame (which is the work object frame) as shown in Figure 7-2(b) and Equation 7-2, where $P_S$ and $P_U$ are the scanned point in sensor and user frame coordinate system accordingly . $T_S^U$ is the transformation matrix between the user frame and the scanner frame which can be found as shown in Figure 7-2(b) and Equation 7-3, where $T_S^L$ is the transformation matrix between the scanner and deposition head frame, and $T_L^U$ is the transformation between the deposition head frame and user frame which can be obtained from the robot controller.

$$P_U = T_S^U . P_S \quad 7\text{-}2$$

$$T_S^U = T_L^U . T_S^L \quad 7\text{-}3$$

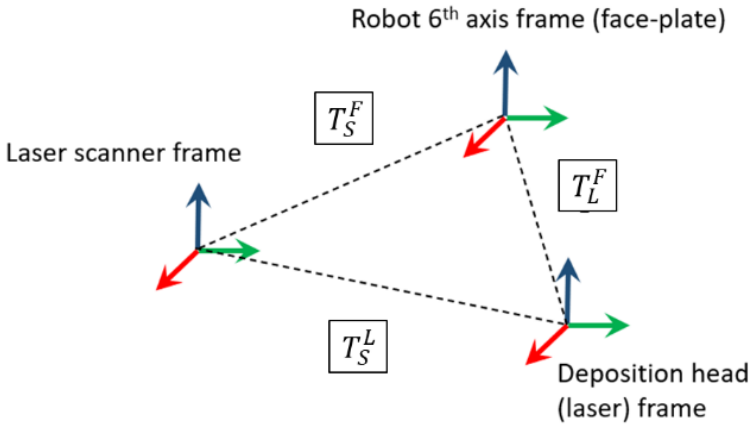


(a)

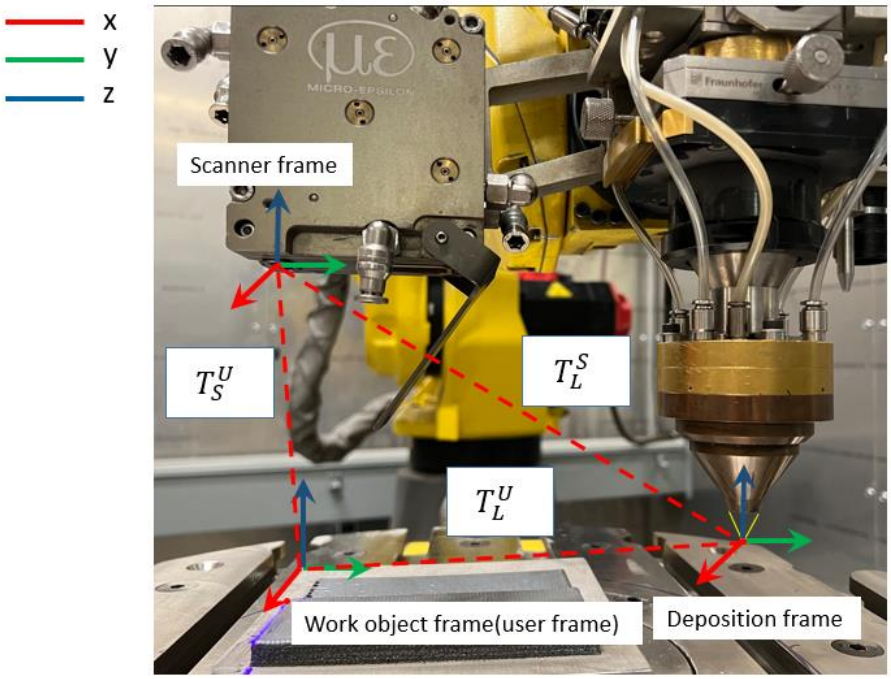


(b)

*Figure 7-2: (a)(b)Laser scanner frame, Deposition frame and Work object (user) frame*

Once the acquired point cloud is transformed into the active user frame of the robot, the target surface of the LDED part will be removed using the RANSAC algorithm, the noise and steep vertical wall are removed using the statistical outlier removal, and the points are clustered into a concave, convex and normal point using the deep learning [9].

## 7.5 Correction strategy

This section provides an overview of the correction process strategies. Two different strategies are employed to correct the geometrical defects. (1) Adaptive intermittent toolpath generation based on controlling the laser and scanning speed (2) Adaptive intermittent repair toolpath generation based on the augmented map.

The workflow of the correction strategies in both techniques is shown in Figure 7-3. First, the CAD model is decomposed to $i$ number of cycles. The toolpath is generated for each cycle. After the deposition of each cycle, the deposition process is stopped, and the laser line profiler scans the top surface of the deposited part. The surface defects and anomalies are detected using an in-house developed software platform for surface defect detection of parts built using LDED-PF [9]. Once the defect boundaries are detected, an augmented map is generated to label the defect regions and then the next layer toolpath will be generated in-situ and the adaptive scanning speed and laser actuations will be employed based on the real-time robot's coordinates and their location will be labelled based on the generated map. Once the robot coordinate is labelled, based on the selected strategy, either the scanning speed will be changed to compensate for the error, or the laser will be turned off in the convex regions to stop the overgrowth. This process continues until the target surface meets the smoothness criteria of:

$$h' = h^*(P_{z\_max} - P_{z\_min}) \quad 7\text{-}4$$

ere, $P_{z\_max}$ and $P_{z\_min}$ are the maximum and minimum height of the target surface and $h^*$ is a coefficient that is selected based on the dimension and material. For SS316, $h^*$ of $1mm$ resulted in acceptable surface conditions.

Once the dimensionally acceptable surface target is obtained, the correction loop ends. It is possible that the deposition height after the deposition of layers ($H^*$) exceeds the theoretically predicted height ($H$). In this case, the number of layers in the consecutive group will be recalculated based on Equation 7-5, where $H$ is the desired height of the next deposition group, $H^*$ is the height of the current deposited group, and $h$ is the layer thickness.

$$n = \frac{H - H^*}{h} \quad 7\text{-}5$$

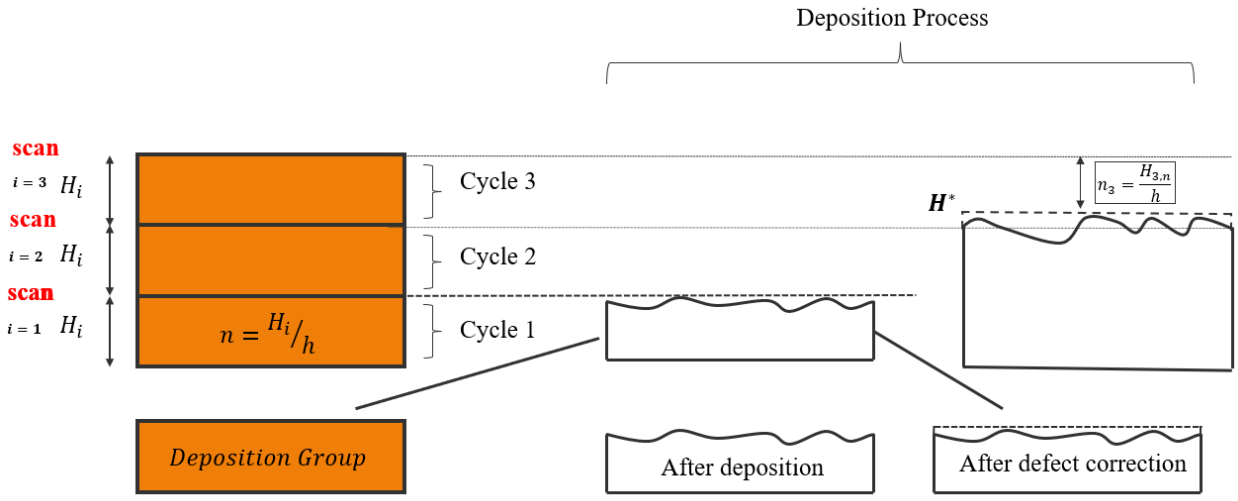


*Figure 7-3: The schematic of the correction process*

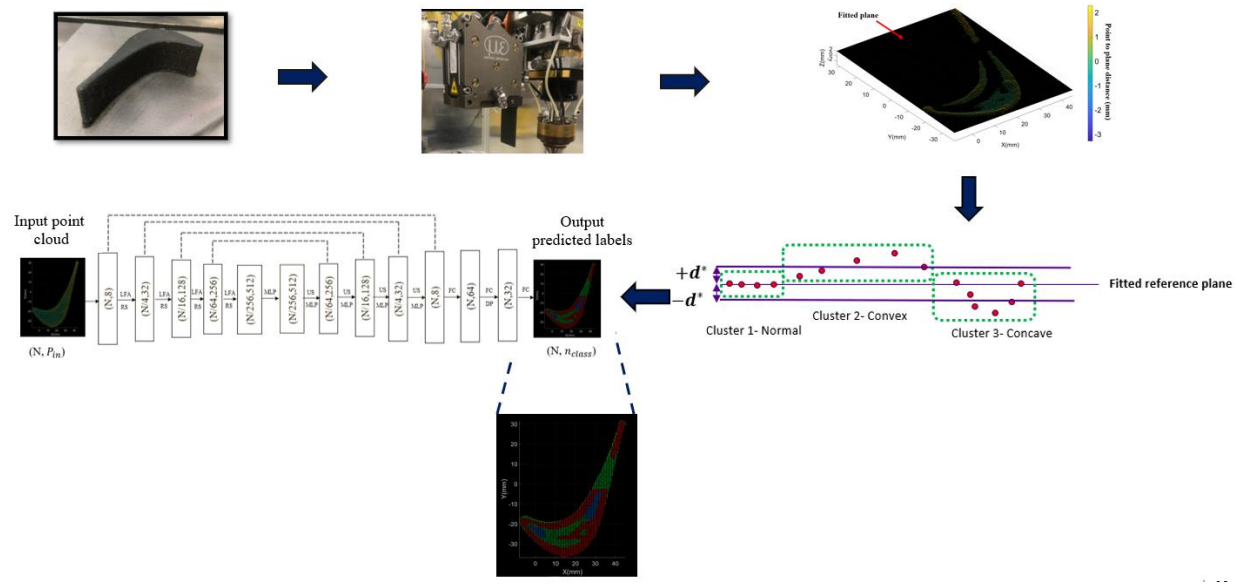


*Figure 7-4: Surface defect detection process using deep learning*

## 7.6 Point cloud processing and repair toolpath generation

In this section, the defect boundary extraction and repair toolpath generation algorithms are presented. The techniques to develop the repair toolpath are one of the main contributions of this research.

## 7.7 Defect Boundary extraction

Once the defect regions are identified, the boundary of each defect region must be identified. Many boundary detection algorithms can be employed. Among them, ConvexHull [177] is the most widely used algorithm. The convex hull of a typical convex region is shown in Figure 7-5(a). It can be noticed that the convex hull of the convex region is not an accurate representation of the convex region. Therefore, the ConcaveHull algorithm is explored [178]. ConcaveHull algorithm is a specific version of the ConvexHull algorithm based on Jarvis March's gift wrapping algorithm for ConvexHull [179]. In this research, a novel concave-hull algorithm based on the circumference circle of the boundary triangle is developed. Firstly, the Delaunay triangulation algorithm was

applied to the acquired point clouds to find the triangle meshes [180]. After the triangle meshes are obtained, the radius of the triangle circumcircle is found as shown in Figure 7-6. A threshold value is then used to determine if the triangle edges are boundary edges. If both neighbouring triangles are in shape, the edges are not the boundary edge.

The radius of the circumcircle can be obtained using Equation 7-6, where a, b and c are the edges of the triangle and $A_t$ is the area of the triangle.

$$R = \frac{abc}{4A_t} \tag{7-6}$$

The generated contour using different threshold values is shown in Figure 7-5(b)-(d). It is noticed that the selection of the threshold value is very subjective. Therefore, a technique based on Minimum Spanning Tree (MST) [181] is developed to calculate the threshold value automatically. Based on the definition of MST, the MST of each concave and convex region is calculated, and the threshold value is calculated as shown in Equation 7-7, where $h_n$is shown in Equation *7-8*, where $l_n$ is the length of MST of the point cloud and *n* is the number of points in the point cloud. The robustness of $\alpha$ selection based on the length of the MST is validated experimentally using extracted boundaries for different geometries with varied dimensions. On the contrary, the selection of constant $\alpha$ results in inaccurate boundary estimation for different geometries with various dimensions.

$$\alpha = \frac{1}{h_n} \tag{7-7}$$

$$h_n = \sqrt{\frac{l_n}{n}} \tag{7-8}$$

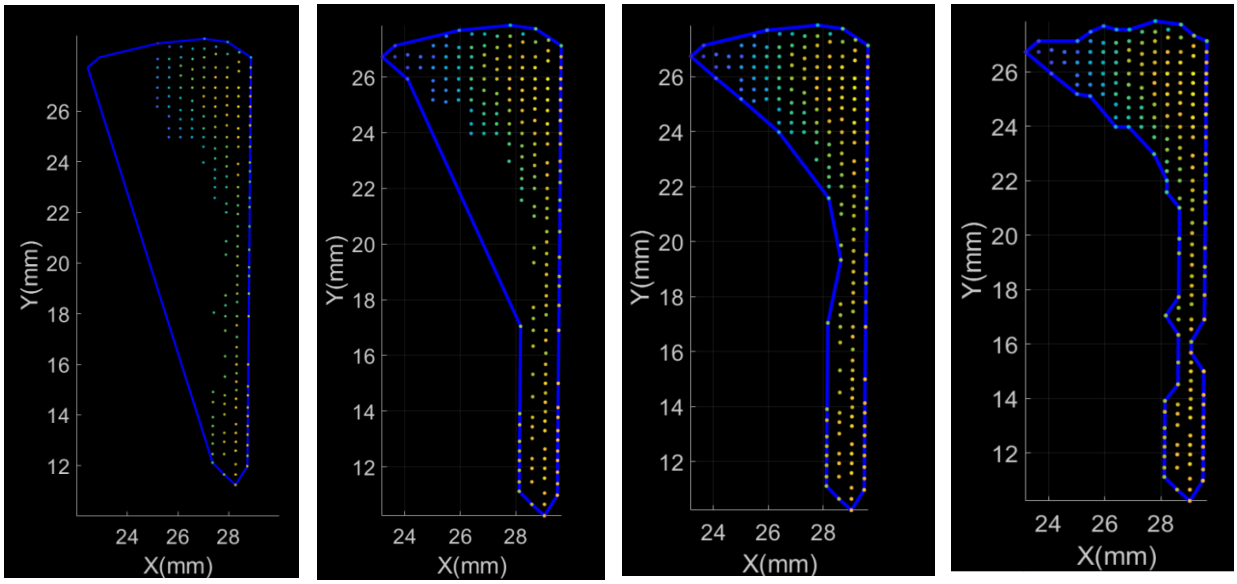


(a) (b) (c) (d)

*Figure 7-5: Resulting boundary using (a) ConvexHull algorithm, ConcaveHull with the alpha value of (b)20, (c)10, (d)1.5*

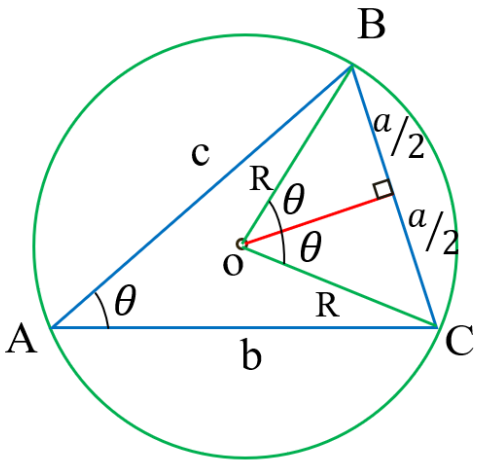


*Figure 7-6. Circumcircle of the triangle*

## 7.8 Binary map generation

Once the contours of defect regions are obtained, an iterative ray casting algorithm is developed to generate the binary map of the deposited layer [182]. Firstly, a grid of size with the resolution of 0.3 mm in both x and y directions (100×100 for a cube with length of 30 mm) is generated as shown in Figure 7-7(a). Secondly, for each pixel in the grid, a label is assigned based on the location of the pixel in respect to the convex and concave boundaries. For example, as shown in Figure 7-7(a), for $i = 3, j = 3, P_{i,j}$ is inside the defect boundary, therefor, a defect label (depending on the boundary defect type) will be assigned to $(i, j)$ pixel. The algorithm used to decide whether the point is inside or outside of the defect polygons is shown in Figure 7-8.

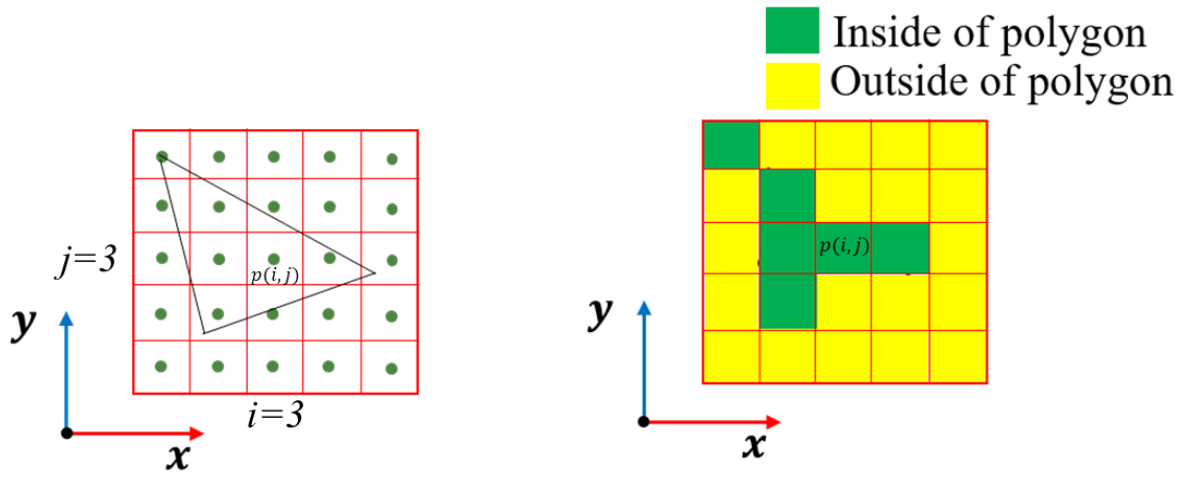


(a) (b)

*Figure 7-7:(a) Ray tracing to determine the position of points in the layer, (b) developed map*

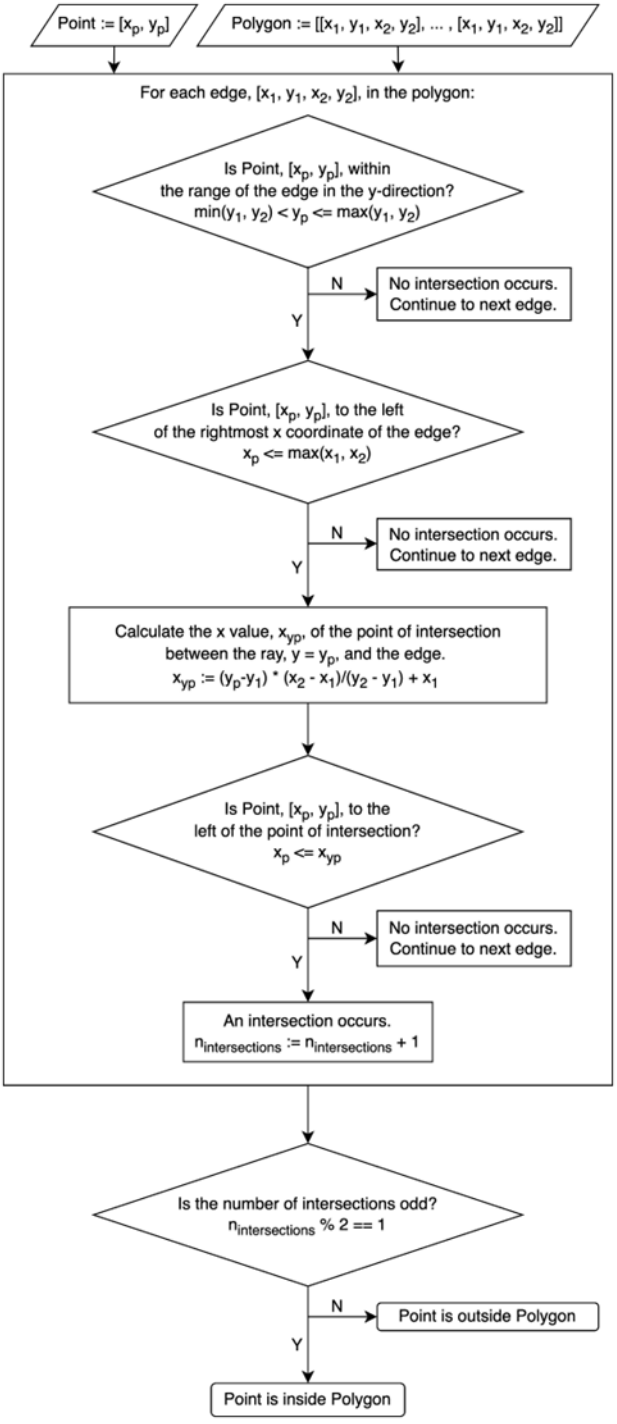


*Figure 7-8: Flowchart of ray tracing algorithm*

The result of the binary map generation process is shown in Figure 7-7(b). The acquired map will be used to control the trajectory of the robot in the consecutive layers to compensate for geometric deviations.

## 7.9 Augmented Map generation

Once the contour of the defect regions is identified using the map generation process, a more accurate map, including the local height of each pixel in the grid is required to achieve a better level of control. In this section, the process of augmented map generation is presented. The flowchart for generating an augmented map is presented in Figure 7-9 (a). The generated augmented map is shown in Figure 7-9 (b).

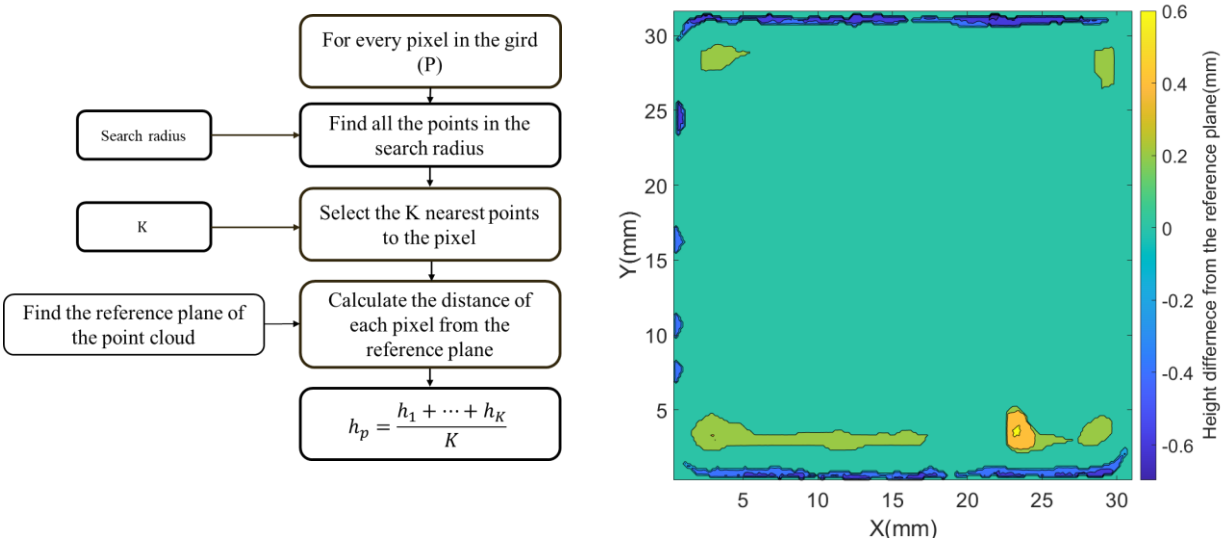


(a) (b)

*Figure 7-9:(a) Flowchart of augmented map generation algorithm, (b) An example of generated augmented map*

Firstly, for each pixel in the grid, the radius search is performed to find all the points within the specified radius from the pixel.After radius searchthe k-nearest points to the pixel center points are selected. Once all the k-nearest points to the pixel center point are found, a plane is fitted to the

point cloud using TLS method. After finding the plane, the equation of the plane can be written as Equation 7-9. Once the palne is found, the distance of k-nearest point to the pixel center point P ($P_{x_i}, P_{y_i}, P_{z_i}$) to the reference palne is found using Equation 7-10, where $h_n$ is the calculated Euclidean distace from each point to the fitted reference plane.

$$ax + by + cz + d = 0 \tag{7-9}$$

$$h_n = \frac{aP_{x_n} + bP_{yn} + cP_{zn}}{\sqrt{a^2 + b^2 + c^2}} \tag{7-10}$$

Once $h_n$ is found for each k-nearest point to the pixel center point, the average distance of the pixel from the fitted reference palne ($h_P$) can be estimated using Equation 7-11.

$$h_P = \frac{h_1 + h_2 + \cdots + h_k}{k} \tag{7-11}$$

### 7.10 Adaptive laser and speed control (ASSLC)

In ASSLC, once the map is generated and the correction layer trajectory is loaded into the robot. Once the robot position hits the convex boundaries, the laser will be turned off as shown in Figure 7-10. Once the robot hits the concave regions, the scanning speed will be decreased according to the augmented map output. The scanning speed in the normal region ($v_{normal}$) remains constant and in the concave region ($v_{concave,i}$) will be adjusted based on Equation 7-12:

$$v_{concave,i} = v_{concave\_set} + c_{cv} h_{pi} \tag{7-12}$$

Where, $v_{concave\_set}$ is the set point scanning speed for the concave region, c is the constant value obtained by experiments and $h_{pi}$ is the output of the augmented map at the specified location. For the process parameters in this study, $v_{concave\_set}$ is set to 5 mm/sec, and the constant value of $c_{cv}$

is defined as shown in Equation *7-13*, where $l_{v\_min}$ is a experimental based parameter defined by user, corresponding to the maximum deviation for which minimum speed is to be applied as shown in Figure 7-12.

$$c_{cv} = \frac{v_{normal} - v_{concave\_set}}{l_{v\_min}} \qquad 7\text{-}13$$

If the scanning speed deviation for a certain deviation is excessive, the growth of the part might change more than requirement to reach the target height. , Therefore, the minimum scanning speed is defined to avoid over deposition in concave regions as shown in Equation 7-14.

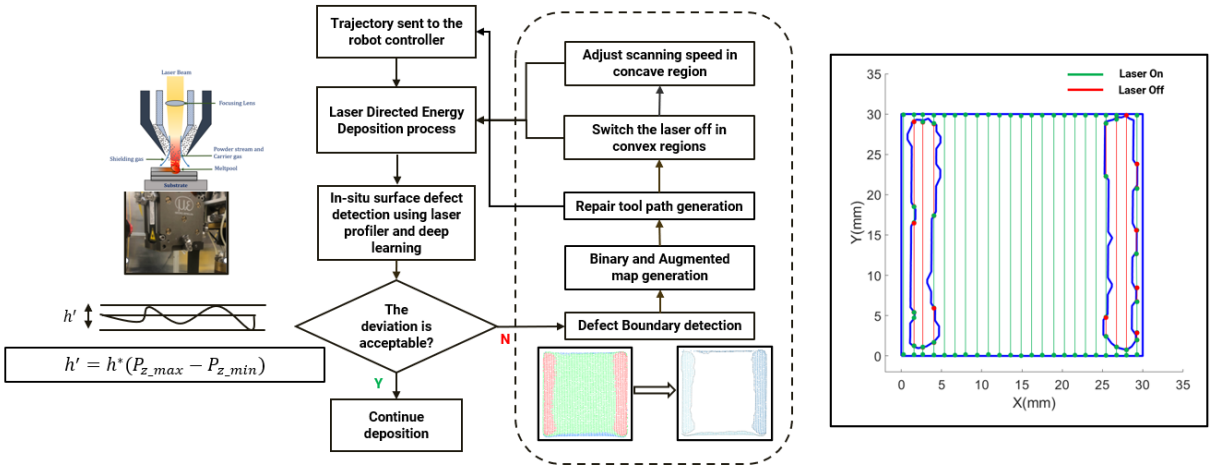


*Figure 7-10: Flowchart of the correction algorithm using laser and scanning speed control*

$$v_{concave,i} = v_{min}, if\ v_{concave,i} < v_{min} \qquad 7\text{-}14$$

### 7.10.1 Adaptive scanning speed control (ASSC)

In this technique, once the map and augmented map are generated, the correction layer trajectory will be generated and sent to the robot controller. Once the robot hits the convex and concave regions the scanning speed will be adjusted based on which region the robot is depositing in and

the value of the augmented map at that exact position. The flowchart of the correction process adopted in ASSC is shown in Figure 7-11.

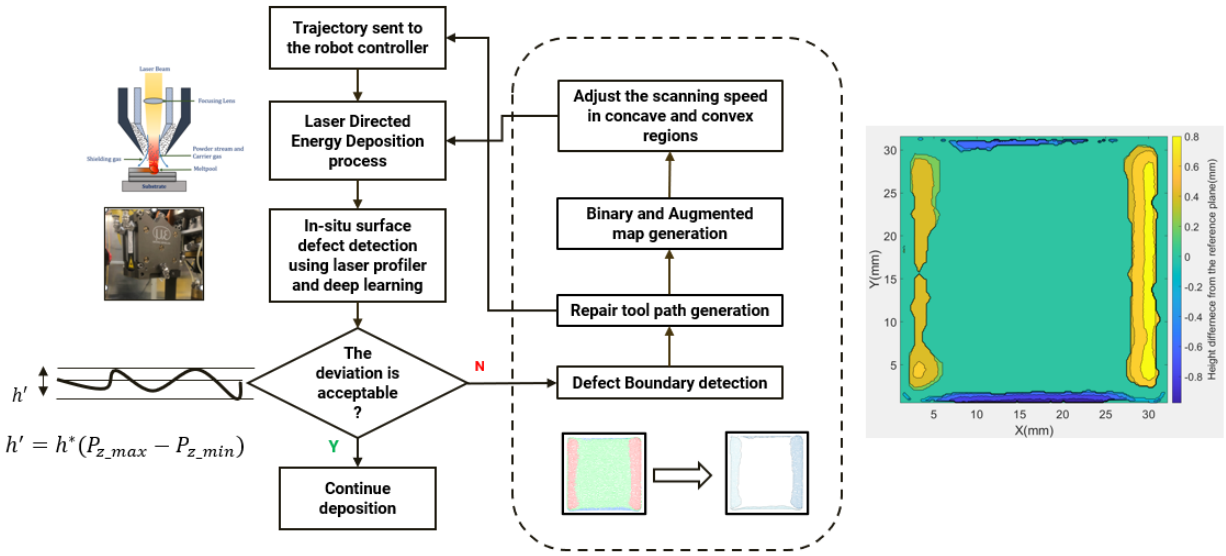


*Figure 7-11: Flowchart of the algorithm for adaptive scanning speed*

Since the binary map and augmented map are both obtained, different setpoint values can be used for concave and convex regions as shown in Figure 7-12. Different set point values are used for normal, convex, and concave regions. These values depend on the layer height and other process parameters. The maximum deviation in the positive direction determines the maximum scanning speed. The slope of each correction curve is determined using the maximum deviation from the reference plane in both positive and negative directions, and $v_{max}$ and $v_{min}$ respectively. If the speed change is more than is required to reach the target height, it might adversely affect the process, therefor $v_{max}$ and $v_{min}$ are applied to ensure that process stays in the stable region. The scanning speed remains unchanged if the deviation from the reference plane is within $\pm l/2$, where $l$ is the layer height. The velocity of each point in the convex region $(v_{convex,i})$ can be obtained

using Equation 7-15, where $c_{cx}$ is the experimental user-defined parameter obtained using Equation 7-16. The maximum allowable scanning speed is obtained using experiments and if the outcome of Equation 7-15 is greater than the maximum allowable scanning speed, it will be set as the maximum scanning speed as shown in Equation 7-17.

$$v_{convex,i} = v_{convex\_set} + c_{cx} h_{pi} \quad 7\text{-}15$$

$$c_{cx} = \frac{v_{convex\_set} - v_{normal}}{l_{v\_max}} \quad 7\text{-}16$$

$$v_{convex,i} = v_{max}, if\ v_{max,i} > v_{max} \quad 7\text{-}17$$

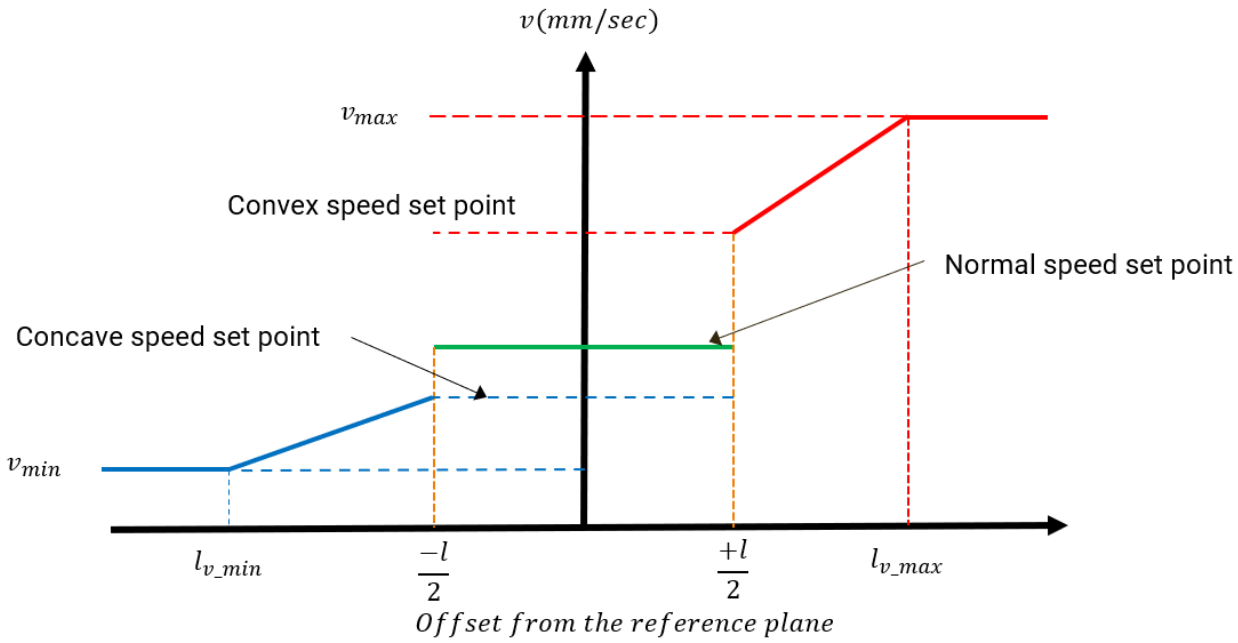


*Figure 7-12: Schematics of scanning speed control based on the points offset from the reference plane*

### 7.10.2 Correction Toolpath generation

Once the layer map and augmented map are generated, the correction layer trajectory at the desired height is generated using ModuleWorks (MW)'s template CAM software. Once the correction layer trajectory is generated, it is loaded into the robot controller using TCP/IP communication and the correction process starts. Once the trajectory is executed, the TCP position is acquired each 8 msec and it is checked versus the generated map and augmented map and the scanning speed or laser status is updated according to the selected correction strategy. The input to the trajectory planning kernel is the desired height at which the correction layer is required, stepover, raster orientation, and scanning strategy as shown in Figure 7-13. The stepover is kept equal to the original trajectory and the raster orientation is selected based on the latest deposition layer strategy.

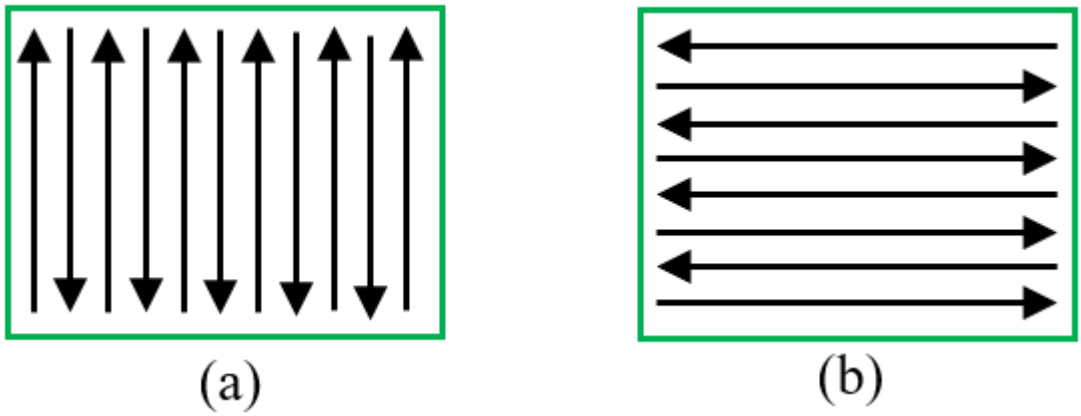


*Figure 7-13: Correction trajectory (a) Raster orientation of 90°, (b) Raster orientation of 0°*

## 7.11 Results and discussion

### 7.11.1 Dimensional accuracy

A series of experiments were conducted to evaluate the performance of the developed technique to increase the dimensional accuracy of the LDED-PF parts. For each part, after each cycle, the deposition is paused, the surface topography of the previously deposited cycles is acquired using the laser line scanner, the surface defects are identified, if the peak to valley difference is more than a layer height, the correction toolpath is generated, and the correction process continues until the peak to valley distance is less than a nominal layer height. The number of cycles and number of layers in each cycle for the three geometries are shown in Table 7-3.

*Table 7-3: Cycle parameters for the three geometries*

| Part | Number of cycles | Number of layers in each cycle |
|---|---|---|
| Cube | 3 | 8 |
| Cylinder | 4 | 5 |
| I-beam | 2 | 6 |

The toolpath for each part was not optimized in this research, therefore, a significant deviation in dimensional accuracy was expected as shown in Figure 7-14(a). The dimensional deviations in this component are mainly due to acceleration and deceleration of the robotic system at the end of each line segment, which increases the laser interaction time with the powder and causes local over-growth regions in the turns and corners. These deviations have a compound effect and will be accumulated during each successive layer, therefore after a few layers, a saddle shape is created. Figure 7-14(b) and Figure 7-14(c) show the part built using ASSLC and ASSC. respectively. Both

techniques resulted in enhancement of the dimensional accuracy, but the surface topography and volumes measurement studies show that the deployment of only ASSC results in better dimensional accuracy.

*Table 7-4: Volume comparison of the built parts by different strategies*

| Strategy | Volume ($mm^3$) | Difference from original ($mm^3$) |
|---|---|---|
| Original | 21,600 | 0 |
| Without dimension correction | 15,018 | -6,582 |
| With Dimension correction; Laser and adaptive scanning speed | 20,980 | -620 |
| With Dimension Correction; Adaptive scanning speed | 21,720 | +120 |

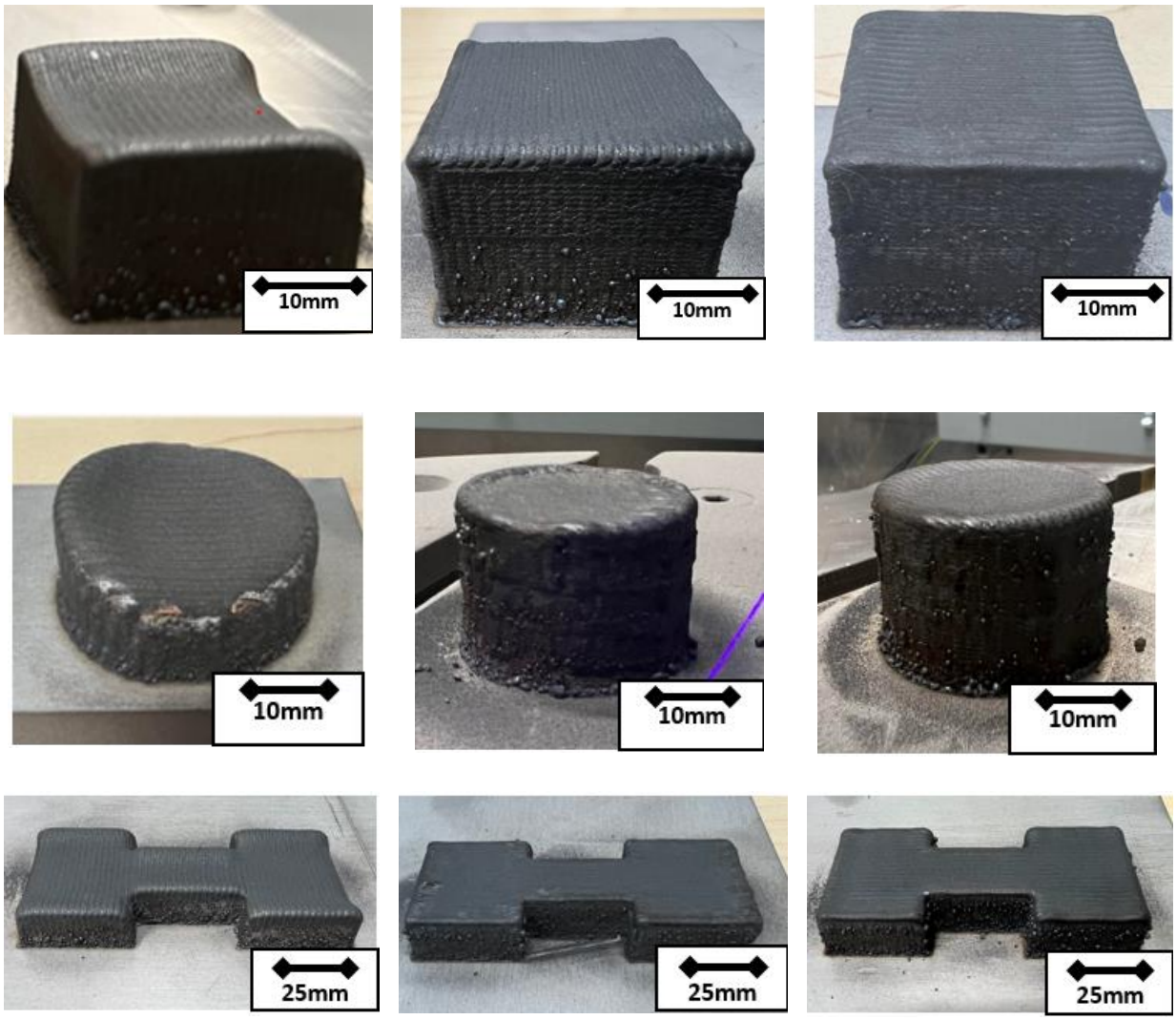


(a) (b) (c)

*Figure 7-14: Comparison of built LDED-PF parts (a) without control (b) ASSLC (c) ASSC*

The theoretical volume of the cuboid, volume correction after implementing techniques and the volume before applying any correction technique is shown in Table 7-4. The volume calculation is performed using the integral of the grid points obtained in the augmented map generation process over the volume. As shown in Table 7-4, the dimension correction using ASSC results in less error than the nominal desired volume. The positive direction of the built part can be justified by the near-net shape nature of the LDED-PF process

### 7.11.2 Geometrical analysis

The cross-section extracted from the acquired point clouds in the XZ direction for the cuboid built without correction is shown in Figure 7-15(a). Figure 7-15(b) shows the final layer of each cycle just before the deposition of correction layers, and Figure 7-15(c) shows the cross-section extracted from the point clouds in XZ direction after correction layer deposition. The height deviation from the desired height in Figure 7-15(a) is corrected by adding subsequent correcting layers in Figure 7-15(b). Figure 7-15(c) shows the flat surface acquired after the adaptive scanning speed is used to correct the local defect and surface unevenness in Figure 7-15(b).

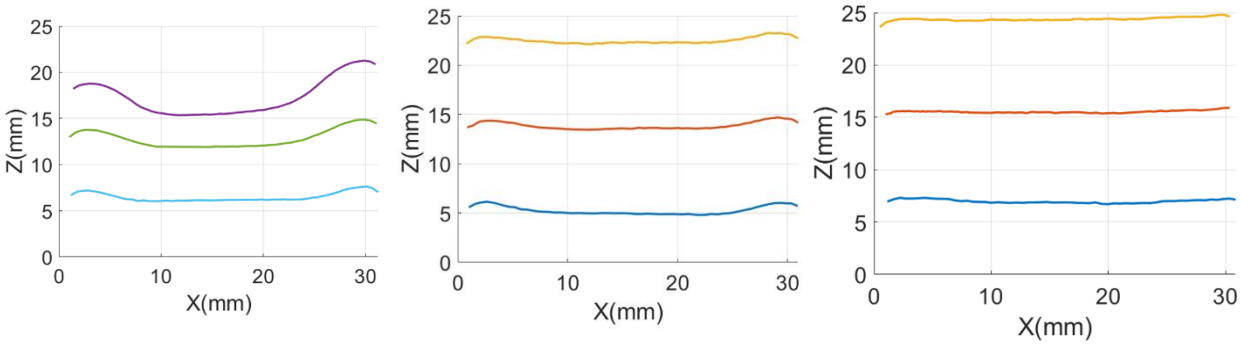


(a) (b) (c)

*Figure 7-15: Cross section extracted from the point cloud in XZ plane of the cuboid (a): Without correction, (b) before correction layers are deposited, (c) after deposition of correction layers*

The results of correction process for every geometry using different correction techniques are shown in Figure 7-16.

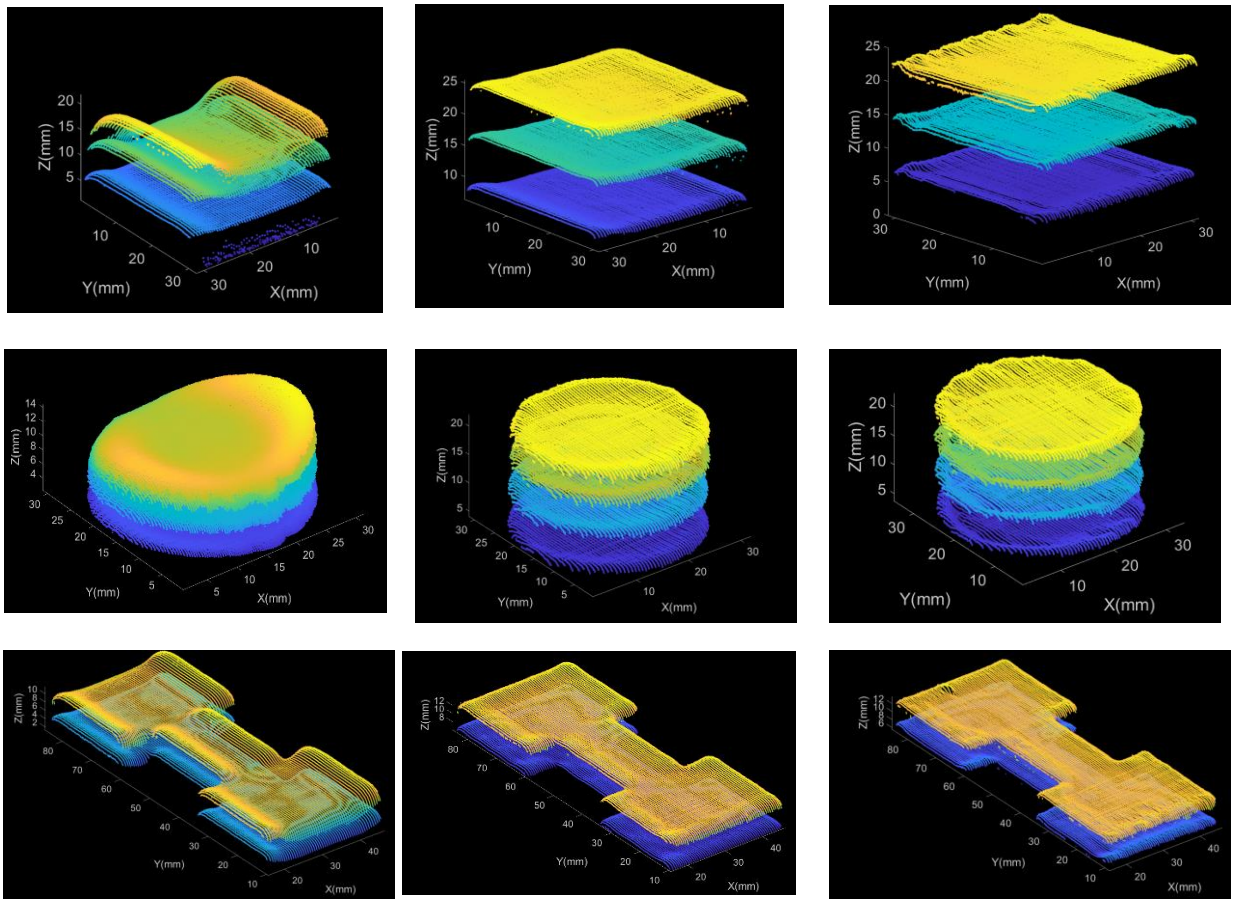


(a) (b) (c)

*Figure 7-16: The results of correction processes on final geometry of the components*

The resulting process map for each correction layer for the cuboid, cylinder and I-beam are shown in Figure 7-17, Figure 7-18 and Figure 7-19 respectively.

**Before correction**

**After the first correction layer**

**After the second correction layer**

**After the third correction layer**

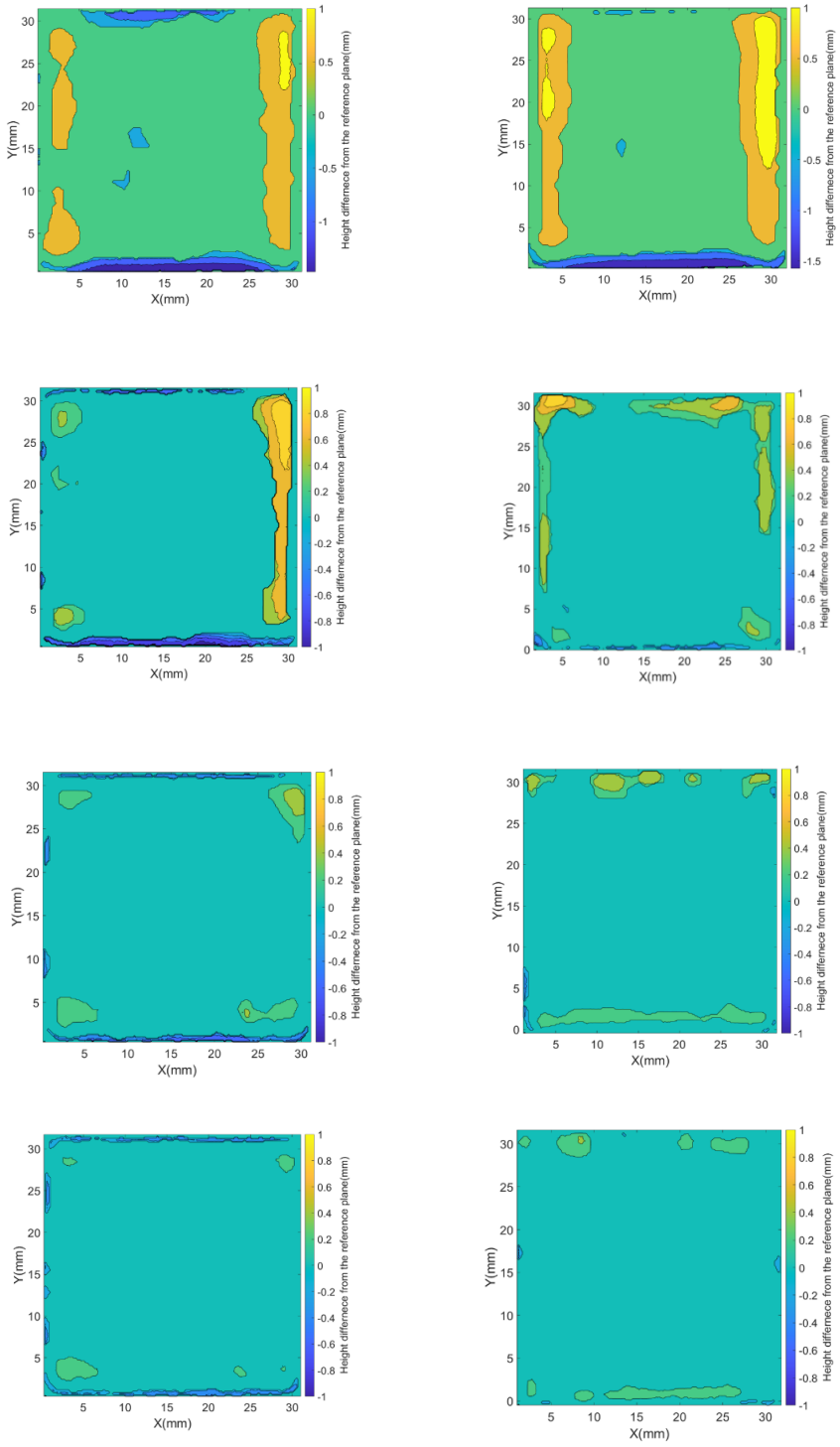


(a) (b)

*Figure 7-17: Correction progress in one correction group using (a) ASSC (b) ASSLC*

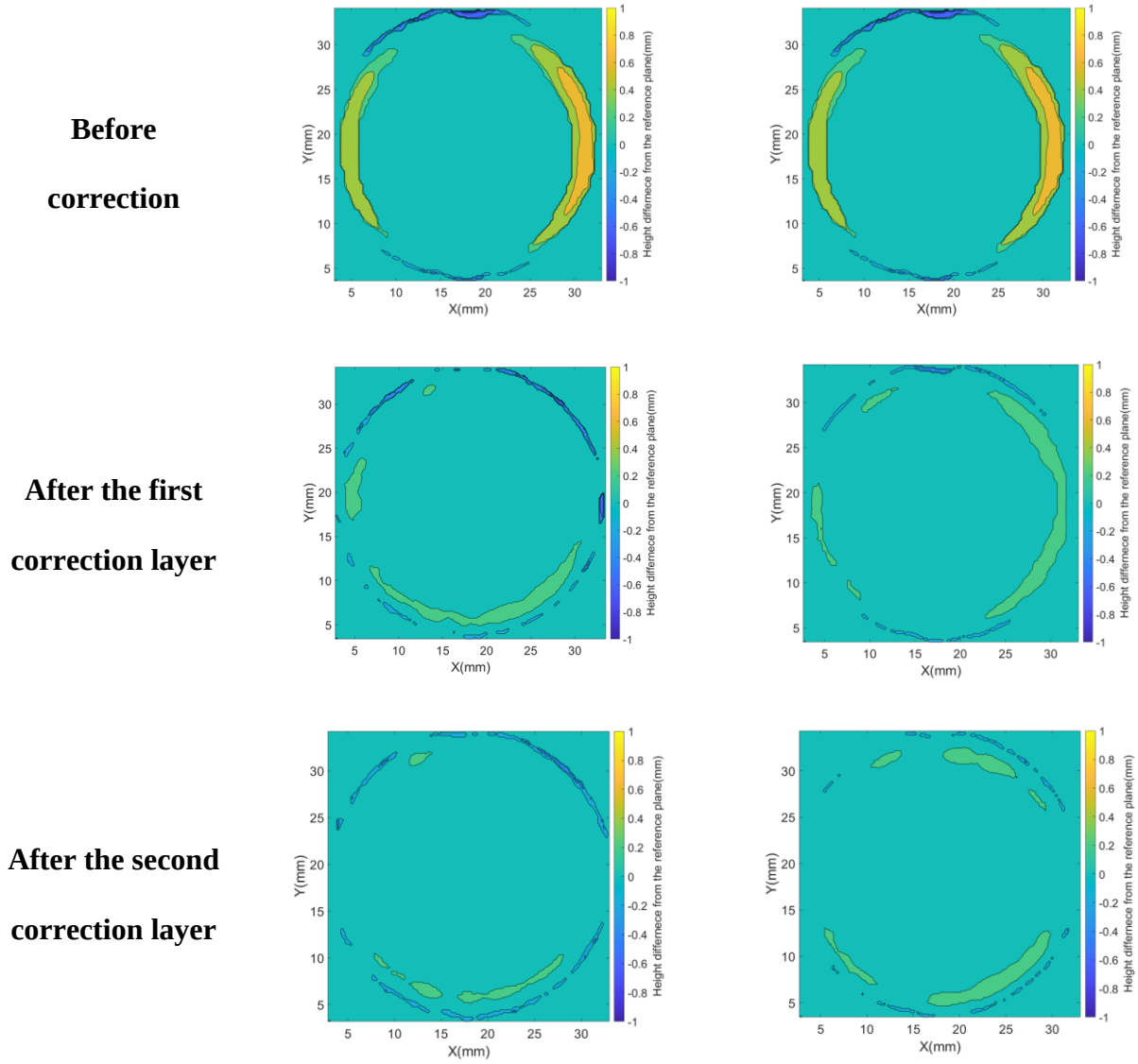


*Figure 7-18: Correction progress in one correction group using (a) ASSC (b) ASSLC*

**Before correction**

**After the first correction layer**

**After the second correction layer**

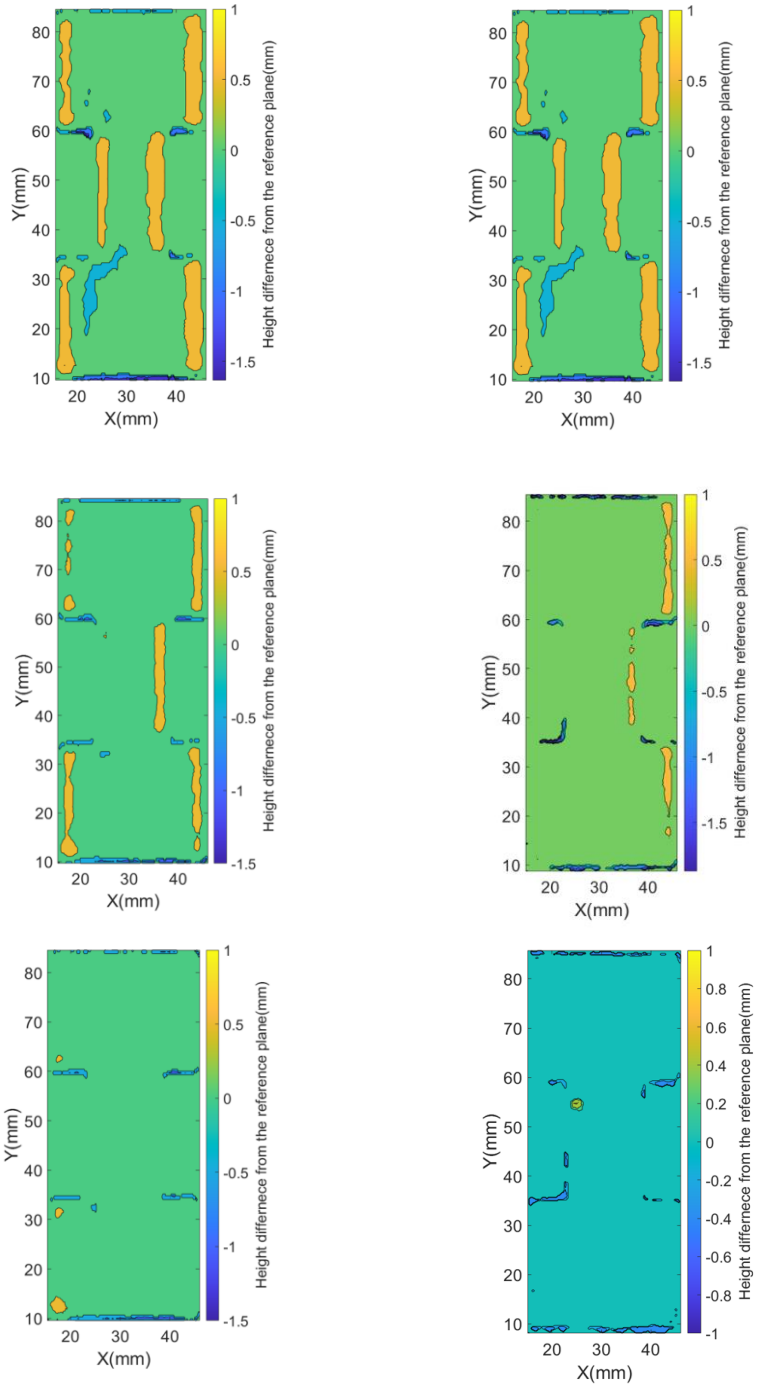


(a) (b)

*Figure 7-19: Correction progress in one correction group using (a) ASSC (b) ASSLC*

### 7.11.3 Melt-pool

The melt-pool morphology of the built components in the XZ plane with and without correction techniques was investigated using optical microscopy. Figure 7-20(a), (b) and (c) shows the melt-pool images of the cross-section without correction, correction using controlling laser and scanning speed, and correction using scanning speed control, respectively. The layer boundaries are highlighted using red dotted lines. The curvature of the melt-pool at the corner is clearly visible under all conditions which are typically seen in LDED due to the effect of acceleration/ deceleration effects from the deposition strategies. The deposition starts and stops at the edges resulting in a slightly higher deposition at the edges. In addition, the over deposition at the edges can result in reduced stand-off distance at the edges, resulting in higher laser energy density. This leads to higher catchment and relatively higher deposition at the edges. This results in the melt-pool curvature from the edges to the central region of the part. A comparison between samples built using different control schemes indicates that the melt-pool curvature is higher in the samples built without correction. This is mainly due to the continuous accumulation of heat during deposition and the accumulation of the geometrical errors from each layer to the final built part. However, it is observed that the curvature of the melt-pool is reduced significantly with the application of correction strategies. This is mainly due to the controlled heat input used with the control schemes which aids to regulate the accumulation of geometrical error. This is in line with the observations from the geometrical analysis presented in the previous section.

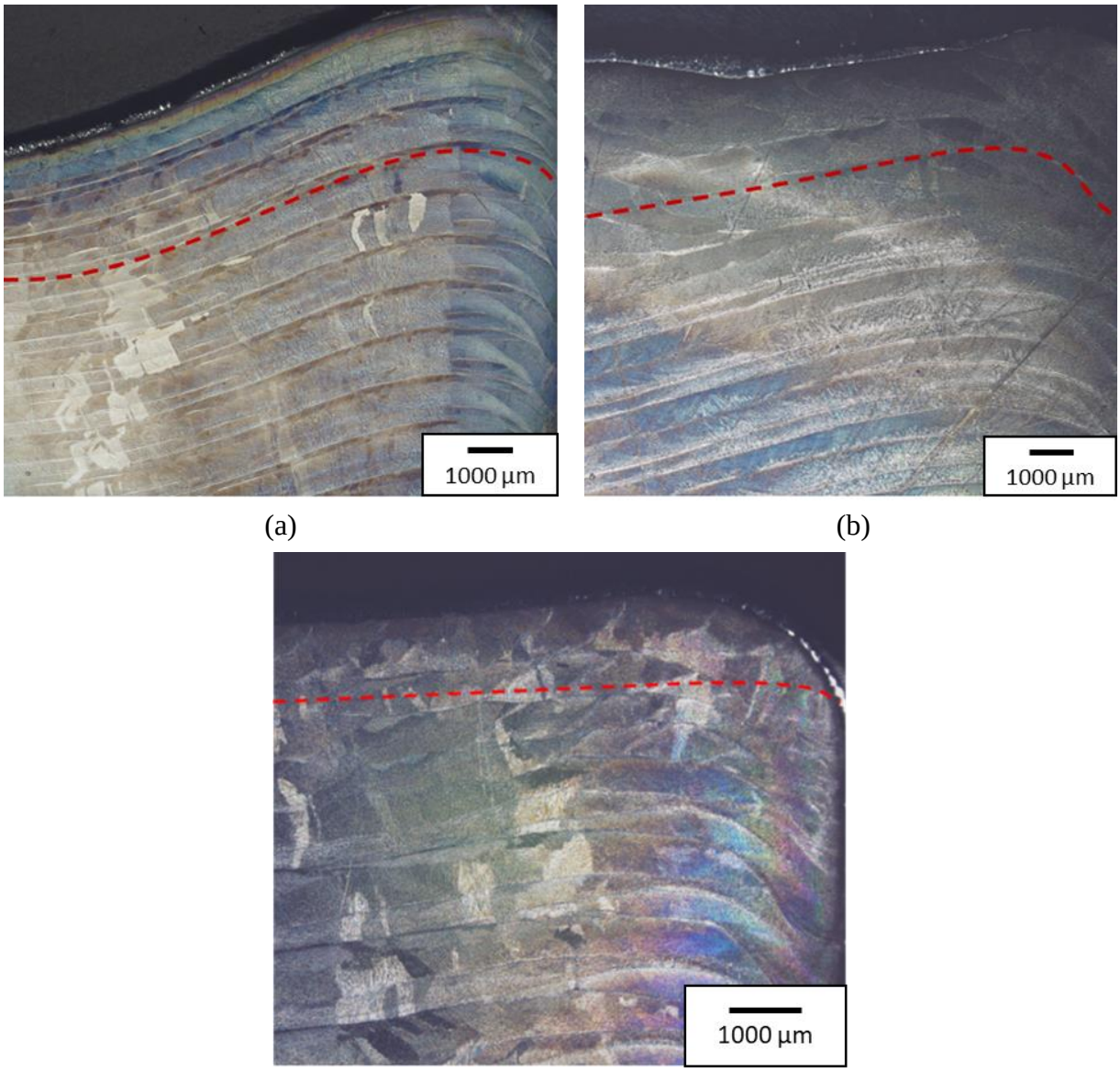


(a) (b)

(c)

*Figure 7-20: Cross section of the parts in XZ plane: (a) Without correction, (b) with ASSLC (b) with ASSC*

### 7.11.4 Density

The density analysis is performed using Archimedes density analysis, optical microscopy, and CT scan. The Archimedes density analysis of the sample indicates a density of 7.88 -7.92 g/cc for all the samples indicating that the density of the samples is not significantly affected by the application of correction. Figure 7-21 presents the cross-section images of the samples built without correction

and with the application of the correction strategy. The presence of micro-pores is observed along the cross-section. The pores are mainly circular indicating the presence of gas porosity in the samples. However, a few lack of fusion pores are also observed at isolated locations due to incomplete melting and solidification. CT analysis is performed on cylindrical samples extracted from the cuboid built with and without correction as shown in Figure 7-22. The CT analysis supports the Archimedes results indicating the presence of only a few micropores at isolated locations along the volume. It indicates a similar pore size spectrum for all the samples. It may also be noted that the number of pores is observed to be higher for ASSLC samples, which are majorly dominated by a lack of fusion pores.

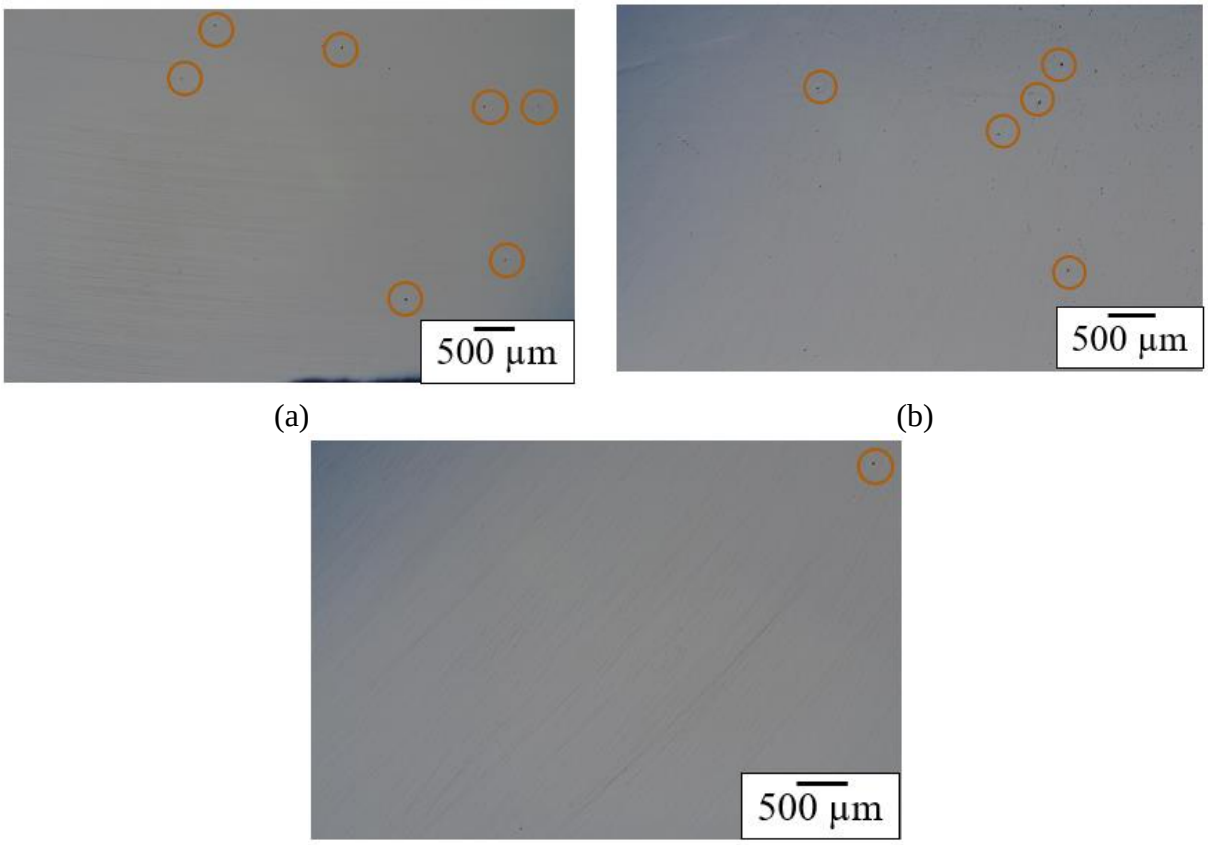


(a) (b)

(c)

*Figure 7-21: Optical microscopy of cross section of the parts: (a)Without correction, (b) ASSLC, (c) ASSC*

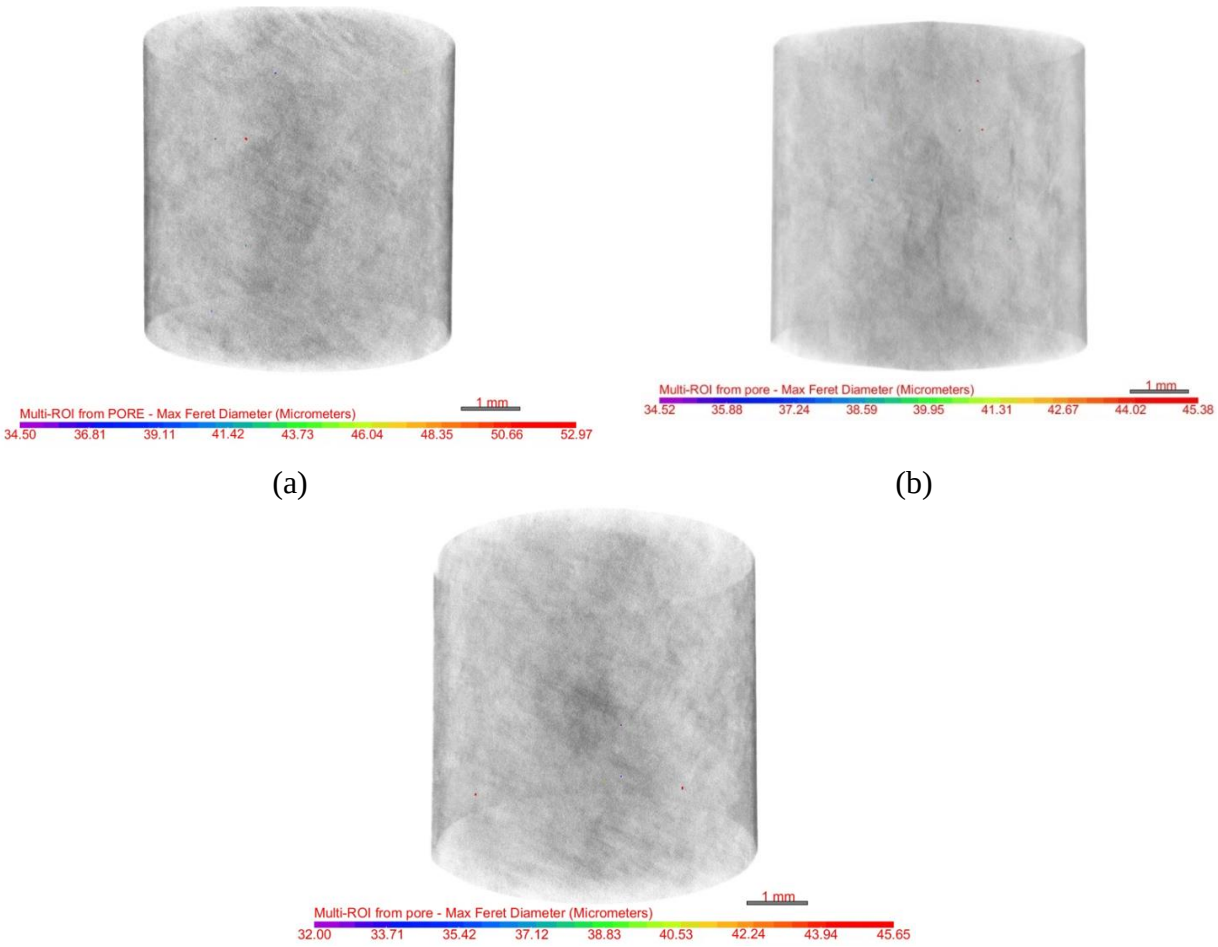


*Figure 7-22: CT analysis of samples (a) without correction, (b) with ASSLC (c) with ASSC*

## 7.12 Microstructure

Figure 7-23 presents the microstructure of the samples built with different control schemes. Microstructural investigation of the sample indicates cellular growth for all the samples. The microstructural evolution is a function of the G/R value and higher values of G/R during LDED promote the formation of cellular grains. The fine nature of the cellular growth observed at all conditions can be due to the faster cooling rates observed in LDED. A comparison of the cell size indicates that samples built using ASSLC have slightly lower cell sizes (3 – 4 µm) at some locations, with cell sizes majorly ranging from 4 – 5 µm at several locations. The localized lower cell size in some regions as compared to other samples can be mainly due to the laser turn-off and

on, which can increase the thermal gradient, leading to higher cooling rates (G × R). The average cell size of samples built using ASSC and without control is 4 - 6 µm. Thus, it can be seen that the average cell size is not significantly influenced by the control schemes used in the present work. Due to the varying working distance in convex, concave and normal regions, the laser spot size for those regions will be varied, however, the laser has a depth of focus which within, the laser beam diameter is constant. In the regions with deviations of beyond the depth of focus, the change in laser spot size can change the energy density and therefor, temperature gradients and material properties, eventually leading to anisotropic properties. Therefor it is recommended to use post heat treatment to achieve isotropic material properties[183] .

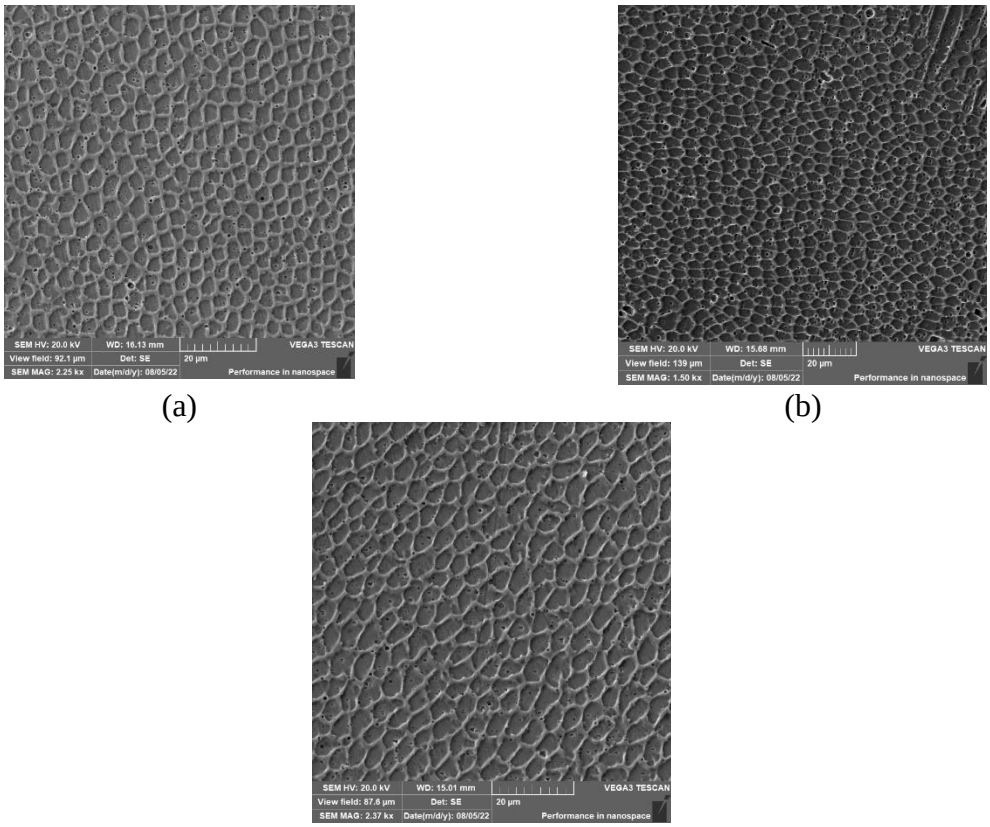


(a) (b)

(c)

*Figure 7-23: Microstructure: (a)Without correction, (b) with ASSLC (c) with ASSC*

## 7.13 Microhardness

Figure 7-24 presents the microhardness plot of the samples using different control schemes. It is observed that the strategy using ASSLC shows slightly higher micro-hardness values at certain locations along the cross-section as compared to the other samples. This is in line with the microstructural observations. The slightly higher hardness in a few regions can be due to relatively finer grain structure at regions subjected to higher cooling rates due to laser on and off. However, a comparison of the average microhardness indicates a significant overlap in the hardness of the material showing that the control strategies do not have a significant impact on the hardness of the built samples. The microhardness measurement experimental setup is outlined in section 3.6.3.

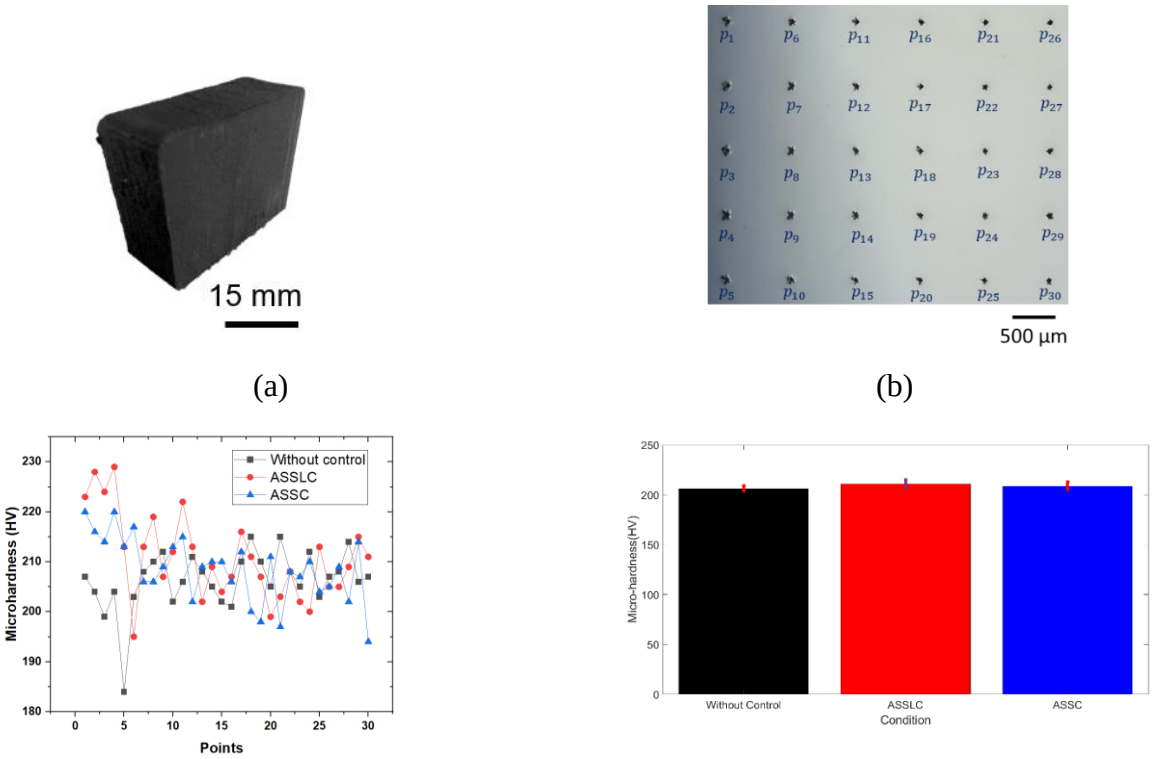


(a) (b)

(c) (d)

*Figure 7-24: (a) Cross section of the surface where the hardness tests are conducted (b) hardness indent points (c) Hardness profiles, (d) average hardness comparison*

## 7.14 Conclusion

The present work reports a novel intermittent adaptive dimension correction technique for LDED-PF parts. The developed technique uses the output of a deep learning defect detection platform to identify the geometric defect regions. This is followed by the extraction of the optimum boundary of defect regions using alpha-shape ConcaveHull and Minimum Spanning Tree (MST) algorithms. Subsequently, the correction layer trajectory is generated based on the height deviation using two techniques: Adaptive scanning speed control (ASSC) and Adaptive scanning speed and laser control (ASSLC) based on the last layer surface topography. ASSC and ASSLC methods improve the dimensional accuracy by 30% and 27.5%, respectively. Porosity, microstructure, and hardness tests were used to find the characteristics of the repaired components. The parts built using ASSLC and ASSC show good density, fine cellular growth, and similar microhardness values. It was also observed that the microstructure and mechanical properties of the corrected samples are similar to the samples built without correction. This indicates that the developed control algorithms can be used to improve the geometrical accuracy of LDED-PF built parts without altering the material properties significantly.

# 8 Conclusions and Future Work

The wide deployment of LDED-PF made parts for various engineering applications is challenged by the dimensional accuracy and its ability to built complex-shape components. This thesis considered the most used geometries such as thin walls and bulk geometries for adaptive trajectory planning. The work comprehends and contributes to the existing understanding on the trajectory planning of the LDED-PF process using offline and online techniques for the overhang wall and bulk structures, respectively with improved dimensional accuracy and geometric stability. On the basis of the research work, the following general conclusions can be drawn:

1. The offline adaptive trajectory planning algorithm for LDED-PF of thin-wall hemispherical dome structure used an adaptive tilt angle to avoid the collision between the nozzle and previously built material, while keeping in mind that the tilt angle cannot exceed the maximum overhang angle. The study provides an insight on to the deployment of collision detection technique to build complex overhang components. The proposed methodology avoids partitioning of the component and the deployment of computationally expensive algorithms to manufacture overhang dome structures using LDED-PF. The study showed the application of the technique to build dome structures with good geometric accuracy, density, and material properties. The study will pave a way for fabricating thin-walled storage tanks for various engineering applications.
2. The offline adaptive trajectory planning for bent pipe structures contributes to the existing literature through the development of an algorithm that uses adaptive slicing and adaptive scanning speed technique, at the same time facilitating the non-parallel deposition of material, and the substrate tilting permits the manufacturing of parts without support structures. The study also shows the development of deposition strategy by varying scanning speed that can

be used to build complex shape components without significant impact on density, microstructure, and mechanical properties. The results show the efficiency and robustness of the toolpath planning engine and its capability to build complex and dimensionally accurate components with varying overhang angles. The developed methodology has great potential to be applied to other AM processes such as laser hot-wire DED, wire-arc additive manufacturing, fused deposition modelling, electron beam DED, etc. to build self-supporting complex-shaped tubular geometries for various engineering applications.

3. A framework for defect detection was developed using deep learning to detect the surface defects during the build, which aids to prevent accumulation of geometric error during manufacturing. The hand-eye calibration is implemented to calibrate the laser scanner sensor to reconstruct the surface of the printed geometries with sub millimetre accuracy. Surface features are separated and annotated using DBSCAN algorithm and fed into a deep neural network called RandLA-Net and the overall accuracy of 91.3% is achieved. The framework for defect detection can be used for immediately pausing the process in case of surface defect detection and preventing further quality deterioration leading to unpredictable failures.
4. The defect-detection platform was further extended to the development of an automatic repair toolpath, which will identify the defect region, acquire defect boundaries automatically and compensate those defect regions by generating the repair strategies until the desired surface quality is achieved. The correction layer trajectory is generated based on the height deviation using two techniques: Adaptive scanning speed control (ASSC) and Adaptive scanning speed and laser control (ASSLC) based on the last layer surface topography. The adoption of ASSC and ASSLC methods improved the dimensional accuracy of the parts, while the microstructure and mechanical properties of the corrected samples are similar to the samples built without

correction. ASSC and ASSLC methods improve the dimensional accuracy by 30% and 27.5%, respectively. The online adaptive trajectory algorithms can be used to improve the geometrical accuracy of LDED-PF built parts without altering the material properties significantly.

## 8.1 Future Work

The following works can be planned for the future:

1. Offline adaptive trajectory planning for geometries with overhang features based on collision detection can be further extended to the evaluation of different particle size distribution, and material systems on the overhang geometries. In addition, the evaluation of structural integrity and the evolution of the microstructure of the fabricated dome component can also be carried out in the future works.
2. In case of offline adaptive trajectory planning for geometries with overhang features based on adaptive slicing, further analysis can be performed to improve the dimensional accuracy. The dimensional accuracy can be further improved by including in-situ laser scanning-based adaptive tool path generation. The in-situ laser scanning-based adaptive tool path generation allows quantifying the dimensional deviations after depositing a few layers. In addition to the scanning speed variation based on geometry used in the present work, the scanning speed variation considering the dimensional deviations can also be included.
3. Although the accuracy of the deep neural network competes with the state-of-the-art mIoU and overall accuracy, it can be further increased by increasing the number of training samples in the dataset. Implementing other defect types such as wavy surface defects, pores etc. in the deep learning framework can be a future plan. Instead of fitting the plane to the acquired point cloud from the as-built part, the reference surface can be generated by slicing the CAD model,

which can be used to compare the surface deviation to the reference plane acquired from the CAD data.

4. The online adaptive trajectory planning can be extended to non-planar geometries and components with overhang parts. The future work will also include the development of algorithms to optimize the repair toolpath generation and number of measurements to improve the efficiency of the inspection process, while maintaining the dimension accuracy. The study also will be extended to a hybrid process which in a subtractive operation will be employed if the dimensional deviation is beyond repair using the LDED repair toolpath.

# Letter of Copyright Permission





**Process planning for additive manufacturing of geometries with variable overhang angles using a robotic laser directed energy deposition system**

**Author:**
Farzaneh Kaji,Arackal Narayanan Jinoop,Mark Zimny,German Frikel,Kyle Tam,Ehsan Toyserkani

**Publication:** Additive Manufacturing Letters
**Publisher:** Elsevier
**Date:** April 2022



## Journal Author Rights

Please note that, as the author of this Elsevier article, you retain the right to include it in a thesis or dissertation, provided it is not published commercially. Permission is not required, but please ensure that you reference the journal as the original source. For more information on this and on your other retained rights, please visit: https://www.elsevier.com/about/our-business/policies/copyright#Author-rights

BACK CLOSE WINDOW

## Robotic laser directed energy deposition-based additive manufacturing of tubular components with variable overhang angles: Adaptive trajectory planning and characterization

**Author:**
Farzaneh Kaji,Arackal Narayanan Jinoop,Ali Zardoshtian,Patrick Hallen,German Frikel,Tianyi Tang,Mark Zimny,Ehsan Toyserkani

**Publication:** Additive Manufacturing

**Publisher:** Elsevier

**Date:** 5 January 2023

# References


[1] H. W. Tan, J. An, C. K. Chua, and T. Tran, "Metallic nanoparticle inks for 3D printing of electronics," *Adv. Electron. Mater.*, vol. 5, no. 5, p. 1800831, 2019.

[2] W. L. Ng, C. K. Chua, and Y.-F. Shen, "Print Me An Organ! Why We Are Not There Yet," *Prog. Polym. Sci.*, vol. 97, p. 101145, 2019, doi: https://doi.org/10.1016/j.progpolymsci.2019.101145.

[3] Y. Y. C. Choong, S. Maleksaeedi, H. Eng, S. Yu, J. Wei, and P.-C. Su, "High speed 4D printing of shape memory polymers with nanosilica," *Appl. Mater. Today*, vol. 18, p. 100515, 2020, doi: https://doi.org/10.1016/j.apmt.2019.100515.

[4] A. Dass and A. Moridi, "State of the art in directed energy deposition: From additive manufacturing to materials design," *Coatings*. 2019, doi: 10.3390/COATINGS9070418.

[5] S. L. Sing, C. F. Tey, J. H. K. Tan, S. Huang, and W. Y. Yeong, "2 - 3D printing of metals in rapid prototyping of biomaterials: Techniques in additive manufacturing," in *Woodhead Publishing Series in Biomaterials*, R. B. T.-R. P. of B. (Second E. Narayan, Ed. Woodhead Publishing, 2020, pp. 17–40.

[6] E. Toyserkani, A. Khajepour, and S. Corbin, *Laser Cladding Laser Cladding*. 2017.

[7] T. Hwang, Y. Y. Woo, S. W. Han, and Y. H. Moon, "Functionally graded properties in directed-energy-deposition titanium parts," *Opt. Laser Technol.*, vol. 105, pp. 80–88, 2018, doi: https://doi.org/10.1016/j.optlastec.2018.02.057.

[8] A. Sylvester Bolokang and M. Ntsoaki Mathabathe, "Chapter 11 - Laser cladding—a modern joining technique," in *Handbooks in Advanced Manufacturing*, J. Paulo Davim, K. Gupta, K. Gupta, and J. B. T.-A. W. and D. Paulo Davim, Eds. Elsevier, 2021, pp. 291–319.

[9] I. E. Anderson, E. M. H. White, and R. Dehoff, "Feedstock powder processing research needs for additive manufacturing development," *Curr. Opin. Solid State Mater. Sci.*, vol. 22, no. 1, pp. 8–15, 2018, doi: https://doi.org/10.1016/j.cossms.2018.01.002.

[10] D. Jafari, T. H. J. Vaneker, and I. Gibson, "Wire and arc additive manufacturing: Opportunities and challenges to control the quality and accuracy of manufactured parts," *Mater. Des.*, vol. 202, p. 109471, 2021, doi: https://doi.org/10.1016/j.matdes.2021.109471.

[11] G. Zhu, D. Li, A. Zhang, G. Pi, and Y. Tang, "The influence of laser and powder defocusing characteristics on the surface quality in laser direct metal deposition," *Opt. Laser Technol.*, vol. 44, no. 2, pp. 349–356, 2012, doi: https://doi.org/10.1016/j.optlastec.2011.07.013.

[12] J. Ertveldt, P. Guillaume, and J. Helsen, "MiCLAD as a platform for real-time monitoring and machine learning in laser metal deposition," *Procedia CIRP*, vol. 94, pp. 456–461, 2020, doi: https://doi.org/10.1016/j.procir.2020.09.164.

[13] F. S. H. B. Freeman, B. Thomas, L. Chechik, and I. Todd, "Multi-faceted monitoring of powder flow rate variability in directed energy deposition," *Addit. Manuf. Lett.*, vol. 2, p. 100024, 2022, doi: https://doi.org/10.1016/j.addlet.2021.100024.

[14] M. Farhan Khan *et al.*, "Real-time defect detection in 3D printing using machine learning," *Mater. Today Proc.*, vol. 42, pp. 521–528, 2021, doi: https://doi.org/10.1016/j.matpr.2020.10.482.

[15] L. E. Murr *et al.*, "Microstructural architecture, microstructures, and mechanical properties for a

nickel-base superalloy fabricated by electron beam melting," *Metall. Mater. Trans. A*, vol. 42, no. 11, pp. 3491–3508, 2011.

[16] W. E. Frazier, "Metal additive manufacturing: a review," *J. Mater. Eng. Perform.*, vol. 23, no. 6, pp. 1917–1928, 2014.

[17] A. Giampieri, J. Ling-Chin, Z. Ma, A. Smallbone, and A. P. Roskilly, "A review of the current automotive manufacturing practice from an energy perspective," *Appl. Energy*, vol. 261, p. 114074, 2020, doi: https://doi.org/10.1016/j.apenergy.2019.114074.

[18] B. Sun, Q. Ma, X. Wang, J. Liu, and M. R. M. Rejab, "Additive manufacturing in medical applications: a brief review," in *IOP conference series: materials science and engineering*, 2021, vol. 1078, no. 1, p. 12007.

[19] J. C. Najmon, S. Raeisi, and A. Tovar, "Review of additive manufacturing technologies and applications in the aerospace industry," *Addit. Manuf. Aerosp. Ind.*, pp. 7–31, 2019.

[20] S. G. Sarvankar and S. N. Yewale, "Additive manufacturing in automobile industry," *Int. J. Res. Aeronaut. Mech. Eng*, vol. 7, no. 4, pp. 1–10, 2019.

[21] C. Sun, Y. Wang, M. D. McMurtrey, N. D. Jerred, F. Liou, and J. Li, "Additive manufacturing for energy: A review," *Appl. Energy*, vol. 282, p. 116041, 2021.

[22] "ISO/ASTM 52909:2022 Additive manufacturing of metals — Finished part propertiesTitle." https://www.iso.org/standard/74639.html#:~:text=ISO - ISO%2FASTM 52909%3A,for metal powder bed fusion.

[23] D.-G. Ahn, "Directed Energy Deposition (DED) Process: State of the Art," *Int. J. Precis. Eng. Manuf. Technol.*, vol. 8, no. 2, pp. 703–742, 2021, doi: 10.1007/s40684-020-00302-7.

[24] J. Wang, Y. Wang, Y. Su, and J. Shi, "Evaluation of in-situ alloyed Inconel 625 from elemental powders by laser directed energy deposition," *Mater. Sci. Eng. A*, vol. 830, p. 142296, 2022.

[25] G. Piscopo and L. Iuliano, "Current research and industrial application of laser powder directed energy deposition," *Int. J. Adv. Manuf. Technol.*, vol. 119, no. 11, pp. 6893–6917, 2022, doi: 10.1007/s00170-021-08596-w.

[26] M. J. Heiden *et al.*, "Evolution of 316L stainless steel feedstock due to laser powder bed fusion process," *Addit. Manuf.*, vol. 25, pp. 84–103, 2019.

[27] A. El Hassanin *et al.*, "On the effect of the layer thickness in Laser-Powder Bed Fusion of pre-mixed Incone1718-Cu powders," in *2021 IEEE 6th International Forum on Research and Technology for Society and Industry (RTSI)*, 2021, pp. 36–40, doi: 10.1109/RTSI50628.2021.9597295.

[28] D.-S. Shim, G.-Y. Baek, J.-S. Seo, G.-Y. Shin, K.-P. Kim, and K.-Y. Lee, "Effect of layer thickness setting on deposition characteristics in direct energy deposition (DED) process," *Opt. Laser Technol.*, vol. 86, pp. 69–78, 2016, doi: https://doi.org/10.1016/j.optlastec.2016.07.001.

[29] W. Eidt, E.-P. Tatman, J. McCarther, J. Kastner, S. Gunther, and J. Gockel, "Surface roughness characterization in laser powder bed fusion additive manufacturing," 2019.

[30] O. Craig, A. Bois-Brochu, and K. Plucknett, "Geometry and surface characteristics of H13 hot-work tool steel manufactured using laser-directed energy deposition," *Int. J. Adv. Manuf. Technol.*, vol. 116, no. 1, pp. 699–718, 2021, doi: 10.1007/s00170-021-07322-w.

[31] L. E. dos Santos Paes *et al.*, "Understanding the behavior of laser surface remelting after directed

energy deposition additive manufacturing through comparing the use of iron and Inconel powders," *J. Manuf. Process.*, vol. 70, pp. 494–507, 2021, doi: https://doi.org/10.1016/j.jmapro.2021.08.061.

[32] M. Alimardani, V. Fallah, M. Iravani-Tabrizipour, and A. Khajepour, "Surface finish in laser solid freeform fabrication of an AISI 303L stainless steel thin wall," *J. Mater. Process. Technol.*, vol. 212, no. 1, pp. 113–119, 2012, doi: https://doi.org/10.1016/j.jmatprotec.2011.08.012.

[33] H. Tan, G. Hu, F. Zhang, W. Fan, W. Hou, and W. Huang, "Formation mechanism of adhering powder and improvement of the surface quality during laser solid forming," *Int. J. Adv. Manuf. Technol.*, vol. 86, no. 5, pp. 1329–1338, 2016, doi: 10.1007/s00170-015-8269-6.

[34] A. Salmi, F. Calignano, M. Galati, and E. Atzeni, "An integrated design methodology for components produced by laser powder bed fusion (L-PBF) process," *Virtual Phys. Prototyp.*, vol. 13, no. 3, pp. 191–202, 2018.

[35] D. Svetlizky *et al.*, "Directed energy deposition (DED) additive manufacturing: Physical characteristics, defects, challenges and applications," *Mater. Today*, 2021, doi: https://doi.org/10.1016/j.mattod.2021.03.020.

[36] D. Wang *et al.*, "Recent progress on additive manufacturing of multi-material structures with laser powder bed fusion," *Virtual Phys. Prototyp.*, vol. 17, no. 2, pp. 329–365, 2022.

[37] D. R. Feenstra, R. Banerjee, H. L. Fraser, A. Huang, A. Molotnikov, and N. Birbilis, "Critical review of the state of the art in multi-material fabrication via directed energy deposition," *Curr. Opin. Solid State Mater. Sci.*, vol. 25, no. 4, p. 100924, 2021, doi: https://doi.org/10.1016/j.cossms.2021.100924.

[38] B. Chen, T. Wang, X. Xi, C. Tan, and X. Song, "Evaluation of in-situ alloyed Inconel 625 from elemental powders by laser directed energy deposition," *Rapid Prototyp. J.*, no. ahead-of-print, 2022.

[39] Q. Han, H. Gu, S. Soe, R. Setchi, F. Lacan, and J. Hill, "Manufacturability of AlSi10Mg overhang structures fabricated by laser powder bed fusion," *Mater. Des.*, vol. 160, pp. 1080–1095, 2018.

[40] J. Jiang, F. Weng, S. Gao, J. Stringer, X. Xu, and P. Guo, "A support interface method for easy part removal in directed energy deposition," *Manuf. Lett.*, vol. 20, pp. 30–33, 2019, doi: https://doi.org/10.1016/j.mfglet.2019.04.002.

[41] A. Khobzi, F. F. Mehr, S. Cockcroft, D. Maijer, S. L. Sing, and W. Y. Yeong, "The role of block-type support structure design on the thermal field and deformation in components fabricated by Laser Powder Bed Fusion," *Addit. Manuf.*, vol. 51, p. 102644, 2022.

[42] U. Chadha *et al.*, "Directed energy deposition via artificial intelligence-enabled approaches," *Complexity*, vol. 2022, 2022.

[43] J.-S. Lim, W.-J. Oh, C.-M. Lee, and D.-H. Kim, "Selection of effective manufacturing conditions for directed energy deposition process using machine learning methods.," *Sci. Rep.*, vol. 11, no. 1, p. 24169, Dec. 2021, doi: 10.1038/s41598-021-03622-z.

[44] G. K. Lewis and E. Schlienger, "Practical considerations and capabilities for laser assisted direct metal deposition," *Mater. Des.*, vol. 21, no. 4, pp. 417–423, 2000.

[45] M. Lalegani Dezaki *et al.*, "A review on additive/subtractive hybrid manufacturing of directed energy deposition (DED) process," *Adv. Powder Mater.*, vol. 1, no. 4, p. 100054, 2022, doi: https://doi.org/10.1016/j.apmate.2022.100054.

[46] I. G. Ian Gibson, “Additive manufacturing technologies 3D printing, rapid prototyping, and direct digital manufacturing.” Springer, 2015.

[47] B. Bax, R. Rajput, R. Kellet, and M. Reisacher, “Systematic evaluation of process parameter maps for laser cladding and directed energy deposition,” *Addit. Manuf.*, vol. 21, pp. 487–494, 2018.

[48] T. DebRoy, W. Zhang, J. Turner, and S. S. Babu, “Building digital twins of 3D printing machines,” *Scr. Mater.*, vol. 135, pp. 119–124, 2017, doi: https://doi.org/10.1016/j.scriptamat.2016.12.005.

[49] L. Song, V. Bagavath-Singh, B. Dutta, and J. Mazumder, “Control of melt pool temperature and deposition height during direct metal deposition process,” *Int. J. Adv. Manuf. Technol.*, vol. 58, no. 1–4, pp. 247–256, 2012.

[50] C. Li, Z. Y. Liu, X. Y. Fang, and Y. B. Guo, “Residual stress in metal additive manufacturing,” *Procedia Cirp*, vol. 71, pp. 348–353, 2018.

[51] D. C. Hofmann *et al.*, “Developing gradient metal alloys through radial deposition additive manufacturing,” *Sci. Rep.*, vol. 4, no. 1, pp. 1–8, 2014.

[52] A. Calleja, I. Tabernero, A. Fernández, A. Celaya, A. Lamikiz, and L. N. L. De Lacalle, “Improvement of strategies and parameters for multi-axis laser cladding operations,” *Opt. Lasers Eng.*, vol. 56, pp. 113–120, 2014.

[53] A. Singh, S. Kapil, and M. Das, “A comprehensive review of the methods and mechanisms for powder feedstock handling in directed energy deposition,” *Addit. Manuf.*, vol. 35, p. 101388, 2020.

[54] A. Thien, C. Saldana, and T. Kurfess, “Surface Qualification Toolpath Optimization for Hybrid Manufacturing,” *J. Manuf. Mater. Process.*, vol. 5, no. 3, 2021, doi: 10.3390/jmmp5030094.

[55] C. Guo, S. He, H. Yue, Q. Li, and G. Hao, “Prediction modelling and process optimization for forming multi-layer cladding structures with laser directed energy deposition,” *Opt. Laser Technol.*, vol. 134, p. 106607, 2021.

[56] V. Errico, A. Fusco, and S. L. Campanelli, “Effect of DED coating and DED+ Laser scanning on surface performance of L-PBF stainless steel parts,” *Surf. Coatings Technol.*, vol. 429, p. 127965, 2022.

[57] F. Weng, S. Gao, J. Jiang, J. Wang, and P. Guo, “A novel strategy to fabricate thin 316L stainless steel rods by continuous directed energy deposition in Z direction,” *Addit. Manuf.*, vol. 27, pp. 474–481, 2019.

[58] A. R. Nassar, J. S. Keist, E. W. Reutzel, and T. J. Spurgeon, “Intra-layer closed-loop control of build plan during directed energy additive manufacturing of Ti–6Al–4V,” *Addit. Manuf.*, vol. 6, pp. 39–52, 2015, doi: https://doi.org/10.1016/j.addma.2015.03.005.

[59] J. C. Heigel, P. Michaleris, and E. W. Reutzel, “Thermo-mechanical model development and validation of directed energy deposition additive manufacturing of Ti–6Al–4V,” *Addit. Manuf.*, vol. 5, pp. 9–19, 2015.

[60] E. Schlienger *et al.*, “Near Net Shape production of metal components using LENS,” 1998.

[61] J. M. Flynn, A. Shokrani, S. T. Newman, and V. Dhokia, “Hybrid additive and subtractive machine tools–Research and industrial developments,” *Int. J. Mach. Tools Manuf.*, vol. 101, pp. 79–101, 2016.

[62] M. Das *et al.*, “In situ synthesized TiB–TiN reinforced Ti6Al4V alloy composite coatings: microstructure, tribological and in-vitro biocompatibility,” *J. Mech. Behav. Biomed. Mater.*, vol. 29, pp. 259–271, 2014.

[63] J. M. Wilson, C. Piya, Y. C. Shin, F. Zhao, and K. Ramani, “Remanufacturing of turbine blades by laser direct deposition with its energy and environmental impact analysis,” *J. Clean. Prod.*, vol. 80, pp. 170–178, 2014, doi: https://doi.org/10.1016/j.jclepro.2014.05.084.

[64] F. Q. Liu, L. Wei, S. Q. Shi, and H. L. Wei, “On the varieties of build features during multi-layer laser directed energy deposition,” *Addit. Manuf.*, vol. 36, p. 101491, 2020.

[65] H. Liu, Z. Hu, X. Qin, Y. Wang, J. Zhang, and S. Huang, “Parameter optimization and experimental study of the sprocket repairing using laser cladding,” *Int. J. Adv. Manuf. Technol.*, vol. 91, no. 9, pp. 3967–3975, 2017.

[66] E. Díaz, J. M. Amado, J. Montero, M. J. Tobar, and A. Yáñez, “Comparative study of Co-based alloys in repairing low Cr-Mo steel components by laser cladding,” *Phys. Procedia*, vol. 39, pp. 368–375, 2012.

[67] Z. Liu *et al.*, “Feasibility exploration of superalloys for AISI 4140 steel repairing using laser engineered net shaping,” *Procedia Manuf.*, vol. 10, pp. 912–922, 2017.

[68] P. Ramiro-Castro, M. Ortiz, A. Alberdi, and A. Lamikiz, “Effects of Gravity and Non-Perpendicularity during Powder-Fed Directed Energy Deposition of Ni-Based Alloy 718 through Two Types of Coaxial Nozzle,” *Metals*, vol. 10, no. 5. 2020, doi: 10.3390/met10050560.

[69] “USER MANUAL: High Precision Coaxial Laser Cladding Head COAX$^{TM}$14o Title.”

[70] “FANUC America Corporation SYSTEM R-30iB and SYSTEM R-30iB Plus Controller Coordinated Motion Setup and Operation Manual.” .

[71] “FANUC ROTATION CONVENTION.” https://doc.rc-visard.com/v21.07/en/pose_format_fanuc.html (accessed Mar. 10, 2022).

[72] Y. Ding, R. Dwivedi, and R. Kovacevic, “Process planning for 8-axis robotized laser-based direct metal deposition system: A case on building revolved part,” *Robot. Comput. Integr. Manuf.*, 2017, doi: 10.1016/j.rcim.2016.08.008.

[73] N. Chen and M. Frank, “Process planning for hybrid additive and subtractive manufacturing to integrate machining and directed energy deposition,” 2019, doi: 10.1016/j.promfg.2019.06.140.

[74] P. Kulkarni, A. Marsan, and D. Dutta, “A review of process planning techniques in layered manufacturing,” *Rapid Prototyp. J.*, vol. 6, no. 1, pp. 18–35, 2000.

[75] S. R. Narasimharaju *et al.*, “A comprehensive review on laser powder bed fusion of steels: Processing, microstructure, defects and control methods, mechanical properties, current challenges and future trends,” *J. Manuf. Process.*, vol. 75, pp. 375–414, 2022, doi: https://doi.org/10.1016/j.jmapro.2021.12.033.

[76] J. Jiang, S. T. Newman, and R. Y. Zhong, “A review of multiple degrees of freedom for additive manufacturing machines,” *Int. J. Comput. Integr. Manuf.*, vol. 34, no. 2, pp. 195–211, Feb. 2021, doi: 10.1080/0951192X.2020.1858510.

[77] J. Jiang, J. Stringer, X. Xu, and R. Y. Zhong, “Investigation of printable threshold overhang angle in extrusion-based additive manufacturing for reducing support waste,” *Int. J. Comput. Integr. Manuf.*, vol. 31, no. 10, pp. 961–969, Oct. 2018, doi: 10.1080/0951192X.2018.1466398.

[78] P. M. Bhatt, R. K. Malhan, A. V Shembekar, Y. J. Yoon, and S. K. Gupta, “Expanding capabilities of additive manufacturing through use of robotics technologies: A survey,” *Addit. Manuf.*, vol. 31, p. 100933, 2020, doi: https://doi.org/10.1016/j.addma.2019.100933.

[79] H. Kalami and J. Urbanic, “Process Planning of Creating a Surface Dome with Bead Deposition Additive Manufacturing,” *IFAC-PapersOnLine*, vol. 52, no. 10, pp. 230–235, 2019, doi: 10.1016/j.ifacol.2019.10.069.

[80] H. Kalami and J. Urbanic, “Exploration of surface roughness measurement solutions for additive manufactured components built by multi-axis tool paths,” *Addit. Manuf.*, vol. 38, no. August 2020, p. 101822, 2021, doi: 10.1016/j.addma.2020.101822.

[81] W. Xiangping, Z. Haiou, W. Guilan, and W. Lingpeng, “Adaptive slicing for multi-axis hybrid plasma deposition and milling,” 2014.

[82] P. M. Bhatt, R. K. Malhan, P. Rajendran, and S. K. Gupta, “Building free-form thin shell parts using supportless extrusion-based additive manufacturing,” *Addit. Manuf.*, vol. 32, p. 101003, 2020, doi: https://doi.org/10.1016/j.addma.2019.101003.

[83] “Lead/Lean Angles,” 2020. https://knowledge.autodesk.com/support/powermill/learn-explore/caas/CloudHelp/cloudhelp/2018/ENU/PWRM-ReferenceHelp/files/GUID-E3341040-E6FD-400F-A71F-6AE3BCF7147D-htm.html (accessed Jan. 26, 2022).

[84] M. Fujiki, J. Ni, and A. J. Shih, “Tool Path Planning for Near-Dry EDM Milling With Lead Angle on Curved Surfaces,” *J. Manuf. Sci. Eng.*, vol. 133, no. 5, Sep. 2011, doi: 10.1115/1.4004865.

[85] H. Kalami and J. Urbanic, “Process planning solution strategies for fabrication of thin-wall domes using directed energy deposition,” *Int. J. Comput. Integr. Manuf.*, pp. 1–17, 2022.

[86] C.-J. Bae, A. B. Diggs, and A. Ramachandran, “6 - Quantification and certification of additive manufacturing materials and processes,” J. Zhang and Y.-G. B. T.-A. M. Jung, Eds. Butterworth-Heinemann, 2018, pp. 181–213.

[87] A. Hussein, L. Hao, C. Yan, R. Everson, and P. Young, “Advanced lattice support structures for metal additive manufacturing,” *J. Mater. Process. Technol.*, vol. 213, no. 7, pp. 1019–1026, 2013.

[88] J.-X. Jiang XunAU - Stringer, JonathanTI - Support Structures for Additive Manufacturing: A Review, “No Title,” *Journal of Manufacturing and Materials Processing*, vol. 2, no. 4. 2018, doi: 10.3390/jmmp2040064.

[89] S. Kapil *et al.*, “5-axis slicing methods for additive manufacturing process,” 2017.

[90] F. Kaji and A. Barari, “Evaluation of the surface roughness of additive manufacturing parts based on the modelling of cusp geometry,” *IFAC-PapersOnLine*, vol. 28, no. 3, 2015, doi: 10.1016/j.ifacol.2015.06.157.

[91] H. Kalami and J. Urbanic, “Exploration of surface roughness measurement solutions for additive manufactured components built by multi-axis tool paths,” *Addit. Manuf.*, vol. 38, p. 101822, 2021, doi: https://doi.org/10.1016/j.addma.2020.101822.

[92] D. Ding, Z. Pan, D. Cuiuri, H. Li, N. Larkin, and S. van Duin, “Automatic multi-direction slicing algorithms for wire based additive manufacturing,” *Robot. Comput. Integr. Manuf.*, vol. 37, pp. 139–150, 2016, doi: https://doi.org/10.1016/j.rcim.2015.09.002.

[93] T. Shi, J. Shi, Z. Xia, B. Lu, S. H. Shi, and G. Y. Fu, “Precise control of variable-height laser metal deposition using a height memory strategy,” *J. Manuf. Process.*, vol. 57, pp. 222–232, 2020.

[94] Y. Murtezaoglu, D. Plakhotnik, M. Stautner, T. Vaneker, and F. J. A. M. van Houten, “Geometry-based process planning for multi-axis support-free additive manufacturing,” *Procedia CIRP*, vol. 78, pp. 73–78, 2018.

[95] X. Xiao and S. Joshi, “Process planning for five-axis support free additive manufacturing,” *Addit. Manuf.*, vol. 36, p. 101569, 2020, doi: https://doi.org/10.1016/j.addma.2020.101569.

[96] J. Ruan, L. Tang, F. W. Liou, and R. G. Landers, “Direct Three-Dimensional Layer Metal Deposition,” *J. Manuf. Sci. Eng.*, vol. 132, no. 6, Nov. 2010, doi: 10.1115/1.4002624.

[97] J. S. Panchagnula and S. Simhambhatla, “Additive Manufacturing of Complex Shapes Through Weld-Deposition and Feature Based Slicing.” Nov. 13, 2015, doi: 10.1115/IMECE2015-51583.

[98] A. Barari, H. A. Kishawy, F. Kaji, and M. A. Elbestawi, “On the surface quality of additive manufactured parts,” *Int. J. Adv. Manuf. Technol.*, vol. 89, no. 5–8, 2017, doi: 10.1007/s00170-016-9215-y.

[99] P. Singh and D. Dutta, “Multi-direction slicing for layered manufacturing,” *J. Comput. Inf. Sci. Eng.*, vol. 1, no. 2, pp. 129–142, 2001.

[100] Y. Li, D. He, X. Wang, and K. Tang, “Geodesic Distance Field-based Curved Layer Volume Decomposition for Multi-Axis Support-free Printing,” *arXiv Prepr. arXiv2003.05938*, 2020.

[101] M. W. Spong, “Robot dynamics and control,” 1989.

[102] W. Sui and D. Zhang, “Four Methods for Roundness Evaluation,” *Phys. Procedia*, vol. 24, pp. 2159–2164, 2012, doi: https://doi.org/10.1016/j.phpro.2012.02.317.

[103] “ISO 12181-1:2011(en).” https://www.iso.org/obp/ui/#iso:std:iso:12181:-1:ed-1:v1:en:sec:3.2.3 (accessed Sep. 27, 2022).

[104] C. Zhi-Min, W. Yun, and H. Jian, “Roundness deviation evaluation method based on statistical analysis of local least square circles,” *Meas. Sci. Technol.*, vol. 28, no. 10, p. 105017, 2017.

[105] W. J. Sames, F. A. List, S. Pannala, R. R. Dehoff, and S. S. Babu, “The metallurgy and processing science of metal additive manufacturing,” *Int. Mater. Rev.*, vol. 61, no. 5, pp. 315–360, 2016.

[106] S. Kou, “Welding metallurgy,” *New Jersey, USA*, vol. 431, no. 446, pp. 223–225, 2003.

[107] Z. Zhang, P. Farahmand, and R. Kovacevic, “Laser cladding of 420 stainless steel with molybdenum on mild steel A36 by a high power direct diode laser,” *Mater. Des.*, vol. 109, pp. 686–699, 2016, doi: https://doi.org/10.1016/j.matdes.2016.07.114.

[108] X. Wang, B. Zheng, K. Yu, S. Jiang, E. J. Lavernia, and J. M. Schoenung, “The role of cell boundary orientation on mechanical behavior: A site-specific micro-pillar characterization study,” *Addit. Manuf.*, vol. 46, p. 102154, 2021, doi: https://doi.org/10.1016/j.addma.2021.102154.

[109] P. R. Gradl, C. S. Protz, and T. Wammen, “Additive manufacturing and hot-fire testing of liquid rocket channel wall nozzles using blown powder directed energy deposition inconel 625 and JBK-75 Alloys,” in *AIAA Propulsion and Energy 2019 Forum*, 2019, p. 4362.

[110] A. Saboori, D. Gallo, S. Biamino, P. Fino, and M. Lombardi, “An overview of additive manufacturing of titanium components by directed energy deposition: microstructure and mechanical properties,” *Appl. Sci.*, vol. 7, no. 9, p. 883, 2017.

[111] J. N. Montero, A. Rodríguez, J. M. Amado, M. J. Tobar, and A. Yáñez, “Some optimization strategies for tool path generation in 3D laser metal deposition,” *LiM, Munich*, 2015.

[112] S. Wang, L. Zhu, J. Y. H. Fuh, H. Zhang, and W. Yan, “Multi-physics modeling and Gaussian process regression analysis of cladding track geometry for direct energy deposition,” *Opt. Lasers Eng.*, vol. 127, p. 105950, 2020.

[113] D. M. Hensinger, A. L. Ames, and J. L. Kuhlmann, “Motion planning for a direct metal deposition rapid prototyping system,” in *Proceedings 2000 ICRA. Millennium Conference. IEEE International Conference on Robotics and Automation. Symposia Proceedings (Cat. No. 00CH37065)*, 2000, vol. 4, pp. 3095–3100.

[114] D. Boisselier, S. Sankaré, and T. Engel, “Improvement of the laser direct metal deposition process in 5-axis configuration,” *Phys. Procedia*, vol. 56, pp. 239–249, 2014.

[115] Y. Zhang, Y. Chen, P. Li, and A. T. Male, “Weld deposition-based rapid prototyping: a preliminary study,” *J. Mater. Process. Technol.*, vol. 135, no. 2–3, pp. 347–357, 2003.

[116] T. Petrat, B. Graf, A. Gumenyuk, and M. Rethmeier, “Build-up strategies for generating components of cylindrical shape with laser metal deposition,” in *Lasers in Manufacturing Conference*, 2015, vol. 61.

[117] R. Liu, Z. Wang, Y. Zhang, T. Sparks, and F. Liou, “A smooth toolpath generation method for laser metal deposition,” in *Proceedings of the 27th Annual International Solid Freeform Fabrication Symposium, Austin, Texas, USA*, 2016, pp. 1038–1046.

[118] S. J. Wolff *et al.*, “In-situ observations of directed energy deposition additive manufacturing using high-speed x-ray imaging,” *Jom*, vol. 73, no. 1, pp. 189–200, 2021.

[119] P. Zhao, Y. Zhang, W. Liu, K. Zheng, and Y. Luo, “Influence mechanism of laser defocusing amount on surface texture in direct metal deposition,” *J. Mater. Process. Technol.*, vol. 312, p. 117822, 2023, doi: https://doi.org/10.1016/j.jmatprotec.2022.117822.

[120] Y. Li, H. Yang, X. Lin, W. Huang, J. G. Li, and Y. Zhou, “The influences of processing parameters on forming characterizations during laser rapid forming,” *Mater. Sci. Eng. A-structural Mater. Prop. Microstruct. Process.*, vol. 360, pp. 18–25, 2003.

[121] L. Tang and R. G. Landers, “Melt pool temperature control for laser metal deposition processes—Part I: Online temperature control,” *J. Manuf. Sci. Eng.*, vol. 132, no. 1, p. 11010, 2010.

[122] M. Mani, B. M. Lane, M. A. Donmez, S. C. Feng, and S. P. Moylan, “A review on measurement science needs for real-time control of additive manufacturing metal powder bed fusion processes,” *Int. J. Prod. Res.*, vol. 55, no. 5, pp. 1400–1418, Mar. 2017, doi: 10.1080/00207543.2016.1223378.

[123] K. Taherkhani, E. Sheydaeian, C. Eischer, M. Otto, and E. Toyserkani, “Development of a defect-detection platform using photodiode signals collected from the melt pool of laser powder-bed fusion,” *Addit. Manuf.*, vol. 46, p. 102152, 2021, doi: https://doi.org/10.1016/j.addma.2021.102152.

[124] Y. AbouelNour and N. Gupta, “In-situ monitoring of sub-surface and internal defects in additive manufacturing: A review,” *Mater. Des.*, vol. 222, p. 111063, 2022, doi: https://doi.org/10.1016/j.matdes.2022.111063.

[125] H. C. de Winton, F. Cegla, and P. A. Hooper, “A method for objectively evaluating the defect detection performance of in-situ monitoring systems,” *Addit. Manuf.*, vol. 48, p. 102431, 2021, doi: https://doi.org/10.1016/j.addma.2021.102431.

[126] M. Iravani-Tabrizipour and E. Toyserkani, “An image-based feature tracking algorithm for real-

time measurement of clad height," *Mach. Vis. Appl.*, 2007, doi: 10.1007/s00138-006-0066-7.

[127] A. Fathi, A. Khajepour, E. Toyserkani, and M. Durali, "Clad height control in laser solid freeform fabrication using a feedforward PID controller," *Int. J. Adv. Manuf. Technol.*, vol. 35, no. 3, pp. 280–292, 2007, doi: 10.1007/s00170-006-0721-1.

[128] T. Purtonen, A. Kalliosaari, and A. Salminen, "Monitoring and Adaptive Control of Laser Processes," *Phys. Procedia*, vol. 56, pp. 1218–1231, 2014, doi: https://doi.org/10.1016/j.phpro.2014.08.038.

[129] R. Sampson, R. Lancaster, M. Sutcliffe, D. Carswell, C. Hauser, and J. Barras, "An improved methodology of melt pool monitoring of direct energy deposition processes," *Opt. Laser Technol.*, vol. 127, p. 106194, 2020, doi: https://doi.org/10.1016/j.optlastec.2020.106194.

[130] M. H. Farshidianfar, A. Khajepour, and A. Gerlich, "Real-time control of microstructure in laser additive manufacturing," *Int. J. Adv. Manuf. Technol.*, vol. 82, no. 5, pp. 1173–1186, 2016, doi: 10.1007/s00170-015-7423-5.

[131] F. Mazzucato, S. Tusacciu, M. Lai, S. Biamino, M. Lombardi, and A. Valente, "Monitoring Approach to Evaluate the Performances of a New Deposition Nozzle Solution for DED Systems," *Technologies*, vol. 5, no. 2, 2017, doi: 10.3390/technologies5020029.

[132] M. H. Farshidianfar, A. Khajepour, and A. P. Gerlich, "Effect of real-time cooling rate on microstructure in Laser Additive Manufacturing," *J. Mater. Process. Technol.*, vol. 231, pp. 468–478, 2016, doi: https://doi.org/10.1016/j.jmatprotec.2016.01.017.

[133] S. Tang, G. Wang, and H. Zhang, "In situ 3D monitoring and control of geometric signatures in wire and arc additive manufacturing," *Surf. Topogr. Metrol. Prop.*, vol. 7, no. 2, p. 25013, 2019.

[134] A. Heralić, A.-K. Christiansson, M. Ottosson, and B. Lennartson, "Increased stability in laser metal wire deposition through feedback from optical measurements," *Opt. Lasers Eng.*, vol. 48, no. 4, pp. 478–485, 2010, doi: https://doi.org/10.1016/j.optlaseng.2009.08.012.

[135] L. Tang, J. Ruan, T. E. Sparks, R. G. Landers, and F. Liou, "Layer-to-layer height control of Laser Metal Deposition processes," in *2009 American Control Conference*, 2009, pp. 5582–5587, doi: 10.1109/ACC.2009.5160407.

[136] I. Garmendia, J. Pujana, A. Lamikiz, M. Madarieta, and J. Leunda, "Structured light-based height control for laser metal deposition," *J. Manuf. Process.*, vol. 42, pp. 20–27, 2019, doi: https://doi.org/10.1016/j.jmapro.2019.04.018.

[137] I. Garmendia, J. Leunda, J. Pujana, and A. Lamikiz, "In-process height control during laser metal deposition based on structured light 3D scanning," *Procedia CIRP*, vol. 68, pp. 375–380, 2018, doi: https://doi.org/10.1016/j.procir.2017.12.098.

[138] N. Yang, "Concentration model based on movement model of powder flow in coaxial laser cladding," *Opt. Laser Technol.*, vol. 41, no. 1, pp. 94–98, 2009, doi: https://doi.org/10.1016/j.optlastec.2008.03.008.

[139] L. Chen, X. Yao, P. Xu, S. K. Moon, and G. Bi, "Rapid surface defect identification for additive manufacturing with in-situ point cloud processing and machine learning," *Virtual Phys. Prototyp.*, vol. 16, no. 1, pp. 50–67, 2021.

[140] Z. Li *et al.*, "In Situ 3D Monitoring of Geometric Signatures in the Powder-Bed-Fusion Additive Manufacturing Process via Vision Sensing Methods," *Sensors* , vol. 18, no. 4. 2018, doi: 10.3390/s18041180.

[141] A. García-Díaz *et al.*, “OpenLMD, an open source middleware and toolkit for laser-based additive manufacturing of large metal parts,” *Robot. Comput. Integr. Manuf.*, vol. 53, pp. 153–161, 2018, doi: https://doi.org/10.1016/j.rcim.2018.04.006.

[142] F. Sohnius, P. Schlegel, M. Ellerich, and R. H. Schmitt, “Data-driven prediction of surface quality in fused deposition modeling using machine learning,” in *Production at the leading edge of technology*, Springer, 2019, pp. 473–481.

[143] Q. Wang, W. Jiao, P. Wang, and Y. Zhang, “A tutorial on deep learning-based data analytics in manufacturing through a welding case study,” *J. Manuf. Process.*, vol. 63, pp. 2–13, 2021.

[144] W. Jiao, Q. Wang, Y. Cheng, and Y. Zhang, “End-to-end prediction of weld penetration: A deep learning and transfer learning based method,” *J. Manuf. Process.*, vol. 63, pp. 191–197, 2021.

[145] D. S. Nguyen, H. S. Park, and C. M. Lee, “Optimization of selective laser melting process parameters for Ti-6Al-4V alloy manufacturing using deep learning,” *J. Manuf. Process.*, vol. 55, pp. 230–235, 2020.

[146] H. Yang *et al.*, “Deep learning-based X-ray computed tomography image reconstruction and prediction of compression behavior of 3D printed lattice structures,” *Addit. Manuf.*, vol. 54, p. 102774, 2022, doi: https://doi.org/10.1016/j.addma.2022.102774.

[147] W. Liu, J. Sun, W. Li, T. Hu, and P. Wang, “Deep learning on point clouds and its application: A survey,” *Sensors*, vol. 19, no. 19, p. 4188, 2019.

[148] K. Ren, Y. Chew, N. Liu, Y. F. Zhang, J. Y. H. Fuh, and G. J. Bi, “Integrated numerical modelling and deep learning for multi-layer cube deposition planning in laser aided additive manufacturing,” *Virtual Phys. Prototyp.*, pp. 1–15, 2021.

[149] F. Ogoke and A. B. Farimani, “Thermal control of laser powder bed fusion using deep reinforcement learning,” *Addit. Manuf.*, vol. 46, p. 102033, 2021, doi: https://doi.org/10.1016/j.addma.2021.102033.

[150] K. He, X. Zhang, S. Ren, and J. Sun, “Deep residual learning for image recognition,” in *Proceedings of the IEEE conference on computer vision and pattern recognition*, 2016, pp. 770–778.

[151] S. Xie, S. Liu, Z. Chen, and Z. Tu, “Attentional ShapeContextNet for Point Cloud Recognition,” in *2018 IEEE/CVF Conference on Computer Vision and Pattern Recognition*, 2018, pp. 4606–4615, doi: 10.1109/CVPR.2018.00484.

[152] H. Lu, H. Wang, Q. Zhang, S. W. Yoon, and D. Won, “A 3D Convolutional Neural Network for Volumetric Image Semantic Segmentation,” *Procedia Manuf.*, vol. 39, pp. 422–428, 2019, doi: https://doi.org/10.1016/j.promfg.2020.01.386.

[153] J. Lee, H. Lee, and D. Mun, “3D convolutional neural network for machining feature recognition with gradient-based visual explanations from 3D CAD models,” *Sci. Rep.*, vol. 12, no. 1, p. 14864, 2022, doi: 10.1038/s41598-022-19212-6.

[154] C. R. Qi, H. Su, K. Mo, and L. J. Guibas, “Pointnet: Deep learning on point sets for 3d classification and segmentation,” in *Proceedings of the IEEE conference on computer vision and pattern recognition*, 2017, pp. 652–660.

[155] C. R. Qi, L. Yi, H. Su, and L. J. Guibas, “PointNet++: Deep Hierarchical Feature Learning on Point Sets in a Metric Space,” in *Proceedings of the 31st International Conference on Neural Information Processing Systems*, 2017, pp. 5105–5114.

[156] R. Y. Tsai and R. K. Lenz, “A new technique for fully autonomous and efficient 3D robotics hand/eye calibration,” *IEEE Trans. Robot. Autom.*, vol. 5, pp. 345–358, 1989.

[157] Y. C. Shiu and S. Ahmad, “Calibration of wrist-mounted robotic sensors by solving homogeneous transform equations of the form AX=XB,” *IEEE Trans. Robot. Autom.*, vol. 5, no. 1, pp. 16–29, 1989, doi: 10.1109/70.88014.

[158] A. Nurunnabi, G. West, and D. Belton, “Outlier detection and robust normal-curvature estimation in mobile laser scanning 3D point cloud data,” *Pattern Recognit.*, vol. 48, no. 4, pp. 1404–1419, 2015.

[159] L. R. Muñoz, M. G. Villanueva, and C. G. Suárez, “A tutorial on the total least squares method for fitting a straight line and a plane,” *Rev. Cienc. e Ingen. del Inst. Technol. Super. Coatzacoalcos*, vol. 1, pp. 167–173, 2014.

[160] E. Schubert, J. Sander, M. Ester, H. P. Kriegel, and X. Xu, “DBSCAN revisited, revisited: why and how you should (still) use DBSCAN,” *ACM Trans. Database Syst.*, vol. 42, no. 3, pp. 1–21, 2017.

[161] Q. Hu *et al.*, “Randla-net: Efficient semantic segmentation of large-scale point clouds,” in *Proceedings of the IEEE/CVF Conference on Computer Vision and Pattern Recognition*, 2020, pp. 11108–11117.

[162] Y. Li, R. Bu, M. Sun, W. Wu, X. Di, and B. Chen, “PointCNN: Convolution On X-Transformed Points,” in *Advances in Neural Information Processing Systems*, 2018, vol. 31, [Online]. Available: https://proceedings.neurips.cc/paper/2018/file/f5f8590cd58a54e94377e6ae2eded4d9-Paper.pdf.

[163] B. Yang, S. Wang, A. Markham, and N. Trigoni, “Robust attentional aggregation of deep feature sets for multi-view 3D reconstruction,” *Int. J. Comput. Vis.*, vol. 128, no. 1, pp. 53–73, 2020.

[164] J. Bowers, R. Wang, L.-Y. Wei, and D. Maletz, “Parallel Poisson Disk Sampling with Spectrum Analysis on Surfaces,” Dec. 2010, SIGGRAPH A., [Online]. Available: https://www.microsoft.com/en-us/research/publication/parallel-poisson-disk-sampling-with-spectrum-analysis-on-surfaces/.

[165] “KNN.” https://en.wikipedia.org/wiki/K-nearest_neighbors_algorithm.

[166] Q.-Y. Zhou, J. Park, and V. Koltun, “Open3D: A modern library for 3D data processing,” *arXiv Prepr. arXiv1801.09847*, 2018.

[167] S. R. Bista, D. Hall, B. Talbot, H. Zhang, F. Dayoub, and N. Sünderhauf, “Evaluating the Impact of Semantic Segmentation and Pose Estimation on Dense Semantic SLAM,” in *2021 IEEE/RSJ International Conference on Intelligent Robots and Systems (IROS)*, 2021, pp. 5328–5335.

[168] V. Errico, S. L. Campanelli, A. Angelastro, M. Dassisti, M. Mazzarisi, and C. Bonserio, “Coaxial Monitoring of AISI 316L Thin Walls Fabricated by Direct Metal Laser Deposition,” *Mater. (Basel, Switzerland)*, vol. 14, no. 3, p. 673, Feb. 2021, doi: 10.3390/ma14030673.

[169] I. Jeon, L. Yang, K. Ryu, and H. Sohn, “Online melt pool depth estimation during directed energy deposition using coaxial infrared camera, laser line scanner, and artificial neural network,” *Addit. Manuf.*, vol. 47, p. 102295, 2021, doi: https://doi.org/10.1016/j.addma.2021.102295.

[170] E. Toyserkani, D. Sarker, O. O. Ibhadode, F. Liravi, P. Russo, and K. Taherkhani, “Metal Additive Manufacturing,” 2021.

[171] Y. Ding, J. Warton, and R. Kovacevic, “Development of sensing and control system for robotized laser-based direct metal addition system,” *Addit. Manuf.*, vol. 10, pp. 24–35, 2016, doi: https://doi.org/10.1016/j.addma.2016.01.002.

[172] I. Garmendia, J. Pujana, A. Lamikiz, J. Flores, and M. Madarieta, “Development of an Intra-Layer Adaptive Toolpath Generation Control Procedure in the Laser Metal Wire Deposition Process,” *Materials* , vol. 12, no. 3. 2019, doi: 10.3390/ma12030352.

[173] P. Xu *et al.*, “In-process adaptive dimension correction strategy for laser aided additive manufacturing using laser line scanning,” *J. Mater. Process. Technol.*, vol. 303, p. 117544, 2022, doi: https://doi.org/10.1016/j.jmatprotec.2022.117544.

[174] L. Qin, D. Zhao, W. Wang, and G. Yang, “Geometric defects identification and deviation compensation in laser deposition manufacturing,” *Opt. Laser Technol.*, vol. 155, p. 108374, 2022, doi: https://doi.org/10.1016/j.optlastec.2022.108374.

[175] D. Kono, H. Yamaguchi, Y. Oda, and T. Sakai, “Stabilization of standoff distance by efficient and adaptive updating of layer height command in directed energy deposition,” *CIRP J. Manuf. Sci. Technol.*, vol. 31, pp. 244–250, 2020, doi: https://doi.org/10.1016/j.cirpj.2020.05.015.

[176] F. Kaji, H. Nguyen-Huu, A. Budhwani, J. A. Narayanan, M. Zimny, and E. Toyserkani, “A deep-learning-based in-situ surface anomaly detection methodology for laser directed energy deposition via powder feeding,” *J. Manuf. Process.*, vol. 81, pp. 624–637, 2022, doi: https://doi.org/10.1016/j.jmapro.2022.06.046.

[177] F. P. Preparata and M. I. Shamos, “Convex hulls: Basic algorithms,” in *Computational geometry*, Springer, 1985, pp. 95–149.

[178] A. Moreira and M. Y. Santos, “Concave hull: A k-nearest neighbours approach for the computation of the region occupied by a set of points,” 2007.

[179] R. A. Jarvis, “On the identification of the convex hull of a finite set of points in the plane,” *Inf. Process. Lett.*, vol. 2, no. 1, pp. 18–21, 1973.

[180] S. Peterson, “Computing constrained Delaunay triangulations,” *Univ. Minnesota*, 1997.

[181] D. P. Mandal and C. A. Murthy, “Selection of alpha for alpha-hull in R2,” *Pattern Recognit.*, vol. 30, no. 10, pp. 1759–1767, 1997.

[182] K. Yerex and M. Jägersand, “Displacement mapping with ray-casting in hardware.,” in *SIGGRAPH sketches*, 2004, p. 149.

[183] S. Chen *et al.*, “Effect of heat treatment on the anisotropy in mechanical properties of selective laser melted AlSi10Mg,” *Mater. Sci. Eng. A*, vol. 858, p. 144130, 2022, doi: https://doi.org/10.1016/j.msea.2022.144130.